Inauguraldissertation

zur Erlangung der Doktorwürde
der
Fakultät für Physik
der Universität Bielefeld

vorgelegt von
Diplomphysiker Achim Donnermeyer
aus Ibbenbüren

Tag der mündlichen Prüfung: 16.8.2007

Scanning Ion–Conductance Microscopy

Gutachter: Prof. Dr. Markus Sauer
Prof. Dr. Günter Reiss

Abstract

In the present work, the development of a combined specialized scanning ion–conductance microscope (SICM) and fluorescence microscope for non–invasive topographical and optical studies on soft samples immersed in electrolyte solution is reported. In SICM, the scanning probe is an electrolyte-filled glass–nanopipette with a tip aperture diameter of about 50 nanometers. Conductivity of an ionic current through the tip, driven by electrodes inside and outside of the pipette, depends on the distance between tip and sample surface (topographical mapping) and on the sample's chemical properties (chemical mapping). For enhancing the sensitivity of the microscope, it is operated in alternating current mode by applying an oscillation to the probe and using a lock–in detection of the modulated current as feedback signal. The presented combination of scanning ion–conductance and fluorescence microscopy demonstrates parallel acquisition of correlated topographical and chemical or optical information. Characterization of the microscopes properties is presented with a detailed analysis of the interaction of all essential elements participating in its operation. Conceptual design and implementation of the control–software that operates on the instruments specialized real–time hardware is described. Successful employment of the SICM at a resolution beyond the Rayleigh criterion combined with fluorescence–optical studies is presented, demonstrating the manifold capabilities of this instrument for applications in the interacting fields of physics, biology, and chemistry.

Contents

1 Introduction

Throughout the last decades, scanning probe microscopy (SPM) techniques have gained significant importance in a variety of different research fields in science and technology. In the history of SPM, an important milestone was the invention of the scanning tunneling microscope (STM) by Binnig & Rohrer in 1981 *[Binnig et al., 1982; Binnig and Rohrer, 1982; Binnig et al., 1985]*. Nonetheless, the functional principle of SPM was already existing long before the advent of STM. Conceptual design of scanning near–field microscopy, which opens up the opportunity for exceeding the microscopical resolution given by Abbe's criterion *[Abbe, 1873]* has already been described by Synge in 1928 and O'Keefe in 1956 *[Synge, 1928; O'Keefe, 1956]*. But at that time, piezoelectrical technology necessary for the successful implementation of this idea was not available. In 1972, the development of the topographiner *[Young et al., 1972]* brought an apparatus, showing already a number of instrumental similarities as compared to the STM. This instrument was the first using piezoelectric actuators for positioning and scanning of a metal tip above the sample surface. Piezo actuators are transforming electrical energy into mechanical energy directly, and are the only instruments making possible translations in the sub–nanometer range without any frictional components limiting the resolution. During the work on the topographiner, also vibration isolation has been improved and identified to be an important key towards high resolution imaging. Since in the topographiner the tip–sample distance was controlled over a field emission signal, the lateral resolution was limited to about half a micrometer. But already in their publication, *Young* and coworkers predicted a significant increase in lateral resolution by bringing the probe closer to the sample surface and by utilizing the quantum–mechanical tunneling effect. Implementation of this idea took until 1981, when the first scanning tunneling microscope was developed. With its ultimate resolution power down to the atomic scale *[Binnig and Rohrer, 1983; Baum, 1986]*, this

microscope was in fact the first one in the family of scanning probe microscopes to attract high interest across the whole scientific community.

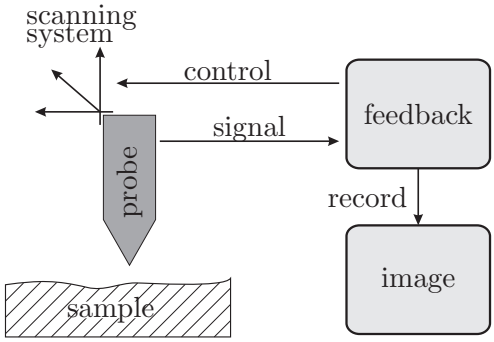

Figure 1.1: Scanning probe microscopy general scheme. Vertical interaction between a sharp probe and a sample surface is utilized for gathering local information, which is collected over lateral coordinates to give an image.

In scanning probe microscopy (figure 1.1), a sharp probe (e.g. metal tip, optical fiber, pipette) is raster–scanned across a sample surface by means of piezoelectric actuators, while a certain signal is recorded by the probe for every single image point. Scanning can be realized either by moving the probe or the sample. Since the interaction between the probe and the sample consists of local information, the term local probe technique can be found frequently. An important aspect in this concept – though not the only one – is to use the local interaction for monitoring the separation between the probe and sample. Thus, topographical information can be acquired in real–space. Two different modes of operation have to be distinguished, which are called the constant height mode and the constant signal mode. In constant height mode the absolute vertical position of the probe remains constant during scanning. Hereby the tip–sample separation changes according to the sample's topology yielding a varying signal of the probe. This mode of operation can be advantageous when small areas are to be scanned at high scan rates in order to minimize image distortion by, e.g. thermal drifts, especially when working at high or ultra–high resolution. Nevertheless, the risk of probe crashes which in almost any case results in damage of either the probe or the surface is high in constant height mode. In the constant signal mode, the signal provided by the probe is kept constant throughout the scan by continuous readjustment of the vertical position of either the sample or the probe by applying appropriate control voltage to the vertical piezo–actuator. Since this voltage contains the surface–height information, it can be used to trace the topology by correlating the signal with the coordinates given to the corresponding lateral piezo translators. Operating in this mode, large areas of up to $100 \times 100\ \mu\mathrm{m}^2$ of rough samples can be imaged while the risk of destroying the sample or the probe is minimal. As a drawback, lower scan rates are necessary in this mode

to allow correct vertical calibration of the height by the feedback loop.

Naming SPM techniques is commonly done straightforward by replacing the 'P' in SPM by an appropriate abbreviation describing the type of signal measured by the probe. For example, in scanning tunneling microscopy, the signal measured is a tunneling current and therefore its abbreviation is STM. In STM, the probe is a sharp metal tip scanned over an conducting sample's surface at distances of typically 1 nm. A bias voltage of commonly a few millivolts is applied between the tip and the sample inducing a tunneling current in the order of a few nanoamperes. An exponential relation between the tunneling current and the tip–surface distance makes the signal an extremely sensitive control to trace that separation. A variation of the distance by 1 Å induces a change of the tunneling current by a factor of approximately 10, meaning that in principle distance variations in the range of 0.001 nm can be monitored by keeping the current constant within a few percent. This is the basis for the ability of resolving single atoms using STM. Due to the fact that the STM information is obtained in real–space, local defects can be investigated, which implies an significant advantage compared to diffraction methods relying on extended periodic structures and thus showing averaged information.

In the last years, atomic force microscopy (AFM) has gained highest importance among all SPMs. AFM is a specialized scanning force microscopical (SFM) technique, where the common operation principle is sensing of forces between a sharp tip and a surface while the probe is raster scanned across the surface. The forces can be monitored by the scanning probe that is mounted on a cantilever beam. Thus the cantilever can act as a spring and sense the beams deflection, since the deflection depends on the tip–sample force and on the spring constant (*Hooke*'s law). For conventional AFM *[Binnig et al., 1986]*, the tip is fixed on a soft cantilever, permanently staying in contact with the sample surface during scanning. As the cantilever is not driven at an oscillation frequency, this AFM–operation mode can be characterized as a *static DC–mode* or *contact mode*. In the contact area of the tip apex (in the ideal case a single atom) repulsive forces occur due to overlapping electronic orbitals of tip and sample atom. Since these interatomic repulsive forces are short–range forces and confined to an extremely small area, they can be utilized to trace the surface topography with atomic resolution *[Binnig et al., 1987]*. Besides these short–range forces also long–range forces (e.g. electrical forces, magnetic forces, *van der Waals* forces), which can be attractive or repulsive, are observed. These forces interact across larger surface areas and are therefore not suited for atomic resolution imaging.

Until today, more than fifty members belong to the family of scanning probe technologies. Many of them are specially designed for the examination of certain suitable samples under customized appropriate conditions. For instance, conventionally STM is operated on conducting surfaces only under ultrahigh vacuum (UHV) and cryogenic conditions. On the other hand, magnetic force microscopy (MFM) *[Martin and Wickramasinghe, 1987]* is a technique needing a surface that features a magnetic moment for successful operating on measuring surface magnetic domains. Several specialized SPM techniques have been applied to chemistry and material sciences, to surface structure analysis and to spectroscopic measurements and many more *[Poggi et al., 2004]*. Additionally, there has always been a great interest in applying SPM to the imaging of biological systems like macromolecules, cellular organelles, and cells *[Driscoll et al., 1990; Umemura et al., 1993; Radmacher et al., 1992; Henderson et al., 1992; Hansma and Hoh, 1994; Shroff et al., 1995]*. However, in many cases the interaction between the microscope's tip and the sample remains only partially understood. Consequently, the soft surface of the sample is often damaged during SPM imaging *[Schoenenberger and Hoh, 1994; Hansma and Hoh, 1994; Lal and John, 1994]*. In atomic force microscopy (AFM), the 'tapping in liquid' mode of operation *[Putman et al., 1994; Sharma et al., 2005; Tsilimbaris et al., 2000; McElfresh et al., 2002; Le Grimellec et al., 1998]* has greatly reduced the problem of damaging the sample. Nevertheless, the mechanisms of image generation and their interpretation are unclear, and the nature of the adhesive interaction between the AFM tip and a 'sticky' specimen remains problematical. In summary, application of SPM to biological specimens often is not straightforward because of the difficulties in controlling the probe–sample separation over soft biological sample surfaces *[Fritz et al., 1993; Braet et al., 1998; Lesniewska et al., 1998; McElfresh et al., 2002]*.

A way to overcome these problems is scanning ion–conductance microscopy (SICM) developed in 1989 by Hansma et al. *[Hansma et al., 1989; Prater et al., 1991]*. Being one of the first offsprings from AFM, in SICM the scanning probe is an electrolyte–filled glass pipette that is scanned across the sample surface immersed under electrolyte solution. If a voltage is applied between an electrode inside the pipette and in the electrolyte reservoir, an ionic current can flow through the pipette aperture. Magnitude of the current depends on the conductivity through the opening of the pipette, and thus also on the probe–sample separation *[Nitz et al., 1998; Korchev et al., 1997a]*. By keeping the ionic current constant, this principle can be used for tracing the surface topography. As the separation between the probe tip and the sample is in the region

of 50 nm, destructive interaction between the probe and the sample can be avoided. This circumstance makes SICM very interesting for all applications that deal with surface–studies on biological samples.

During the years from its invention, a technological evolution has developed SICM by integrating several significant improvements. Already in 1996, *Proksch* and coworkers have demonstrated that problems with stability in the feedback distance control can be prevented by using the SICM probe as a tapping mode cantilever as well as a current sensitive probe *[Proksch et al., 1996]*. They used a piezo stack to excite a 10 nm rms free lateral oscillation amplitude at the pipettes resonant frequency of about 80 kHz. During scanning in tapping mode, this oscillation amplitude was typically reduced by about 60 % due to surface interaction, and this reduction was used as the feedback signal. However, all of their applications were limited to the imaging of flat polymeric films instead of complex physiological systems like cell membranes. Further improvements in the SICM technology were made by *Mann* et al.. They implemented a SICM with a backstep mode, which prevents the electrode tip from touching overhanging membrane areas *[Mann et al., 2002; Happel et al., 2003; Mann et al., 2006]*. Here, at the beginning of each image pixel that is to be scanned, the SICM probe is rejected from the surface by a predefined distance. On the one hand, this technique allows for very stable scanning of surfaces with complex topology. On the other hand, the scan duration is extended by a significant amount, preventing studies of dynamic processes and inducing errors due to possible movement of the living cell during the scan.

Maybe the largest step towards reliable and non invasive imaging of the sensible membrane of living cells is the AC–SICM mode, developed by *Pastré* et al. and *Shevchuk* et al. in 2001 *[Pastre et al., 2001; Shevchuk et al., 2001; Gu et al., 2002]*. In this method, the reliability and sensitivity of the SICM signal is enhanced by introducing a vertical oscillation of some tens of nanometers to the SICM probe. Since this oscillation of the tip near the scanned surface is translated into a modulation of the ionic current (AC), a periodical signal can be detected by a lock–in amplifier. This device is employing a technique known as phase sensitive detection, which implies the measurement of periodical signals at a bandwidth as small as 0.1 Hz. Application of this technique filters out many disturbing sources of error from the current signal, hence strongly increases the stability of the distance control. Furthermore, the response of the lock–in amplifier as depending from the tip–sample separation is much more sensitive than the ionic current. Therefore, surface analysis at larger distances is possible for improving stability in complex and delicate topographical environment, that is assisted by an enhancement

in the overall SICM resolution.

For these reasons, already since 1997 SICM is applied for noninvasive imaging of living cells *[Korchev et al., 1997a,b, 2000c]*, which is of interest since continuous high spatial resolution observations of living cells can greatly aid the elucidation of the relationship between outer structure of the cell membrane and its internal function. Furthermore, it facilitates the study of major physiological processes that are still not understood, like the mechanism of action of hormones *[Gorelik et al., 2004]*. In 2006, *Shevchuk* et al. have pushed the border of SICM resolution far beyond the *Rayleigh* limitation *[Shevchuk et al., 2006]*. Like generally true for SPMs, the resolution of a SICM is limited by the dimension of the probe used *[Korchev et al., 1997b; Gorelik et al., 2003]* and by the tip–sample separation, thus also limited by the overall mechanical stability of the microscope *[Hansma et al., 1989; Nitz et al., 1998; Bard et al., 1990]*. Using pipettes with an inner diameter of only 12.5 nm and improved mechanical stability of the setup, they demonstrated the SICM axial resolution to be as small as 3 nm. With this experimental setup it was possible to resolve individual membrane proteins embedded in the membrane of a living cell. This level of resolution enables the study of molecular processes of functional areas in membranes of living cells. Other processes like the function of ion channel proteins inside a cell membrane are commonly studied by patch–clamping techniques *[Hamill et al., 1981]*. However, in patch–clamping most commonly the spatial correlation between the ion–channel location and the cell membrane morphology is not present. Exact information about the distribution of certain ion–channels on the different functional areas of a cell membrane is often not available. SICM has been utilized for simultaneously imaging the topology of functional areas on the membranes of living cells and for detecting local currents induced by ion–channel operation *[Korchev et al., 2000b; Gorelik et al., 2002; Gu et al., 2002]*. Hereby, the functional location of single active ion–channels was compared with the spatial structure of the cell membrane giving additional information about fundamental working principles of the cell. Recently, *Sanchez* and coworkers have utilized the SICM probe for contactless mechanical sensation of mechanosensitive ion channels *[Sanchez et al., 2007]*. Mechanosensitive ion channels are fundamental for the operation of many complex processes inside the body, including such essentials like pain, hearing, growth, balance and touch *[Ghazi et al., 1998]*. Nevertheless, the molecular bases underlying mechanosensation are still unknown *[Kung, 2005]*. Mechanosensitive ion–channels consist of transmembrane proteins transducing mechanical force into electrical or chemical signals. *Sanchez* and coworkers have used the SICM probe to stimulate the mechanosensitive

ion–channels. This method makes contactless sensation of individual mechanosensitive ion–channels possible.

But not only the spatial information, also resolution and stableness of SICM have steadily been improved. In addition, fast temporal studies were performed. Dynamics of contracting cardiac myocytes have successfully been studied in real–time using SICM in AC mode *[Korchev et al., 2000a]*. Here, the contraction and expansion of the heart muscle cell of about 800 nm within some hundred milliseconds has been monitored using the distance signal of the SICM.

Although in principle SICM offers the potential to resolve processes on the molecular scale, chemical identification of certain individual molecules is impossible. Additional optical information could aid in further elucidating the underlying details in complex biological or chemical processes. Since this elucidation is often crucial for the understanding of processes undergoing in biological systems, combinations of SICM and optical microscopical setups have been realized. Combining an existing SICM with far–field optical microscopy is possible without significant additional technological challenges. Furthermore, far–field optical microscopy has long been an essential tool to biologists as imaging can be carried out *in vivo*. However, image resolution is limited to $\lambda/2$ following the *Rayleigh* criterion. This problem has been overcome by the development of the scanning near–field optical microscopy (SNOM) *[Pohl et al., 1984; Lewis et al., 1984]*. SNOM has the potential to resolve subdiffraction features of a sample , but lacks in robustness of the feedback distance control on soft biological surfaces *[Lewis and Lieberman, 1991]*. A combination of SNOM and SICM was successfully demonstrated *[Korchev et al., 2000c; Bruckbauer et al., 2002; Rothery et al., 2003]*, using the stable distance control signal of SICM combined advantages of SICM and SNOM can be used to correlate optical and spatial information. For studying the bases underlying mechanosensational processes of ion–channels, *Sanchez* et al. have integrated confocal fluorescence microscopy into a SICM setup. Basically, this combination is performed by positioning the confocal volume of the microscope objective directly beneath the SICM probe's tip. The process under investigation underlying mechanosensation is thought of being based on the transportation of Ca^{2+}. Since fluo-4-acetoxymethylester can act as as fluorescent dye that is coupling to Ca^{2+}, local changes in the calcium concentration can be measured by simultaneous contactless sensation of appropriate ion–channels using the SICM probe and fluorescence detection. Utilizing this method, *Sanchez* and coworkers have measured locally correlation between calcium movement and ion–channel sensation *[Sanchez et al., 2007]*.

One further aspect that volunteers SICM for applications in the context of surface–analyzing biological and chemical systems is its potential of controlled and localized deposition of molecules. Molecules in aqueous solution can easily be filled into the SICM probe. If electrically charged, the electric field built up by the SICM bias electrodes makes the molecules drift due to electrophoretic forces. Since this force depends on the magnitude of the field and on the sign of the molecule's charge, controlled delivery of the molecule through the tip aperture is possible. Using AC electric fields, control over electrically neutral molecules has been shown as well *[Ying et al., 2004]*. The base for this approach is the dielectrophoretic effect: an electric dipole momentum induced inside the molecule by the oscillationg electromagnetic field results in an interacting force. *Ying* et al. showed that by controlling the molecules velocity, even specific immobilization of the molecules by binding to appropriately functionalized surfaces is possible. Again, a possible detection mechanism is the identification of the immobilized molecule by means of fluorescence microscopic techniques. Applying this principle, delivery of fluorescence–labeled antibodies and similar macromolecules was demonstrated to produce a surface with spatially varying fluorescence *[Bruckbauer et al., 2003; Rodolfa et al., 2005]*. Furthermore, by applying this technique an addressable antibody nanoarray has been produced on a nanostructured surface *[Bruckbauer et al., 2004]*. The authors demonstrated that it is possible to selectively address specific features in a nanoarray by nanopipet delivery of a functional antibody. This method could be extended to perform local assembly of biological structures or to perform a local assay by delivery of reagents from the pipet at defined positions on the surface. Not only the delivery of molecules on functionalized glass surfaces, but also on membranes of living cells has been demonstrated. Individual lysozyme enzymes have been placed on a bacterial cell surface *[Hu and Lu, 2004]*. This was an important step towards probing single–molecule enzymatic reactions in living cells.

In the present work, the development of a specialized scanning ion–conductance microscope is described. It integrates the main advantage of SICM (noninvasive topographical analysis of soft biological surfaces) with those of confocal and wide–field fluorescence microscopy (structural and functional analysis of macromolecules in the sample). For enhanced stability of the microscope's control signal and for increasing its sensitivity, the method of phase–sensitive current detection is adopted. In order to manage a fast and reliable distance feedback control, specialized computer hardware capable of real–time performance in the 10 kHz regime is used. This hardware is steered by custom software whose implementation as a part of this work is designed to achieve stable

and sensitive but fast and efficient operation of the microscope. Within the second chapter of this work, an overview over the fundamental bases underlying the scientific and technological facets of the SICM is given. Different aspects of the complex interaction between electrolyte solution, glass capillary and bias electrodes are elucidated. The working principle of lock–in amplifiers, namely phase–sensitive detection is illustrated in the context of exact measuring of picoampere–sized modulations in the ionic current. As will be explained in this chapter too, electromagnetic and mechanical isolation methods must be applied to the microscope in order to realize these measurements with high temporal stability. Additionally, an overview is given on feedback control theory to ease understanding of the digital non–linear distance–control. This control is the central algorithm of the SICM software and is processed on real–time hardware. Therefore, a short review of real–time computing is given at the end of this chapter. The following chapter (Experimental Materials and Methods) is devoted to the technological description of the hardware components used for SICM and can be regarded as to be a SICM operation manual. Experimental results of this thesis and their discussion are presented in chapter 4 (Experimental Results and Discussion). Results report on the successful development of the SICM software by analyzing testing procedures. Also, the custom development of certain SICM hardware components like the probe holder and the isolation methods are described. Characterization and demonstration of the microscope is performed by examination of the scanning probes and by performing extensive SICM and fluorescence scanning of different appropriate surfaces. Hereby, information is obtained about all important factors describing the potential of the SICM and fluorescence microscope.

2 Fundamentals

2.1 SICM Functional Principle

The scanning ion–conductance microscope (SICM) is assigned to the category of scanning probe microscopes. It can image the topography of surfaces that are covered with electrolytes *[Hansma et al., 1989]*. For SICM, the scanning probe is a hollow, electrolyte–filled nanopipette that measures an ionic current passing through its tip aperture, which can be much smaller than 50 nm *[Nitz et al., 1998; Shevchuk et al., 2006]*. Since this flow of ions is sensitive to the distance between the tip and the sample surface due to partial blockage of the current, the topography of the specimen can be reproduced and, in principle, the probe does not come into contact with the surface.

The potential difference, that drives the current through the pipette aperture is applied by reversible silver–chloride electrodes, one inside of the pipette and one in the solution surrounding the sample. Unpredictable and complex processes at the electrodes induce drifts and fluctuations in the current circuit's overall conductance, that inevitably lead to artifacts in the control signal.

Furthermore, such fluctuations can result in the tip crashing into a rough surface, since the dependence of the ionic current on the distance between the tip and the sample is not very steep. The tip of the pipette will then break or damage the specimen. As a practical remedy, the operating distance from the sample surface has purposely been kept large *[Hansma et al., 1989; Korchev et al., 1997a]*. As a result, the sensitivity and resolution are decreased, since the effective size of the probe is related to this distance as well *[Hansma et al., 1989]*.

A new approach that has been implemented in the presented work uses a distance oscillation to significantly increase the sensitivity and resolution of the SICM *[Pastre*

et al., 2001]. The distance oscillation introduces an AC component in the ionic current. A lock-in amplifier is used to detect the changes in the modulated current amplitude precisely at the frequency that is applied to the distance oscillation, which is then used to control the feedback circuitry. This is a much more sensitive method than monitoring direct ionic current *[Hansma et al., 1989; Korchev et al., 1997a]* and allows the scanning probe to be operated only a few nm from the sample surface.

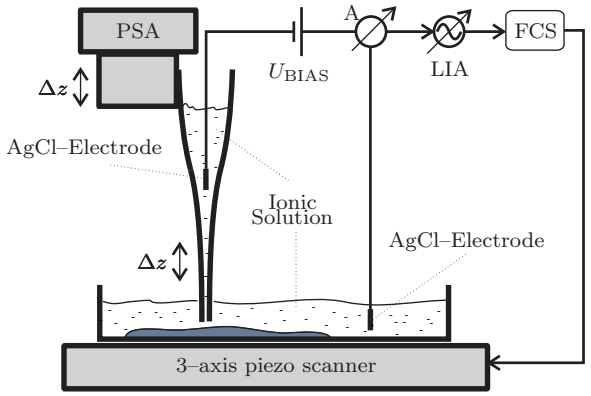

Figure 2.1: Schematic presentation of SICM. Ionic current flowing in solution through the probe tip aperture is modulated, since the probe is oscillated vertically by the piezo actuator PSA. The current passes a current–to–voltage converter before it is analyzed by a lock–in amplifier LIA. The LIA output is used for keeping the tip–sample distance constant by means of a feedback–control system FCS, while the sample is scanned with a XYZ–piezo scanning stage.

A detailed signal–pathway presentation of the developed SICM system is shown in figure 2.2. Hereafter, the nanoampere–sized current (I) flowing between the pipette electrode (PIP) and the counter electrode (CEL) in the bath is amplified and converted in–situ into a voltage signal by a headstage–preamplifier (PRA). A low–noise microelectrode amplifier (MEA) is further improving the current signals quality by filtering and correcting for errors and offsets. Since the sophisticated circuitry of this amplifier and additional electrical isolation, the ionic current can be measured at picoampere resolution. The output of the amplifier is connected to the input of the lock–in amplifier (LIA). This device is used for phase–sensitive detection of the input signal. Simultaneously, the LIA provides an oscillating reference signal (MOD) that is applied to a modulating piezo–stack actuator (PSA) over a piezo–controller (PCTRL). Attached to the pistil of this actuator is the probe within its holder by what the ionic current can be modulated at short tip–surface distances. In parallel, a real–time control system (RTC) is reading the (LIA) signal over a digital/analog converter (DAC) device to maintain the constant tip–sample distance by giving feedback voltage command to the Z–channel of the scanning stage's (PST) piezo controller PCTRL over the DAC. Furthermore, the RTC controls the lateral scan by giving adequate control commands to the X– and Y–channels of the piezo–scanning stage. Monitoring of all critical parameters is realized by reading analog input channels of the DAC connected

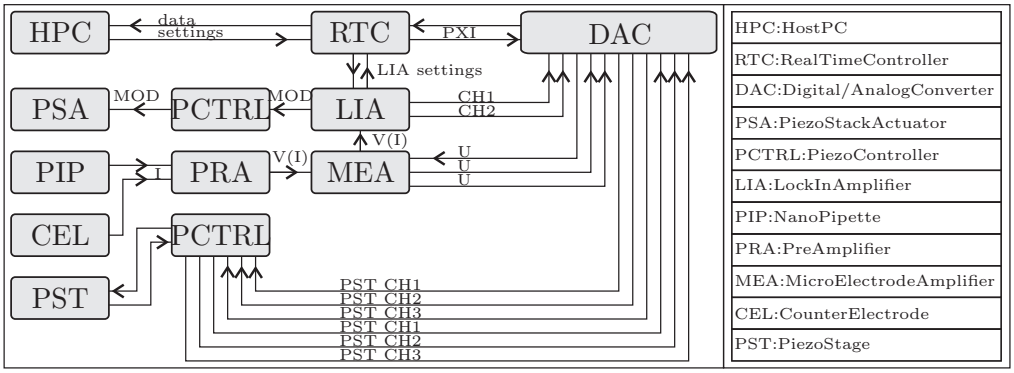

Figure 2.2: SICM–signal pathway. The modulated ionic current I between pipette electrode PIP and counter–electrode CEL is measured by a headstage–preamplifier PRA. After further amplification by a microelectrode amplifier MEA, the current is analyzed with a lock–in amplifier LIA which is also supplying reference oscillation MOD to the piezo–controller PCTRL of the modulating piezo–stack actuator PSA. The 3 piezo–stage channels are controlled and monitored by the real–time controller RTC, which is acquiring and writing over a PXI–bus connected 16bit digital/analog converter DAC. The LIA signals CH1 and CH2 as well as MEA voltage U and current I are evaluated by the RTC. LIA settings are under control by a GPIB connection with the RTC. All system parameters and experimental data are controlled and received by a host–PC HPC, connected over a 1Gbit ethernet TCP/IP connection to the RTC.

to signal outputs of the different devices. Image data and system settings are being received and adjusted by a host computer (HPC) that is connected to the RTC over TCP/IP steered Gigabit local area network.

2.2 Ionic Conductance in Electrolytic Solution and Glass Capillaries

The electrical conductivity of electrolytic solution is based on the movement of dissolved ions under the influence of an electric field. Ions of the charge $z \cdot e$ (valence z, $z \in \mathbb{Z}$; elementary charge e, $e \approx 1.6 \times 10^{-19}$ C) which are exposed to an electric field of the strength $\boldsymbol{E}$ experience a electrophoretic force $\boldsymbol{F_E} = z \cdot e\boldsymbol{E}$. Depending on the sign of z, the direction of this force is orientated parallel or anti–parallel to $\boldsymbol{E}$. The resulting acceleration of the ions is compensated by the complementary frictional force $\boldsymbol{F}_\mathrm{F} = 6\pi\eta r_\mathrm{I}\boldsymbol{v}$ with η = viscosity of solution and r_I = radius of solved ion. In the steady

state $\boldsymbol{F}_{\mathbf{E}} = \boldsymbol{F}_{\mathbf{F}}$ is true. Thus, for given η and $\boldsymbol{E}$, the steady–state velocity $\boldsymbol{v}_{\max}$ of the solvated ion is given by

$$\boldsymbol{v}_{\max} = \frac{ze\boldsymbol{E}}{6\pi\eta r_{\mathrm{I}}}. \tag{2.2.1}$$

Considering electrolytic solutions consisting of m different kinds of each anions and cations, one can define final velocities $\boldsymbol{v}_{\mathrm{m}}^{\pm}$ and densities $n_{\mathrm{m}}^{\pm}$ of z–fold charged ions per volume element. Then the product $n_{\mathrm{m}}^{\pm} \cdot \boldsymbol{v}_{\mathrm{m}}^{\pm}$ represents the amount of ions passing a unit of area A, perpendicular to the direction of movement per unit of time t. In this case the steady–state ionic current $\boldsymbol{j}_{\mathrm{ion}}$ can be written as

$$\boldsymbol{j}_{\mathrm{ion}} = A^{-1} \sum_{\mathrm{i}=1}^{\mathrm{m}} \frac{dQ_{\mathrm{i}}^{+}}{dt} + \frac{dQ_{\mathrm{i}}^{-}}{dt} = e \sum_{\mathrm{i}=1}^{\mathrm{m}} \left(n_{\mathrm{i}}^{+} z^{+} \boldsymbol{v}_{\mathrm{i}}^{+} + n_{\mathrm{i}}^{-} z^{-} \boldsymbol{v}_{\mathrm{i}}^{-} \right). \tag{2.2.2}$$

Introducing the concentration $c_{\mathrm{m}}^{\pm} = n_{\mathrm{m}}^{\pm}/N_{\mathrm{A}}$ [mol $\cdot$ cm^{-3}], with N_{A} being *Avogadros* number (N_{A}=6.02 $\cdot$ 10^{23} mol^{-1}), the ionic current density becomes

$$\boldsymbol{j}_{\mathrm{ion}} = eN_{\mathrm{A}} \sum_{\mathrm{i}=1}^{\mathrm{m}} \left(z^{+} \boldsymbol{v}_{\mathrm{i}}^{+} c_{\mathrm{i}}^{+} + z^{-} \boldsymbol{v}_{\mathrm{i}}^{-} c_{\mathrm{i}}^{-} \right). \tag{2.2.3}$$

Having in mind that η is a function of the temperature T of the solution, equations 2.2.1 and 2.2.3 show that for a given temperature and composition of the electrolyte the ionic current density $\boldsymbol{j}_{\mathrm{ionic}} = \boldsymbol{I}_{\mathrm{ionic}}/A$ is proportional to the electric field $\boldsymbol{E}$:

$$\boldsymbol{j}_{\mathrm{ion}} = \sigma \boldsymbol{E}. \tag{2.2.4}$$

It depends on the radii $r_{\mathrm{I}}^{\pm}$, the valences $z^{\pm}$, the concentrations $c^{\pm}$ of the ions, the viscosity η, the temperature T and on the dimensions of the ionic conductor, i.e. the cross section area. The dimension of σ is *Siemens* per metre [S/m], with 1 S = 1 A/V = 1 Ω^{-1} and it is reciprocal to the resistance of the electrolyte.

Ions solved in concentrated electrolytic solutions do not move independently from each other. Two ions of opposite charges q^{+} and q^{-} attract each other due to *Coulomb* force $\boldsymbol{F}_{\mathrm{C}}$ with

$$\boldsymbol{F}_{\mathrm{C}} = \frac{q^{+}q^{-}}{4\pi\varepsilon\varepsilon_0 r^2} \boldsymbol{r}_0. \tag{2.2.5}$$

Here, ε is the dielectric constant of the media surrounding the ions and $\varepsilon_0 = 8.85 \cdot 10^{-12}$ CV^{-1}m^{-1} is the electric field constant. $\boldsymbol{r}_0$ represents the vector of unity length

in direction of the connection between the ions. The corresponding *Coulomb* energy E_C is given by

$$E_C = -\boldsymbol{\nabla} \boldsymbol{F}_C = -\frac{q^+ q^-}{4\pi\varepsilon\varepsilon_0 r}. \tag{2.2.6}$$

Opposing the Coulomb–interaction there is the thermal energy $E_{th} \cong k_B T$ ($k_B = 1.38 \cdot 10^{-23}$ JK^{-1} is the *Boltzmann*–constant) that is giving anions and cations the ability to dissolve in water. Considering two ions of charge $+e$ and $-e$ at distance $r = 0.5$ nm dissolved in water ($\varepsilon = 80$) at 300 K, the relation E_{th}/E_C is $5.8 \cdot 10^{-21}$ K/$4.1 \cdot 10^{-21}$ K = 1.41. The thermal energy is sufficient to dissolve the two ions but not to create a general spacial independence between cations and anions. As a consequence, every ion is surrounded by a spherical symmetric constellation of counter–ions each of them representing a center of a spherical ion constellation itself. Influenced by an electric field, these charges are being separated meaning a disturbance of the charge distribution. Therefore, around a moving ion the ionic sphere is constantly renewing resulting in a decelerating force between center–ion and counter–ionic sphere. This so called relaxation–effect depends on the mean distance between the ions which is the concentration of the electrolytic solution.

Glass capillaries used in this work are made of borosilicate glass or fused silica. The surfaces of fused silica (SiO_2) as well as of borosilicate glass (composition of SiO_2 and B_2O_3) are mainly consisting of silanol (SiOH)–groups. These silanoles are ionized to negatively charged silanoate (SiO^-) groups if in contact with fluids of sufficient high pH–value. Attracted to the negatively charged silanoate groups, positively charged hydrated cations of the solution form an inner layer of cations on the capillary wall. This layer is referred to as the *Helmholtz*–layer and is locally fixed on the charged glass surface. Taking into account that thermal molecule movement of the solution tends to break up the fixed charge distribution, according to *Gouy–Chapman* one gets an additional diffuse ionic space–charge layer. As a result, the potential distribution in the direction perpendicular to the glass surface is a sum of two components. Between the surface silanoates and the *Helmholtz*–layer there is a linear potential decrease that is passing over into an exponential decay in the diffuse charge layer. An applied electric field, orientated in parallel to the glass surface (or in direction with the glass capillary axis), pulls the mobile diffuse cation layer in the direction of the negatively charged electrode. Since the moving cations are solvated, the bulk solution migrates with the mobile layer, causing electroosmotic flow (EOF) of the solution. The rate of EOF is dependent on the field strength and the charge density of the capillary wall. The walls

charge density depends on the pH–value of the buffer solution. The electroosmotic flow will increase with pH until all of the available silanol groups on the wall of the capillary are fully ionized.

2.3 Silver–Chloride Electrodes

For the application of the potential difference between the electrolyte solution inside and outside of the SICM probe, electrodes are used. Additionally at the interface between the liquid solution and the solid electrodes, transformation of the ionic current into an electronic current measurable by the preamplifier is performed. Obviously, the function of the electrodes plays a very central role in the SICM system. Many different kinds of electrodes are known, but not all of them are applicable in SICM. Silver/silverchloride electrodes are known to have advantageous properties like large potential stability, electrochemical reversibility and non–toxicity to biological systems that make them appropriate candidates for SICM.

Silver/silverchloride electrodes consist of a solid core of $Ag_{(s)}$ that is covered by a solid shell of its salt silver(I)chloride $AgCl_{(s)}$. Surrounded by an aqueous solution containing $Cl^-_{(aq)}$ the electrode system can be described as $Cl^-_{(aq)}|AgCl_{(s)}|Ag_{(s)}$. At the interface between $Ag_{(s)}$ and $AgCl_{(s)}$ an electron transfer takes place: $AgCl_{(s)} + e^- \rightleftarrows Ag_{(s)} + Cl^-_{(s)}$, whereas on the surface of the $AgCl_{(s)}$–shell a chemical exchange of $Cl^-_{(s)}$–anions occurs: $Cl^-_{(s)} \rightleftarrows Cl^-_{(aq)}$. In summary there is the equilibrium reaction equation

$$AgCl_{(s)} + e^-_{(metal)} \rightleftarrows Ag_{(s)} + Cl^-_{(aq)}. \tag{2.3.1}$$

The potential E of this electrode is given by the *Nernst* equation

$$E = E^0 - \frac{RT}{F} \ln\left(a_{Cl^-}\right) \tag{2.3.2}$$

where E^0 is the standard–potential of the hydrogen electrode, $R = 8.31\ JK^{-1}mol^{-1}$ is the ideal–gas constant, $F \cong 96.49$ kC/mol the *Faraday* constant and a_{Cl^-} the activity of the chloride–ions. This shows that the potential of silverchloride electrodes at given temperature T depends on the activity / concentration of the Cl^-–anions in the solution.

At the electrodes, current must be transformed smoothly from a flow of electrons in the copper wire to a flow of ions in solution. When using Ag/AgCl–electrodes

the following points should be considered to avoid possible artifacts in the observed current signal. First, silverchloride electrodes perform well only in solutions containing chloride ions. Second, because current must flow in a complete circuit, two electrodes are needed. If the two electrodes face different concentrations of Cl^-, there will be a difference in the half–cell potentials (the potential difference between the solution and the electrode) at the two electrodes, resulting in a large steady potential difference in the two wires attached to the electrodes. This steady potential difference, termed liquid junction potential, can be subtracted electronically and poses few problems as long as the electrodes are used within their reversible limits. Lastly, if the AgCl is exhausted by the current flow, bare silver could come in contact with the solution. Silver ions leaking from the wire are toxic to many biological systems like protozoae and viruses. Also, the half–cell potentials now become dominated by the unpredictable, poorly reversible surface reactions due to other ions in the solution and trace impurities in the silver, causing electrode polarization. However, used properly, Ag/AgCl electrodes possess the advantages of reversibility, little polarization and predictable constant junction potential *[Standen et al., 1987]*.

2.4 Electromagnetic Isolation

Stable low–noise measurement of current in the nanoampere range is a difficult task. It can often be impaired due to intrinsic instrument noise and sources of extraneous electrical interference. The latter can be divided into three main categories: radiative electrical pickup, magnetically–induced pickup and ground–loop noise.

Radiative Electrical Pickup

Examples of radiative electrical pickup include line frequency noise from lights (lab light, microscope light) and power sockets (hum), and high frequency noise from computers. This type of noise is usually reduced by placing conductive shields around the current–leading components. These shields are connected to the ground of the MEA. Another way to avoid radiative pickup is often just powering off all devices whose function is not necessary for the experiment.

Magnetically Induced Pickup

Magnetically induced pickup noise arises whenever a changing magnetic flux cuts a loop of wire, thereby inducing a current at the wire. It most often originates in the vicinity of electromagnets in power supplies, and is usually identified by its non–sinusoidal shape with a frequency that is a higher harmonic of the line frequency. This type of interference is reduced by moving power supplies away from sensitive circuitry. Again, reducing this type of noise can often be reached by simply turning off unused laboratory equipment.

Ground–Loop Noise

Ground–loop noise arises when shielding is grounded at more than one place. Magnetic fields may induce currents in this loop. Moreover, if the different grounds are at slightly different potentials, a current may flow through the shielding and introduce noise. In principle, ground loops are easy to eliminate: all shields must be connected and then be grounded at one connector only (most preferably at the signal ground of the MEA) *[Morrison, 1977; Horowitz and Hill, 1988]*.

2.5 Phase–Sensitive Detection

Since signals are often influenced by uncontrollable environment influences, the observed signal is often limited to a specific frequency component. This can very efficiently be done using the lock–in technique *[*Stanford Research Systems Inc.*, 2002]*. The lock–in technique is one of the most important correlation procedures. It implies a method known as *phase–sensitive detection* (PSD). Here, the signal of interest is modulated at a specific frequency and the resulting correlation function is analyzed to single out the amplitude and phase of the signal with a bandwidth down to 0.01 Hz.

Typically, the signal is modulated at a fixed frequency ω_r (the reference frequency). In figure 2.3 the reference signal is a square wave. The resulting signal might be a periodic function, like the sinusoidal signal waveform shown.

The reference waveform is $V_\mathrm{ref} \sin(\omega_\mathrm{r} t)$ and the signal is $V_\mathrm{sig} \sin(\omega_\mathrm{r} t + \vartheta_\mathrm{sig})$ where V_ref and V_sig are the references and signals amplitude. The internal generated (locked–in) reference signal is $V_\mathrm{ref} \sin(\omega_\mathrm{r} t + \vartheta_\mathrm{ref})$. During PSD, the signal is multiplied by the

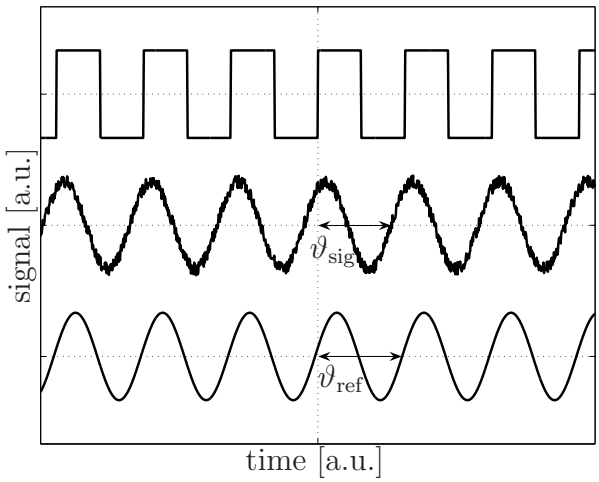

Figure 2.3: Examples of signal waveforms involved in phase–sensitive detection. Reference– (top), signal– (center) and internal lock–in reference (bottom).

internal reference waveform. The output of the phase–sensitive detector is then

$$\begin{aligned} V_{\mathrm{PSD1}} &= V_{\mathrm{sig}} V_{\mathrm{L}} \sin\left(\omega_{\mathrm{r}} t + \vartheta_{\mathrm{sig}}\right) \sin\left(\omega_{\mathrm{L}} t + \vartheta_{\mathrm{ref}}\right) \\ &= 1/2 V_{\mathrm{sig}} V_{\mathrm{L}} \cos\left(\left[\omega_{\mathrm{r}} - \omega_{\mathrm{L}}\right] t + \vartheta_{\mathrm{sig}} - \vartheta_{\mathrm{ref}}\right) - \\ &\quad 1/2 V_{\mathrm{sig}} V_{\mathrm{L}} \cos\left(\left[\omega_{\mathrm{r}} + \omega_{\mathrm{L}}\right] t + \vartheta_{\mathrm{sig}} + \vartheta_{\mathrm{ref}}\right) \end{aligned} \tag{2.5.1}$$

The PSD output results in two AC signals, one at the difference frequency $(\omega_{\mathrm{r}} - \omega_{\mathrm{L}})$ and the other at the sum frequency $(\omega_{\mathrm{r}} + \omega_{\mathrm{L}})$. If this signal is passed through a low pass filer, the AC signals will be removed. In the general case, the filter output will be zero. But for $\omega_{\mathrm{r}} = \omega_{\mathrm{L}}$, the difference frequency component of the PSD output will be a DC signal and be able to pass the low pass filter. In this case, the filtered PSD output will be

$$V_{\mathrm{PSD1}} = 1/2 V_{\mathrm{sig}} V_{\mathrm{L}} \cos\left(\vartheta_{\mathrm{sig}} - \vartheta_{\mathrm{ref}}\right). \tag{2.5.2}$$

Signal input at frequencies very close to the reference frequency will result in very low frequency AC outputs from the PSD. Their attenuation depends upon the lowpass filter bandwidth and roll off (excess bandwidth).

The PSD output is proportional to $V_{\mathrm{sig}} \cos\vartheta$ where $\vartheta = (\vartheta_{\mathrm{sig}} - \vartheta_{\mathrm{ref}})$. ϑ is the phase difference between the signal and the reference oscillation. Thus, manual adjustment of ϑ_{ref} can make ϑ equal to zero in which case V_{sig} can directly pass the PSD and filter due to $\cos\vartheta = 1$. Conversely, if ϑ is equal to $\pi/2$, there will be no output of the PSD. This phase dependency can be eliminated by adding a second PSD. If the second PSD multiplies the signal with the reference oscillator shifted by $\pi/2$, i.e.

$V_{\mathrm{L}} \sin(\omega_{\mathrm{L}} t + \vartheta_{\mathrm{ref}} + \pi/2)$, its low pass filtered output will be

$$V_{\mathrm{PSD2}} = 1/2 V_{\mathrm{sig}} V_L \sin(\vartheta_{\mathrm{sig}} - \vartheta_{\mathrm{ref}}). \tag{2.5.3}$$

The two quantities V_{PSD1} and V_{PSD2} represent the signal as a vector relative to the reference oscillator. By considering the signal as the magnitude R of this vector, the phase dependency is removed:

$$\begin{aligned} R &= \left[\left(1/2 \left(V_{\mathrm{sig}} V_{\mathrm{L}} \cos(\vartheta_{\mathrm{sig}} - \vartheta_{\mathrm{ref}})\right)^2 + \left(V_{\mathrm{sig}} V_L \sin(\vartheta_{\mathrm{sig}} - \vartheta_{\mathrm{ref}})\right)^2\right)\right]^{1/2} \\ &= \left(V_{\mathrm{PSD1}}^2 + V_{\mathrm{PSD2}}^2\right)^{1/2}. \end{aligned} \tag{2.5.4}$$

2.6 SICM Control Signal and Transfer Function

In SICM, the distance control signal is provided by the conductivity of solvated ions that are drifting through the aperture of a nanopipette. The driving force of this drift is the gradient of the potential applied by the two electrodes, inside and outside of the pipette. Since the narrow aperture and the conical geometry of the pipette, applying a potential V_0 between the two electrodes results in a potential drop that occurs mainly in the region of the pipette tip *[Ying et al., 2004]*. Assuming that the electric field is not affected by surface charges and that there is no change in the ion current throughout the pipette length, the potential can be given by

$$dV(z) = -I_{\mathrm{DC}}\, d\rho(z) = -\frac{I_{\mathrm{DC}}}{\pi\sigma \left(R_0 + z\tan\theta\right)^2}\, dz, \tag{2.6.1}$$

where ρ is the pipette resistance, z is the distance from the tip, σ is the conductivity of the electrolytic solution, R_0 is the radius of the tip opening, and θ is the half–cone angle of the inner wall of the pipette. Integrating eq. 2.6.1 gives

$$\rho = \frac{1}{\pi\sigma R_0 \tan\theta}, \tag{2.6.2}$$

and

$$V(z) = \frac{V_0 R_0}{R_0 + z\tan\theta}. \tag{2.6.3}$$

Then the electric field in the z–direction inside the pipette is

$$E(z) = \frac{dV(z)}{dz} = \frac{V_0 R_0 \tan\theta}{\left(R_0 + z\tan\theta\right)^2}. \tag{2.6.4}$$

The shape of the electric field (figure 2.4) is highly asymmetrical with respect to the tip opening ($z = 0$) and the highest magnitude will be inside the pipette at very short distances from the tip opening.

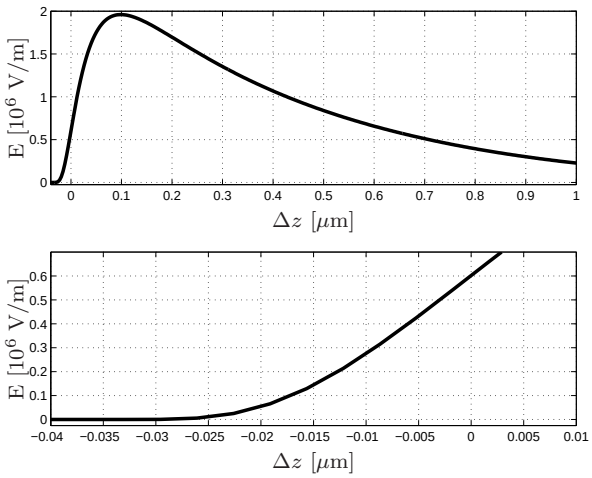

Figure 2.4: Draft of the electric field magnitude inside and outside of a borosilicate–pipette with inner diameter of 100 nm, 6° cone angle, and 1 V applied potential. Top: Overview. Bottom: Detail of the electrical field magnitude at proximity of the tip. The field inside of the pipette is calculated according to eq. 2.6.4, the field magnitude outside of the pipette can be simulated with a finite element approach *[Ying et al., 2004]*.

Here, it reaches values of about 10^6 V m^{-1} and sharply decreases to zero outside the aperture. Nevertheless, a small magnitude of electric field can be found in the first few tens of nanometers outside of the pipette. This part of the electric field can have dielectric interactions with matter in the proximity of the pipette aperture. A surface, for example, perpendicular with respect to the pipette axis and at a distance of about the opening radius will significantly bend the streamlines of the electric field.

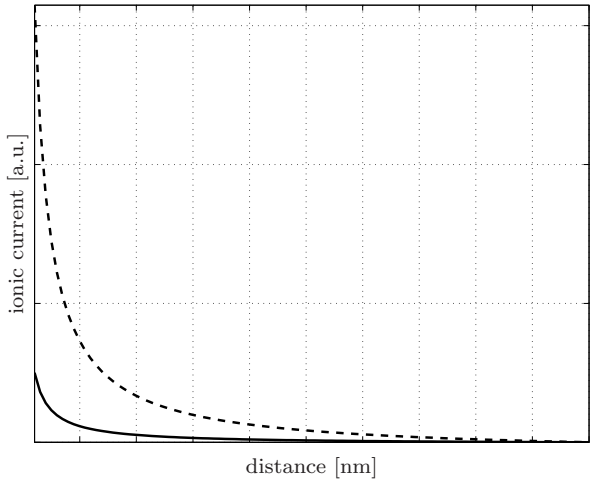

Figure 2.5: Ionic current as a function of the tip–sample distance. Solid line: $1 - I_{ion}^{DC}$. Dashed line: I_{ion}^{AC}. The curves are calculated from equations 2.6.5 and 2.6.6, with $I_{sat} = 10^{-9}$, $r_0 = 200$ nm, $a = 100$ nm and $L = 2$ μm *[Pastre et al., 2001]*. Notice the relation between the gradient dI_{ion}^{DC}/dz and the gradient of I_{ion}^{AC}, dI_{ion}^{AC}/dz. The steeper signal $I_{ion}^{AC}(z)$ is much more sensitive to distance changes than the DC–signal.

This effect corresponds to a decrease of the effective area A that the ionic current density $\mathbf{j}_{ion}$ is passing, thus equivalent to a decrease of the ion conductance of the microelectrode system. The dependency between the tip–sample distance z and the

ionic current $I_{\text{ion}}^{\text{DC}}$ through the pipette can be estimated by

$$I_{\text{ion}}^{\text{DC}}(z) = I_{\text{sat}} \left(1 + \left(\ln\left(r_0/a\right) a r_0\right) / \left(Lz\right)\right)^{-1} \tag{2.6.5}$$

[Bard et al., 1990; Pastre et al., 2001], with the saturation current I_{sat}, inner tip opening radius a, outer tip opening radius r_0 and the length L of the tapered pipette end. If the distance between the sample and the tip is oscillated periodically at frequency ω and amplitude d, the amplitude of the modulated ionic current signal detected by the phase–sensitive detectors (compare section 2.5) can be calculated with the following equation:

$$I_{\text{ion}}^{\text{AC}}(z) = \int_0^{\text{T}} I_{\text{ion}}^{\text{DC}}(z + d\sin\left(\omega t\right)) \sin\left(\omega t\right)\ dt, \tag{2.6.6}$$

where $T = 2\pi/\omega$ is the period of modulation.

2.7 Feedback Control Theory

Proportional (P) Feedback Control

Control is the process of making a system variable adhere to a particular value, called the *reference value* r or *setpoint*. In *open-loop control* the system does not sensor the process output y, and there is no compensation of that output to make it conform to the reference value. In *closed loop control* or *feedback control* systems the variable being controlled is measured by a sensor, and the information is fed back to the process to influence the controlled variable.

The feedback transfer function $H(s)D_{\text{y}}(s)$ (with $H(s), D_{\text{y}}(s)$ as the feedback components of sensor transfer function and dynamic compensation, respectively) typically represents the sensor action to convert the output $y(t)$ to an electrical output signal $b(t)$. Likewise, the transfer function $D_{\text{r}}(s)$ is often required to convert the reference input into an electrical signal that combines with $b(t)$ in the controller to generate the actuating signal $a(t)$. The controller with transfer function $D(s)$ converts the electrical actuating signal into the control signal $u(t)$. This signal fed back into the process is transformed by the process–intrinsic transfer function $G(s)$. Additional to the process and sensor signals there are disturbances w and sensor noise v that contribute to the control system.

If the feedback control signal u is made to be linearly proportional to the error e in the measured output, the control is called *proportional feedback*. The general form of proportional control is

$$u = Ke. \tag{2.7.1}$$

The functional context between input and output of the feedback controll is called the controller *transfer function* $D = D(s)$. In the case of proportional feedback the transfer function is simply given as

$$D(s) = K. \tag{2.7.2}$$

The proportional feedback controller can be regarded as an amplifier and may have a steady–state offset in response to a constant reference input and may not be entirely capable of rejecting a constant disturbance *[Franklin et al., 1994]*. For higher–order systems, large values of the proportional feedback gain will typically lead to instability.

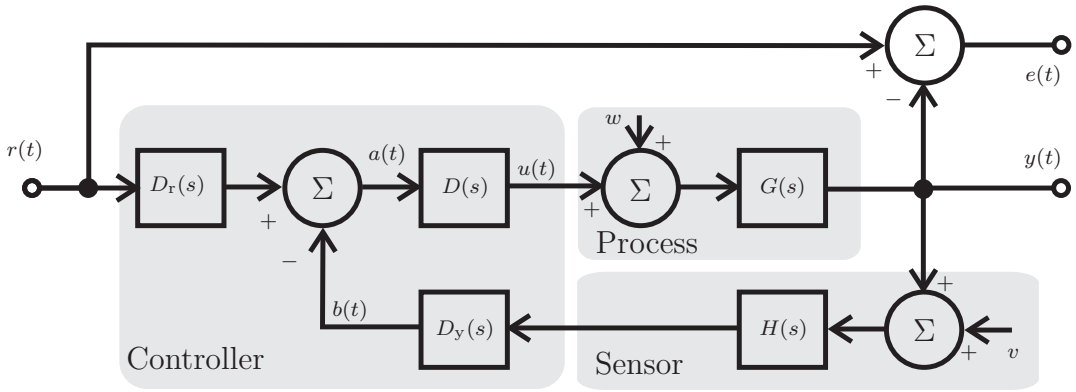

Figure 2.6: Block diagram of a feedback control system. The reference r is compared to the process output y. The controllers output u manipulates on the input of the process to minimize the error $e = y - r$. Further information will be found in the text.

For most systems there is an upper limit on the proportional feedback gain in order to achieve a well-damped stable response and this limit may still have an unacceptable steady–state error. One way to improve the steady–state accuracy of control without adding extremely high proportional gains is to introduce integral control.

Proportional–Integral (PI) Feedback Control

The primary reason for integral control is to reduce or eliminate steady–state errors, but this benefit typically comes at the cost of worse transient response. Proportional–Integral feedback has the form

$$u(t) = \frac{K}{T_{\mathrm{I}}} \int_{t_0}^{t} e \, d\tau. \tag{2.7.3}$$

Therefore, the transfer function becomes

$$D(s) = \frac{K}{T_{\mathrm{I}} s}, \tag{2.7.4}$$

where T_{I} is called the *integral*, or *reset time*, and $1/T_{\mathrm{I}}$ is a measure of the speed of response and is referred to as the *reset rate*. T_{I} is the time for the integrator output to reach K with an input of unity.

Proportional–Derivative (PD) Feedback Control

Derivative feedback has the form

$$u(t) = K T_{\mathrm{D}} \frac{d}{dt} e. \tag{2.7.5}$$

Therefore the transfer function $D(s)$ becomes

$$D(s) = K T_{\mathrm{D}} s, \tag{2.7.6}$$

and T_{D} is called the *derivative time*. It is used in conjunction with proportional and/or integral feedback to increase the damping and generally improve the stability of a system. Derivative feedback is not used by itself, because if $e(t) \neq 0$ remained constant, the output of a derivative controller would be zero ans a proportional or integral term would be needed to provide a control signal at this time.

In the derivative control the correction depends on the rate of change of the error. As a result, a controller with derivative control exhibits an anticipatory response: proportional–derivative behavior leads the proportional–only action by T_{D} seconds.

Proportional–Integral–Derivative (PID) Feedback Control

For control over steady–state and transient errors all three control strategies can be combined to get *proportional–integral–derivative* control. Here the control signal is a linear combination of the error, the time–integral of the error and the time rate of the error. The controller transfer function is given by

$$D(s) = K\left(1 + \frac{1}{T_{\mathrm{I}}s} + T_{\mathrm{D}}s\right). \tag{2.7.7}$$

Designing a control feedback loop inhibits adjusting K, T_{I} and T_{D} in equation 2.7.7.

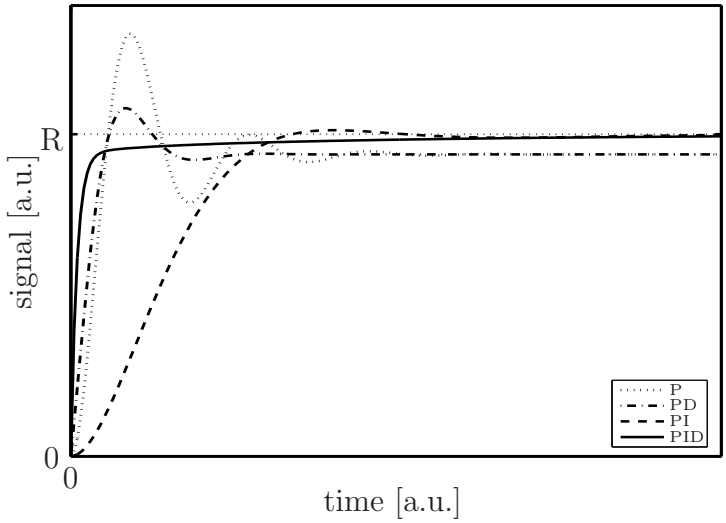

Figure 2.7: Plot of different control design qualitatively temporal behaviors (simulated). P control: Steady–state error, large overshoot. PD control: reduced overshoot and settling time. PI control: eliminated steady–state error. PID control: no overshoot, fast rise time, and no steady-state error. R: reference value.

This procedure is called *tuning* the controller. Increasing K and $1/T_{\mathrm{I}}$ tends to reduce system errors but may not be capable of also producing adequate stability, while increasing T_{D} tends to improve stability.

The efficiency of PID control depends on the slope of the transfer function that transfers from alternations in the input of the system to corresponding alternations of its output. Thus, K can be considered as consisting of a product of the transfer functions slope m and a chosen parameter K. It becomes clear that only if m is constant over the whole dynamic range of the controller a stable feedback control is possible. If the transfer function is not linear, it can be normalized for linearization of the control.

2.8 Real–Time Computing

In computer science, real–time computing means the application of hardware and software that facilitate preservation of temporal conditions for giving predictable process

performance. This requires special software like real–time operating systems (RTOS) as well as real–time capable hardware.

General purpose operating systems like Microsoft Windows and Apple Mac OS are optimized to run a variety of applications simultaneously, ensuring that all applications receive some processing time. These operating systems must also respond to interrupts from peripherals such as the mouse and keyboard. The user has limited control regarding how these tasks are handled by the processor. As a result, high-priority tasks can be preempted by lower priority tasks, making it impossible to guarantee a response time for processes and applications.

In contrast, real-time operating systems give the ability to prioritize tasks so that the most critical task can always take control of the processor when needed. This property enables one to program an application with predictable results. Real-time operating systems are originated with the need to solve two main types of applications: event response, and closed loop control systems. Event response applications require a response to a stimulus in a determined amount of time, an example of such a system is an automotive airbag system. Closed loop control systems continuously process feedback in order to adjust an output. Both of these types of systems require the completion of an operation within a specific deadline. This type of performance is referred to as determinism.

The most common misconception associated with real-time performance is that it increases the execution speed of applications. While this is true in some cases, it actually enhances applications by providing more precise and predictable timing characteristics. With these enhancements, determination of the exact time for certain events to occur is facilitated.

Determinism measures the consistency of the specified time interval between events. Many control algorithms, such as PID, require very deterministic behavior. For example, an elevator gradually moves to the correct floor because of the deterministic behavior of the control loop. Without the determinism, the elevator would still reach the correct floor but without temporal stability. With all real-time systems, there is some amount of error called jitter. Jitter is another way of measuring the determinism of a real-time system. It can be calculated as the maximum difference between any individual time delay and the desired time delay in a system.

3 Experimental Materials and Methods

The SICM is used to perform a mechanical study of a sample's surface resulting in topographical information. In addition to the topographical information, optical information of the sample can be gathered simultaneously to the topographical scanning process by means of optical microscopy. In this work, the development of a SICM is presented that can be combined with a variety of optical microscopy techniques. As will be explained in this chapter, this combination requires a different setup than that one would design specialized for scanning ion–conductance microscopy only. In this chapter, a detailed description of the hardware and software used in the experimental setup is given.

3.1 Experimental Setup Environment

For improved mechanical stability, the SICM is set up on top of an optical table (Model RS–4000, Newport Corporate, Irvine CA, USA). This table efficiently eliminates table–intrinsic torsional and bending vibration modes. It is equipped with eight I–2000 pneumatic isolators with automatic leveling, with a 99% isolation against vertical oscillations at frequencies above 10 Hz. The scanning ion–conductance microscope is established as a modification of a commercial inverted optical microscope (Model IX70, Olympus Optical Co. Ltd., Tokyo, Japan). Usage of this kind of microscope facilitates that optical microscopy can be applicated during SICM topography scans. Moreover, an inverted microscope eases access to the scanned probe since the area straight above the sample area of the microscope is clear. This free area is used for

the SICM that is mounted as an extension onto the frame of the IX70. A schematic presentation of the combination of the SICM and the optical (fluorescence) microscope is shown in figures 3.1 and 3.2. The SICM yields information about the surface of the

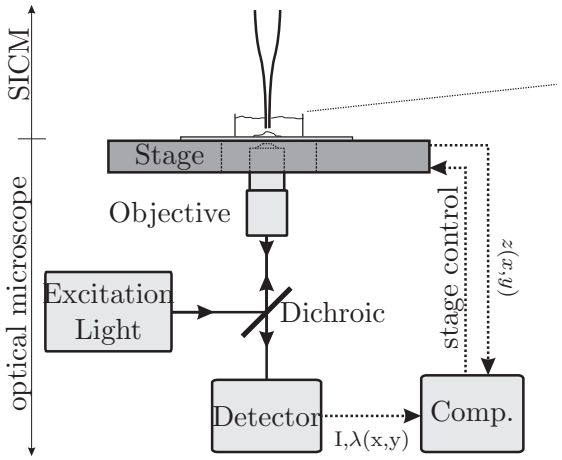

Figure 3.1: Combining SICM and fluorescence microscopy. The scanned sample is located between the SICM probe and the microscope objective. Mechanical SICM imaging is performed from above, while fluorescence analysis is done from below. The only moving part is the scanning stage controlling the samples position with respect to the probe and the objective focus.

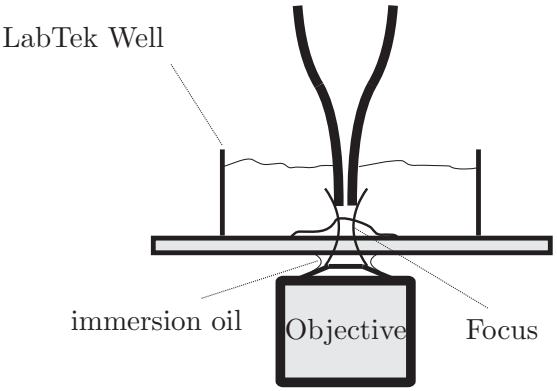

Figure 3.2: Detailed view on the location of the scanned sample. Only the sample and the LabTek well are being moved.

sample by probing its topography from the upside. This results in an image matrix $z = z(x, y)$. For gathering optical information about the sample, the same area (x,y) can be probed by confocal fluorescence microscopical from below, additionally giving fluorescence information I=I(x,y).

In confocal fluorescence microscopy, the collimated beam of an excitation light source is adjusted into the back focal plane of the microscope objective. By moving the objective, the excitation light can be focused into the sample under examination so that it forms a detection volume. Molecules located in this detection volume can be optically excited into higher energetic levels by absorbing an excitation photon $\hbar\omega_{\mathrm{ex}}$ ($S_0 + \hbar\omega_{\mathrm{ex}} \rightarrow S_1$). Then, among other relaxation processes, there is a certain probability of relaxing by spontaneous emission of a fluorescence photon $\hbar\omega_{\mathrm{fl}}$ ($S_1 \rightarrow S_0 + \hbar\omega_{\mathrm{fl}}$). Because of the Stokes shift, the fluorescence wavelength is larger than the excitation wavelength, so that the fluorescence light emitted from the detection volume can be separated from the excitation light. After that the fluorescence signal is analyzed by a sensitive detector.

Further information about fluorescence techniques can be found in *[Lakowicz, 1999]*.

In the presented setup, the excitation light can be provided by either a combination of a high-pressure mercury lamp and corresponding optical filter or a laser system emitting light of suitable wavelength. Detection of the fluorescence light can be done in two ways. For sensitive detection of even single fluorescence photons, an avalanche photo diode (APD) can be used (SPCM AQR-15, PerkinElmer MA, USA). Connected to a time–correlated single photon counting (TCSPC) module (SPC830, Becker und Hickl, Berlin, Germany), the APD gives fluorescence information via a photon–rate over time trace that has to be re–correlated to the samples position to give a fluorescence map. A different approach can be made by detecting the fluorescence by using an EMCCD camera (Ixon EM+855, Andor, USA). While for confocal imaging the fluorescence image is constructed by re–correlation of an intensity time trace, using a camera means making parallel imaging of the whole image matrix. Since therefore the whole image area must be illuminated by the excitation light, a modification in the optical pathway geometry is necessary. That is the collimated excitation light is focused onto the objectives back focal aperture to give a Gaussian excitation profile illuminating the sample surface with large diameter. In this so called defocused laser excitation, the sample is illuminated by a nearly homogeneous excitation profile.

3.2 Glass Capillaries

The scanning probe is a glass–nanopipette that is produced in situ immediately prior to use. During this procedure, a glass barrel made of either fused silica (SiO_2) or Borosilicate, a compound of SiO_2, B_2O_3, Na_2O, K_2O, and Al_2O_3 is simultaneously melted and pulled with a laser–based programmable nanopipette puller (Model P-2000, Sutter Instrument, Novato CA, USA). The P–2000 nanopipette puller is designed for use with aluminosilicate, borosilicate (or other lower melting point glass) and Quartz (fused silica) tubing or fiber ranging from 0.125 mm to 1.5 mm in diameter.

Borosilicate

The borosilicate–glass[1] is purchased (Science Products GmbH, Hofheim, Germany) as hollow cylinders of 80 mm in length. The outer diameter O.D. is 1.00 mm while

[1] Schott 8340

the inner diameter I.D. can be either 0.78 mm or 0.58 mm. To prevent sharp edges that could be harmful to the insulation of inserted electrodes silver wire, the ends of borosilicate capillaries can be fire polished. As an option for easier back–filling of the pulled micropipettes, a thin glass–filament with a diameter of some ten microns is attached at the inner surface. This glass softens at 825 degrees Celsius and, as it is pulled, maintains its ratio of inside diameter to outside diameter over the total taper length. The influence of the glass filament inside the barrel on the shape of the pipette tip has not been investigated during this work. Because of its dielectric constant of 4.6 at 25° C and a loss factor of $3.7 \cdot 10^{-3}$ *[*Schott Rohrglas GmbH*, 2007]*, the electric noise occurring due to the dielectrics of borosilicate pipettes will be significantly larger than that of fused silica *[*Molecular Devices Corp.*, 1999]*.

Item Nr.	**Outer Dia.**	**Inner Dia.**	**Length**	**Filament**	**Ends**	**Material**
GB100-8P	1.00 mm	0.58 mm	80 mm	no	fire–polished	borosilicate
GB100T-8P	1.00 mm	0.78 mm	80 mm	no	fire–polished	borosilicate
GB100F-8P	1.00 mm	0.58 mm	80 mm	yes	fire–polished	borosilicate
GB100TF-8P	1.00 mm	0.78 mm	80 mm	yes	fire–polished	borosilicate
Q100-50-7.5	1.00 mm	0.50 mm	75 mm	no	cutted	fused silica
Q100-70-7.5	1.00 mm	0.70 mm	75 mm	no	cutted	fused silica
QF100-70-7.5	1.00 mm	0.70 mm	75 mm	yes	cutted	fused silica
QF100-70-7.5	1.00 mm	0.70 mm	75 mm	yes	fire–polished	fused silica

Table 3.1: Listing of types of glass used for pipette fabrication in this work. In most experiments, GB100F-8P type borosilicate glass was used.

Fused Silica

Fused silica[2] is purchased (Science Products GmbH, Hofheim, Germany) as hollow cylinders of 75 mm length with an outer diameter of 1.00 mm and an inner diameter of 0.7 mm. Like borosilicate, fused silica with an inner filament for easier filling is available. Because of the high softening temperature of 1.580° C *[*Molecular Devices Corp.*, 1999]*, fused silica offers the possibility of making pipettes with extreme small opening

[2]Heraeus HSQ300

diameters (below 15 nm are possible with 1.0 mm O.D. and 0.5 mm I.D. fused silica barrels *[*Sutter Instrument Company*, 1999; Shevchuk et al., 2006]*). Fused silica shows a dielectric constant of 3.8 at room temperature, and with the smallest loss factor of all glasses, fused silica offers far lower dielectric noise than borosilicate glass does.

As an overview, see table 3.1 for information about glass types used in this work.

3.3 Nanopipette Puller

The glass tubing to be pulled can be cleaned before pipette fabrication by rinsing with pure alcohol and deionized water and subsequent drying. This removes (fingerprint–)oil and dirt from the glass-surface that could otherwise be critical to the reproducibility of the pipettes geometry as well as harmful to the pullers retro–reflective mirror. The glass barrel is afterwards symmetrically clamped into the two pulling bars of the P–2000 puller. Both pulling bars apply a moderate pulling force onto the glass in parallel with the glass cylinder axis of rotation. The light of a CO_2–laser melts the glass while the soft pull is drawing out the glass. As the viscosity of the melting glass decreases, the velocity of the moving bars increases until a pre–defined velocity is reached. At this point, which is called the *trip–point*, the heating is turned off and after a programmable delay between -128 ms and 128 ms the pulling force is strongly increased. This *hard pull* leads to the formation of two pipettes whose shape (inner tip diameter and taper length) depends on the setting of the parameters in the pulling program, which are:

- HEAT – This parameter specifies the output power of the laser, and consequently the amount of energy supplied to the glass. The HEAT required to melt a piece of glass is a function of the 'FILAMENT' that has been selected and the particular glass size and composition. Generally changes to HEAT will be made in steps of about 10 units since in most cases smaller changes will have little effect.
- FILAMENT (FIL) – specifies the scanning pattern of the laser beam that is used to supply HEAT to the glass. The P-2000 is preprogrammed with 6 different scanning patterns (FILAMENTS), each of which defines the longitudinal length and the rate of the scan.
- VELOCITY – The VELOCITY adjustment allows for the selection of a precise glass temperature as the trip point for the hard pull. One unit represents a change of one or more millivolts of transducer output depending on the transducer being used.

- PULL – This parameter controls the force of the hard pull. In general, the higher the pull, the smaller the pipette tip diameter and the longer the taper. A change of one unit represents a change of 4 mA of current through the pull solenoid. Changes in PULL strength of 10 units or more are typically required to see an effect.
- DELAY – The DELAY parameter controls the time between when the HEAT turns off and when the hard PULL is activated. The higher the DELAY value, the cooler the glass will be when the hard PULL is executed. Thus, increasing the DELAY results in decreased taper length and increased tip diameter. The range of DELAY values (0-255) is timed to allow the hard pull to be initiated at the same time as the deactivation of the laser when the DELAY value = 128. If the DELAY value is greater than 128, the hard pull will be initiated after the deactivation of the laser. If the DELAY value is less than 128, the hard pull will be initiated before the deactivation of the laser.

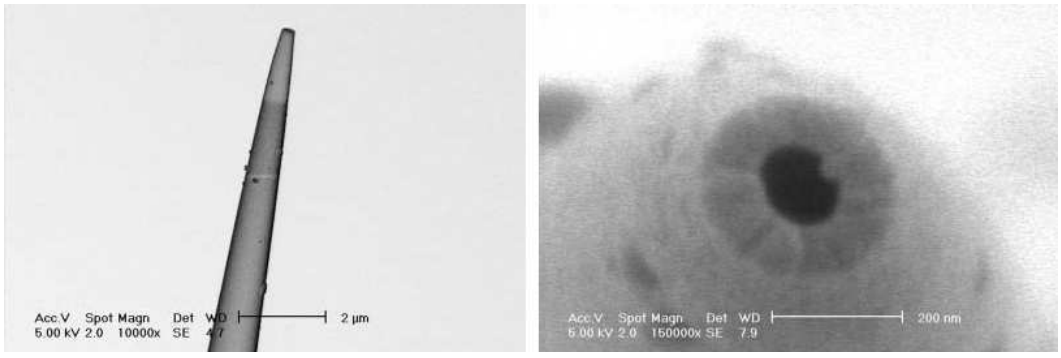

Figure 3.3: Scanning electromicrographs of the nanopipette tip coated with 5 nm of gold. The scale bar is 2 μm (left) and 200 nm (right), respectively. *[Ying et al., 2004].*

3.4 Filling Nanopipettes

Filling the electrodes with electrolytic solution is not straight–forward. Because of the extremely small aperture size, interactions between the solution and the glass surface tend to prevent the solution from entering the tip due to capillary forces. For tip aperture diameters below approximately 100 nm it is almost impossible to completely fill the pipette with electrolytic solution. As a practical remedy, glass tubing with a thin glass filament fused inside the lumen are used for pulling pipettes. When the pipette

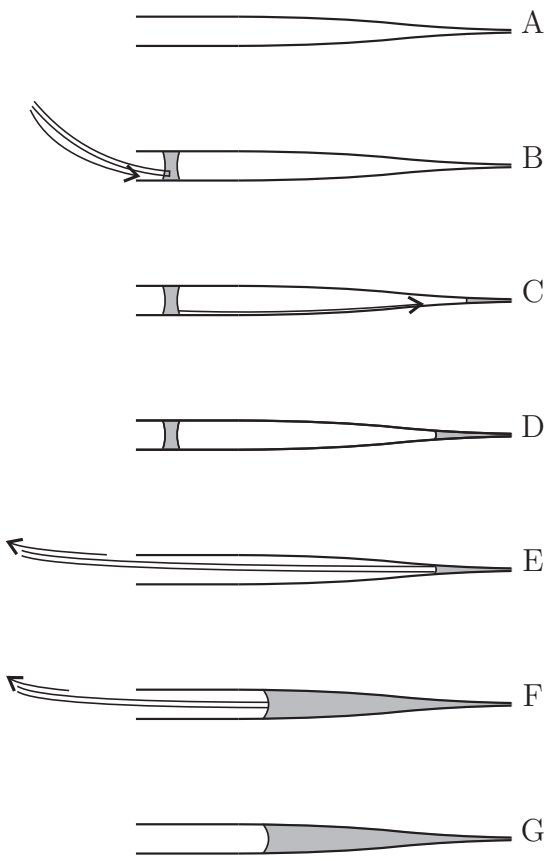

Figure 3.4: Filling nanopipettes. The pulled pipette (A) is back–filled (B) with some μl of the solution (grey) using a microloader. Due to the glass–internal fibre, within some seconds the solution tracks right down to the tip (C) until the tip is visibly filled with solution (D). By further insertion of solution into the tip region and successive rejection of the microloader (E,F), the bulk of the pipette can be filled as far as is necessary for contacting the solution with the inner silverchloride–electrode (G). Care must be taken to avoid formation of gas bubbles.

is pulled, their cross–section shape is preserved up to the tip. Using fiber-containing capillary, pipettes can be backed-filled with small amounts of solution. This back–filling is done with the help of microcapillaries (Microloaders, Eppendorf, Hamburg, Germany). Within some seconds, the solution tracks down the channels formed on either side of the fiber right down to the tip. After waiting for the tip to be filled with solution, the microloader is used to fill the bulk of the pipette. Only as much solution is filled into the bulk as is necessary for securing electrical contact with the inner electrode. To prevent harmful leaking currents into the pipette holder it is important that the outside of the pipette stays dry and clean. Air bubbles inside the pipette must be avoided by carefully positioning the microloader during the filling process.

3.5 Electrodes

Silverchloride electrodes used for insertion into nanopipettes are made by chlorination of tetrafluroethylene–resin (TFE) coated silver wire (Cat.–Number 786500, A–M Sys-

tems Inc., Carlsborg WA, USA). A silver–wire of 200 μm diameter, coated with an insulating layer of 80 μm TFE is cut into a part of about 40 mm length (Fig. 3.5). One end is chlorined for about 30 minutes in a sodium hypochlorite solution resulting in a formation of a 0.28 mm diameter circular–shaped Ag/AgCl electrode. Here, the chemically inert TFE protects the excess surface of the silver from getting into contact with the chloride solution. At the other end of the wire the TFE–coating is removed within about 5 mm before 1 mm of the bare silver is bended over to an angle of 90° to give good and stable electrical contact with the headstage–amplifier. The grounding electrode that connects the electrolyte solution with the grounding plug of the headstage, is a commercially sintered silver–chloride electrode (Model E-205 Ag/AgCl–Pellet, In Vivo Metric, Healdsburg CA, USA). Here, a AgCl–barrel of 1.0 mm dia. $\times$ 2.5 mm length is sintered onto a 0.25 mm diameter silver–wire.

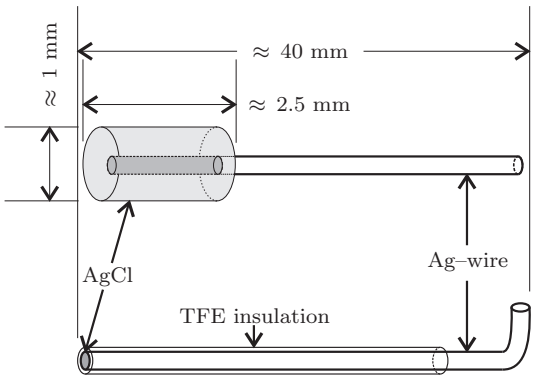

Figure 3.5: Top: Grounding silver-chloride electrode. Sintered AgCl pellet on silver wire. **Bottom:** Silverchloride electrode preparated for insertion into nanopipette. One end of the TFE–insulated silver–wire (0.2 mm silver with 0.08 mm TFE–coating) is cutted and chlorinated in 13 % NaClO–solution resulting in a circular shaped Ag/AgCl electrode tip. The other end is bare silver, rectangularly bended to establish an electrical contact with the headstage amplifier.

3.6 Electrolytic Solution

The electrolytic solution used for non–physiological measurements constists of phosphate buffered saline (PBS, Sigma-Aldrich Chemie GmbH, Munich, Germany). One tablet is dissolved in 200 ml of deionized water and yields 10 mM phosphate buffer, 2.7 mM potassium chloride and 137 mM sodium chloride, pH 7.4, at 25 °C.

3.7 Manual Probe Positioning System

Prior to an experiment, manually positioning of the scanning probe relatively to the scanned sample is performed by means of a high–precision multi–axis positioning system (Model M-562 XYZ ULTRAlign, Newport Corporate, Irvine CA, USA).

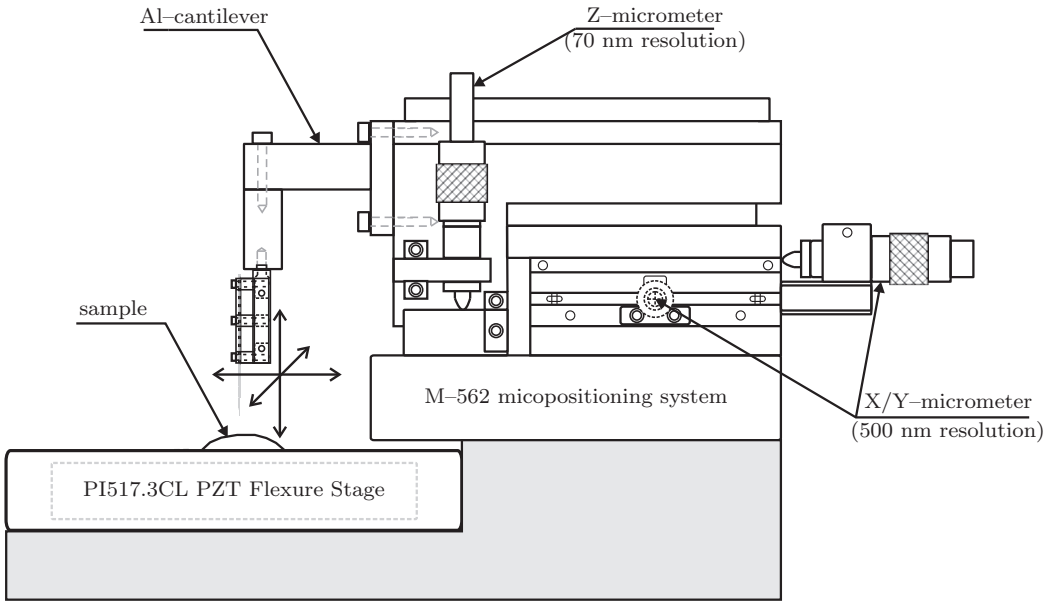

Figure 3.6: Probe positioning system. The scanning probe with its holder can manually be positioned according to the position of the probe by a M–562 multi–axis positioning system. Lateral positioning is controlled by HR–13 lockable high–resolution micrometers. The vertical position can be changed with a 70 nm resolution over a DM–13 differential micrometer. Maximum travel in all directions is 13 mm.

The piezo–stack and the pipette holder are directly attached to the M-562 over an aluminium cantilever with a length of 55 mm having a quadratic profile of 15×15 mm^2. (see figure 3.6). Lateral movement of the M–562 system is controlled over a lockable micrometer (Model HR–13, Newport Corp.). These high-resolution micrometers have 0.25 mm pitch threads, providing 0.5 μm sensitivity with direct position readout in 5 μm graduations. The HR Series Micrometers have a thumbscrew locking mechanism that clamps a non–threaded portion of the screw from all sides. This stress–balanced design secures the position with negligible displacement during locking. Vertical position control is done by a differential micrometer (Model DM–13, Newport Corp.). The DM–13 differential micrometer offers 13 mm overall range with 0.2 mm fine adjustment range at 0.07 μm resolution. Due to the micrometers used, the pipette tip position can

be adjusted withing a virtual cube of $13 \times 13 \times 13$ mm^3.

3.8 Scanning Piezo Flexure Stage

During scanning, the scanned sample has to be moved both in lateral (scanning) and in vertical (distance correction) directions with sub nm resolution. This is done by a 3–axis piezo flexure scanner (Model P–517.3CL, Physik Instrumente GmbH & Co. KG, Karlsruhe, Germany). With a travel of $100 \times 100 \times 20$ μm^3 (X $\times$ Y $\times$ Z), this scanner offers resolutions of 0.3 nm in lateral and 0.1 nm in vertical direction, respectively. Due to its low resonant frequency component of 1.1 kHz in vertical direction, this stage is not capable of performing highly dynamic movement. Driving of the piezo–stage is done by a three–channel amplifier for the low–voltage piezo–ceramics lead zirconium titanate, PZT, (E–503, PI). It contains three independent amplifiers that can each output and sink a peak current of 140 mA and an average current of 60 mA. The output voltages are controlled via analog output signals supplied by the DAC. Multiplication by the gain factor by 10 results in an output voltage range of -20 V to +120 V. A DC–offset potentiometer is active at the same time and produces an internal offset voltage of 0 V to 10 V added to the input signal.Due to integrated capacitive position feedback sensors (model D100.00, PI), closed–loop position control (and read–out) at sub–nm resolution and stability is realizable over an E–509.C3A servo–control module. This controller generates the input signal for the power amplifier module which actually drives the stage. It uses the difference between target position and the actual position in a servo–loop algorithm, compensating drift and hysteresis of the PZT system. The effective stiffness of the actuator is significantly increased due to the rapid displacement control effected by adjusting the PZT operating voltage so as to maintain the displacement even when external forces change.

3.9 Oscillating Piezo Actuator

For successfully application of the lock–in technique, the ionic current flowing through the pipette opening has to be modulated. This is done by periodically changing the pipette–tip to sample distance close to the surface. Because of the strong dependence of the ionic conducuctivity from the distance, only a nm–sized amplitude oscillation is adviced while the frequency should be as fast as possible to provide fast responsiveness

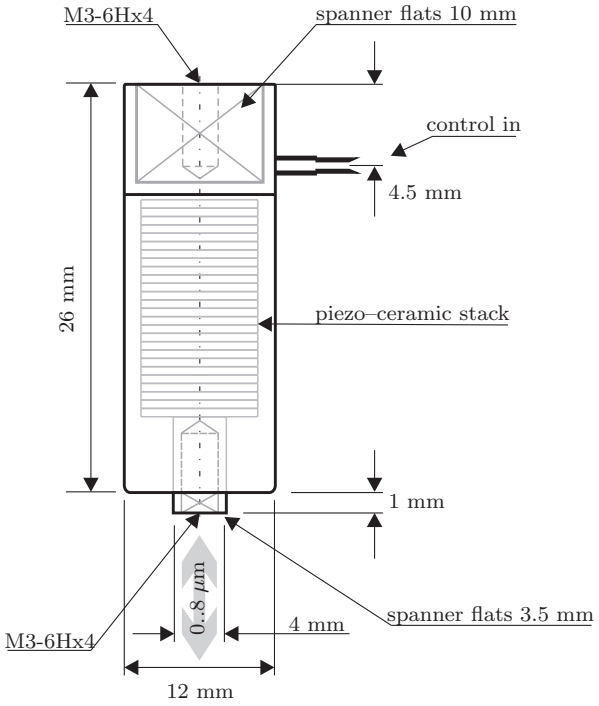

Figure 3.7: Drawing of PA 8/12 high–dynamic stack type piezo actuator used for kHz–oscillation of the scanning pipette and pipette holder.
Details *[*Piezo System Jena GmbH*, 2004]*:
Manufacturer: Piezosystem Jena
Nominal maximum motion: 8 μm
Pre–load: 300 N
Maximum voltage: 150 V
Maximum load: 850 N
Minimum load (tensile force): 300 N
Stiffness: 120 N/μm
Resonant frequency: 50 kHz
Resolution: 0.01 nm

of the lock–in detection cycle.

These requirements are met by a highly dynamic piezo actuator like the stack–type actuator PA8/12 (Piezosystem Jena, Jena, Germany, see figure 3.7). The PA8/12 actuator is internally preloaded by a mechanical spring making it ideal for dynamic applications. Due to its resonant frequency of 50 kHz and stiffness of 120 N/μm *[*Piezo System Jena GmbH*, 2004]*, it is capable of sinusoidally dynamics at up to 20 kHz frequencies. Typical frequencies in our experiments are 1 kHz to 2 kHz. Because of the pre–load of 300 N, moderate tensile forces (upside–down operation) are applicable to the actuator. Furthermore, the preload does allow for moderate shear–forces during application like they can appear in the way the piezo–system is used in this work. The shear forces occur due to torques arising from when the center of the oscillated mass is not exactly in–line with the axis of translation.

The PA8/12 piezoelectrical actuator is made of PZT (lead zirconium titanate). The stack consists of a large number of contacted ceramic discs. The electrodes are arranged on both sides of the ceramic discs and are connected in a parallel line. The breakdown voltage of the ceramic limits the maximum field strength. Normally, piezostacks work with a maximum field strength of 2 kV/mm.

The PA8/12 is connected to its power supply (ENV400, Piezosystem Jena, Germany) by a LEMO OS 250–connector and shielded cable. It is driven by internal operating

voltages ranging from -10 V to 150 V. With the 10 kΩ resistance, 0 to 10 V BNC–input MOD, the modulating control signal is applied from the lock–in amplifiers SINE OUT source to the piezo's power supply. This signal is internally translated into the operating voltage corresponding to a relative displacement z from 0 μm to 9.5 μm *[*Piezo System Jena GmbH, *2004]*. Obviously, the ratio between input signal potential ΔV and displacement Δz is given as

$$\Delta \mathrm{V}/\Delta \mathrm{z} = 1/0.95\ \mathrm{V}\mu\mathrm{m}^{-1} \approx 1.053\ \mathrm{V}\mu\mathrm{m}^{-1}, \tag{3.9.1}$$

and an input signal $V_{\mathrm{MOD}}(t)$ with

$$V_{\mathrm{MOD}} = 0.1 \cdot \sin(\omega t)\ \ [\mathrm{V}] \tag{3.9.2}$$

is resulting in a translation $z_{\mathrm{MOD}}(t)$ of approximately

$$z_{\mathrm{MOD}}(t) \approx 95 \cdot \sin(\omega t + \phi)\ \ [\mathrm{nm}] \tag{3.9.3}$$

with a phase shift between input modulation and output oscillation of ϕ.

3.10 Microelectrode Amplifier

Headstage Preamplifier

Measurement of the ionic current is performed by an *Axopatch 200B* (Axon Instruments, Molecular Devices Corporation, Union City CA, USA) microelectrode amplifier. This instrument is designed for patch–clamping experiments and therefore most of its circuitry is devoted to passively and actively eliminate noise from the current signal. Directly attached to the experimental location there is a slim designed ($1.8\times1.9\times10.5\,\mathrm{cm}^3$) preamplifier headstage *CV 203BU* that works as an operational amplifier measuring the ionic current through the pipette tip. It is provided with a gold–plated 1 mm socket connected to ground, which is used for grounding the preparation. This headstage is capable of working in two different measurement modes: resistive feedback and capacitive feedback. Patch–clamp headstages are current–to–voltage converters. That is, the voltage output is proportional to the current input. In contrast, conventional microelectrode amplifier headstages are voltage followers in which the voltage output corresponds to the voltage input. For an ideal operational amplifier the pipette current

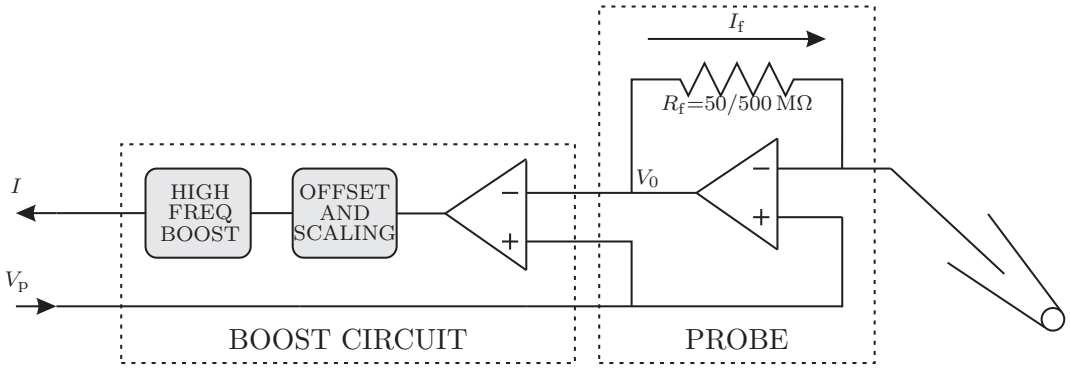

Figure 3.8: Equivalent circuit diagram / Essential working parts of the CV 203BU headstage in resistive operation mode. Feedback resistor R_f, current through feedback resistor I_f, pipette potential V_p *[*Molecular Devices Corp., *1999]*.

is the same as the current through the feedback element R_f (Figure 3.8). Since the operational amplifier in the probe acts to keep the voltage at its two inputs equal to each other, the potential at its negative input equals the pipette potential V_p. Thus, the voltage across R_f is $V_0 - V_p$, which is calculated by the differential amplifier in the probe box. Subsequent amplifiers are used to scale the gain and remove voltage offsets. A fundamental problem of this circuit is that the output bandwidth of the probe is inherently low. To a first approximation, the bandwidth is set by the product of R_f and the stray capacitance across it. To overcome this limitation, the probe output is passed through a high–frequency boost circuit. The gain of this circuit is proportional to the frequency. In resistive feedback mode under optimal conditions the noise values are 0.55 pA rms for $R_f = 500$ MΩ and 1.60 pA rms at $R_f = 50$ MΩ, respectively.

An alternative to measuring current across feedback resistors is to measure current as the rate of change of the voltage across a capacitor (Figure 3.9). Nearly ideal capacitors exist whereas high–gigaohm resistors found in patch clamp headstages possess intrinsic noise (in excess of thermal noise) and have limited bandwidth due to stray capacitance. The benefits of capacitors are taken advantage of in the *PATCH* configuration of the *CV 203BU* headstage, which is designed for low–noise current recording. The headstage measures the integral of the current which is subsequently differentiated to allow measurement of the current itself. The capacitor mode achieves a substantial reduction of noise and has much better linearity compared to resistive feedback headstages. In integrating headstages, the low frequency asymptote of the noise depends on the gate current of the headstage input transistor rather than on the thermal noise of

the feedback resistor [Molecular Devices Corp., *1999*]. The low–noise recording performance of the headstage is further improved by actively cooling down critical parts of its circuitry. For this purpose, a build–in peltier device can be controlled by the main amplifier. There is one disadvantage in capacitive feedback measurement. The voltage

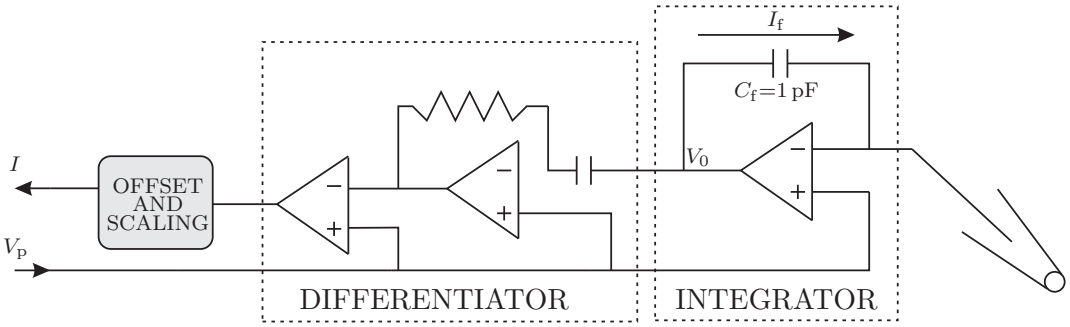

Figure 3.9: Equivalent circuit diagram of the capacitive–feedback configuration. Feedback capacitor C_f [Molecular Devices Corp., *1999*].

across the feedback capacitor cannot ramp in one direction forever. At some point the capacitor voltage will approach the supply limits and the integrator must be reset. Thus, the current record must be interrupted for 50 μs while the integrator and differentiator reset. When this reset occurs, a sample and hold circuit maintains the value of the current at the level it had just prior to the reset. In capacitive feedback mode under optimal conditions the noise values are 0.045 pA rms.[Molecular Devices Corp., *1999*].

Connecting the Reference Ag/AgCl Electrode

After chlorination of the silverchloride reference electrode made for insertion into the pipette, it has to be securely attached to the headstage preamplifier to secure good electrical contact in order to perform reliable measurements. Therefore, the nonchlorided end of the silver wire is inserted through the hole of the silicone seal and bended at the last 1 mm over to an angle of 90° (see figure 3.10). Then the wire is pressed into the back of the barrel making sure that the silicone seal is flush with the back of the barrel. After slipping the threaded collar over the back of the barrel, the pin cap is screwed down firmly with the large end of the pin directed toward the bent–over wire. This procedure assures good electrical contact between the silverchloride electrode and the headstage circuitry.

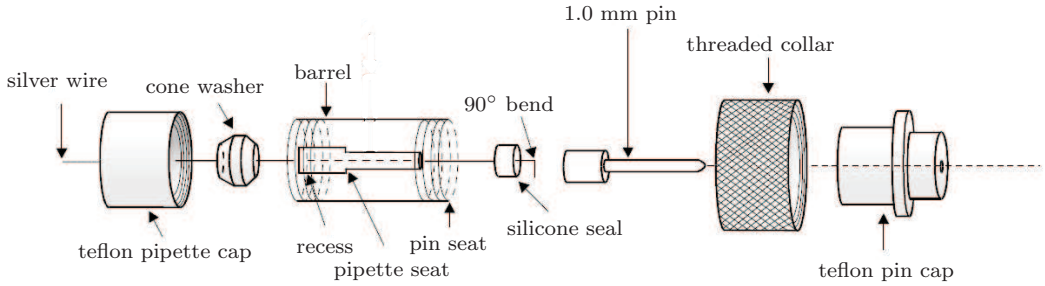

Figure 3.10: Exploded view of the HL-U original pipette holder made of polytetrafluroethylene resin (PTFE) and polycarbonate used as mechanical connection between the silver wire and the headstage. *[*Molecular Devices Corp., *1999]*.

Main Amplifier

In this work, the Axopatch 200B amplifier solely is operated in the voltage–clamping mode, which means that the command potential between the two electrodes is kept constant. So all changes in the conductivity are observed as changes in the current flowing between both silver chloride electrodes. The command potential itself is set via the rear *EXT. COMMAND* input that is in connection with an analog channel of the DAQ device controlled by the SICM software. During all experiments, the peltier–cooling of the headstage circuitry is turned on resulting in temperatures of about $-25°$ C inside of the headstage.

Current and Voltage Conventions

Positive current: The flow of anions *out* of the headstage into the microelectrode and out of the microelectrode tip into the electrolyte reservoir is termed positive current.

Positive voltage: The term *positive voltage* means a positive voltage at the headstage input with respect to ground.

Pipette Offset Compensation

The *PIPETTE OFFSET* control is used to add up to ± 250 mV to the pipette command potential (V_p). In order to compensate for the total offset of the liquid–liquid and liquid–metal junction potentials in the electrode and bath, and the offset of the probe

input amplifier. It is used at the beginning of each experiment to zero the pipette current I when the electrode first touches the solution, and may be used occasionally thereafter to manually adjust for any offset drift.

3.11 Lock–In Amplifier

In order to improve stability and noise of the SICM control signal, a lock–in amplifier (LIA) is used for both, creation of the reference modulating frequency and phase–sensitive detection (see section 2.5 for details). For this purpose, a digital signal processing, two–channel lock–in amplifier (Model SR830, Stanford Research Systems, Sunnyvale CA, USA) is used.

The SR830 offers direct digital reference frequency synthesis with single–frequency sine waves between 1 mHz to 102 kHz and amplitudes ranging from 4 mVrms up to 5 Vrms. This reference signal is directly connected to the MOD input of the piezo–stacks control amplifier to give the reference frequency for phase–sensitive detection onto the ionic current via oscillation of the piezo–stack. After low–noise analysis of the modulated current (see section 3.10), the output signal of the microelectrode amplifier is fed into the signal input A of the lock–in amplifier.

All settings of the LIA are controlled via the SICM software using a GPIB–connection (IEEE-488.2) from the realtime controller. Among others, the most important settings are:

Reference Signal The amplitude and frequency of the reference frequency must be set properly in order to achieve reasonable modulation of the ionic current. According to section 3.9), the dependency between the output signal amplitude V_{MOD} and the resulting oscillation amplitude z_{MOD} of the pipette is given by

$$z_{\mathrm{MOD}}\left(V_{\mathrm{mod}}\right) = \frac{950}{V_{\mathrm{MOD}}}\frac{\mathrm{nm}}{\mathrm{V}}. \tag{3.11.1}$$

From experience, an oscillating amplitude of about 50 nm to 150 nm corresponding to modulating voltage amplitudes of about 50 mV to 160 mV gives good results.

Signal Input Configuration: Configuration of the signal input is made in accordance with the type of input signal. Most commonly, the signal is fed into the LIA as a single–ended DC signal and DC–coupling for the input is chosen. Notch–filtering of line–frequency (50 Hz/60 Hz and 100 Hz/120 Hz) pickup is turned on in order to remove any significant line–disturbances.

Time Constant: Lock–in amplifiers have traditionally set the low pass filter bandwidth by setting the time constant. The time constant is simply $1/2\pi f$ where f is the -3 dB frequency of the filter. The notion of time constant arises from the fact that the actual output is supposed to be a DC signal. In fact, when there is noise at the input, there is noise on the output. By increasing the time constant, the output becomes more steady and easier to measure reliably. The trade off comes when real changes in the input signal take many time constants to be reflected at the output. This is because a single RC filter requires an integration time of about 5 time constants to settle to its final value. The time constant reflects how fast the output responds, and thus the degree of output smoothing. Time–constants can be set in the range from 10 μs to 30 s. Most commonly, a time–constant of 1 ms is chosen.

Sensitivity: The full scale sensitivity of the LIA can be set between 2 nVrms and 1 Vrms in a 1–2–5–10 sequence. A typical value for the sensitivity in a SICM measurement is 20 μVrms.

Filter Slope/Oct: The low–pass filter slope determines the overall–bandwidth of the lock–in detection. Low–pass filter slope can be set as either 6, 12, 18 or 24 dB/oct. A narrower bandwidth will remove noise sources very close to the reference frequency, a wider bandwidth allows these signals to pass.

Output configuration: The X and Y rear panel outputs are the outputs from the two phase sensitive detectors with low pass filtering. These outputs are the traditional outputs of an analog lock-in. The X and Y outputs have an output bandwidth of 100 kHz. The two front panel outputs can be configured to output voltages proportional to the CH1 and CH2 displays or X and Y. If the outputs are set to X or Y, these outputs duplicate the rear panel outputs. If they are set to 'Display', the output is updated at 512 Hz, which is rather slow. The CH1 display can be defined as X, R, X Noise, Aux Input 1 or 2, or any of these quantities divided by Aux Input 1 or 2. The CH2 display can be defined as Y, Θ, Y Noise, Aux Input 3 or 4, or any of these quantities divided by Aux Input 3 or 4. If a display is defined as simply X or Y, this display, when output through the CH1 or CH2 output BNC, will only update at 512 Hz. It is better in this case to set output to X or Y directly, rather than the display.

According to equation 2.5.4, the signal output X and Y of the two channels / two phase–sensitive detectors, can be summarized to result in the overall signal amplitude $R = \sqrt{X^2 + Y^2}$. Both channels outputs are being output from the front connectors 'CH1 OUTPUT' and 'CH2 OUTPUT', respectively, which are configured to output X

and Y. Its magnitude is proportional to the amplitude of the modulation of the ionic current at the reference frequency. Furthermore, that signal is independent of any phase–shifts between the reference and the signal. This signal R is the SICM–control signal used as the input for the distance–control algorithm. It is strongly depending on the distance between the probe tip and the scanned surface.

3.12 Microscope Control Hardware

The hardware concerned with the control of the SICM consists mainly of two parts. The first one is the host computer HPC, a notebook personal computer for controlling all microscope parameters and settings, monitoring the scanning process, receiving scanning data and analyzing topographical information for image generation.

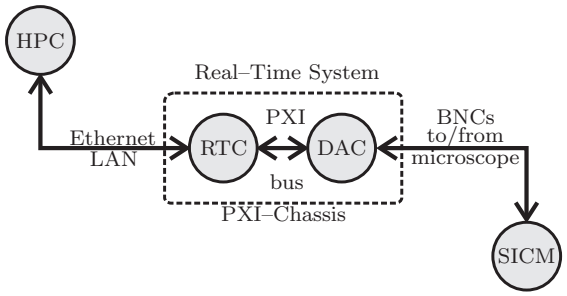

Figure 3.11: Control hardware diagram. The host computer HPC connected over a fast network link is steering the real–time system. This system consists of a PXI–chassis into which are inserted a real–time controller RTC and an analog/digital converter card DAC. Fast data transfer between RTC and DAC is realized using the PXI bus system. The I/O channels of the DAC are connected to the sensors and actuators of the SICM.

The second part is a real–time system that is realizing the scan (figure 3.12). Implemented on this system there is the feedback control that periodically corrects for

Figure 3.12: Image of the National Instruments PXI–1031 PXI chassis with a PXI real–time controller and further PXI devices inserted. This device is used for execution of time–critical microscope control tasks.

the tip–sample distance and the scanning routines for lateral movement of the sample scanning piezo stage. The real–time system is connected to the HPC over an 1 Gbit/s local–area ethernet connection. This system consists of a chassis (PXI–1031, National Instruments Corporation, Austin TX, USA) with a 4–slot PXI 3U backplane. Installed into this chassis there is an embedded high-performance PXI–compatible system real–time controller (NI PXI–8186, National Instruments), which is equipped with a 2.2 GHz Intel Pentium 4 Mobile CPU, 1 GB of RAM and a 30 GB hard drive. This embedded controller has specialized hardware for facilitating real–time deterministic performance, since it uses sophisticated caching techniques and contains special timing and triggering hardware. For high–speed data I/O to and from the embedded controller, a multifunctional DAQ (data acquisition) device (NI PXI-6259, National Instruments) is connected to it over the chassis–intrinsic PXI backplane. This device has four 16–bit resolution analog output channels with a maximum output rate of 2.8 MS/s and 32 analog input channels with 1 MS/s maximum input rate. For real–time purposes, the I/O of this device can be coupled chronologically to an internal digital hardware clock that is used for triggering both the input and the output operations. Due to the 16 bit resolution of the AD– and DA–converters, the PXI–6259 can both output and input 2^{16} different values. Since the input and output ranges (the difference between maximum and minimum I/O voltages at the DAC–channels) are 20 V (-10 V to +10 V), the minimum voltage–step that can be written at the output or resolved at the input is

$$\frac{20\ \mathrm{V}}{2^{16}} = 305\ \mu\mathrm{V}. \tag{3.12.1}$$

Sixteen–bit DAC resolution is needed, since 12bit resolution (which is the next lower resolution possible) leads to 16–fold ($2^{16} - 2^{12}$) larger minimum voltage steps of 4.88 mV magnitude, as can be seen in figure 3.13. Here, a voltage ramp is applied to the channel of a 12bit DAC and a 16bit DAC, respectively, that are connected to the control input of the piezo–stage. The 4.88 mV steps are clearly visible in the monitor channel of the stage and would lead to a limitation of the physical resolution of the piezo flexure stage. Applying 12 bit resolution control to the P–517 piezo scanner would lead to minimum scanning steps of 9.76 nm in vertical direction ($2 \cdot 10^4$ nm$/2^{11}$) and 48.83 nm in lateral direction (10^5 nm$/2^{11}$). This rough resolution is expected not to be sufficient for analyzing SICM scan resolution limits, that should be in the range of the scanning probe diameter. Therefore, 16–bit DAC resolution is used for control of the SICM.

For facilitating physical access between the DAQ channels and the sensors and actuators of the microscopy (by means of BNC connectors), all analog channels of the

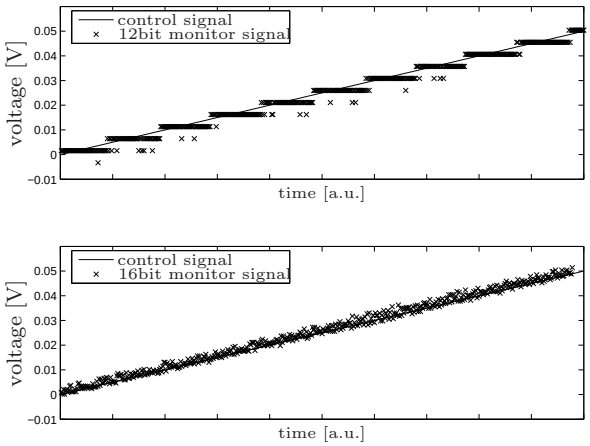

Figure 3.13: Influence of DAC resolution on the minimum physical step size of the piezo scanner. Upper: Voltage ramp applied to the 12bit DA–converter connected to the control of the stage. Resolution limitation of 4.88 mV (9.76 nm minimum vertical step size) shows up in the monitor signal. Lower: The same experiment using a 16bit DAC converter. The resolution is 16 times higher (305 μV, 0.61 nm minimum vertical step size).

DAQ device are connected to a rack–mount analog breakout accessory (BNC–2090, National Instruments Corp., USA). To minimize noise–pickup and crosstalk, the connecting cable features individually shielded analog twisted pairs (NI SHC68–68–EPM, National Instruments Corp., USA). All analog channels of the NI–PXI 6259 can be set up individually concerning input/output voltage range, and channel configuration. The channel configuration can be either differential (DIFF), non–referenced single–ended (NRSE) or referenced single–ended (RSE). However, single–ended systems are susceptible to ground loops. But since due to hardware limitations, differential mode is not realized in the presented SICM and the RSE mode is not recommended to be used by the manufacturer of the hardware *[*National Instruments Corporation, *1996]*. For SICM, all channels are working in NRSE–mode. In a non–referenced single–ended system, all the channels are still referenced to a common point. But the common channel in this case is not connected to system ground.

3.13 Microscope Software Development Environment

During SICM operation, the scanning system hardware is under control of the SICM software. This software is implemented in LabVIEW (National Instruments Corp., USA). LabVIEW, short for **Lab**oratory **V**irtual **I**nstrumentation **E**ngineering **W**orkbench is a development environment for a visual programming language named 'G' from National Instruments Corporation, USA. Programs implemented with LabVIEW are called VIs (Virtual Instruments). LabVIEW is appropriate to be used for SICM software implementation, because it can be used simultaneously for both crucial tasks of SICM, for data acquisition and instrument control. Furthermore LabVIEW offers ex-

tended capabilities for design of deterministic real–time applications and it is possible to create distributed applications which communicate by a client/server scheme. The latter functionalities are required for the successful implementation of a high–speed feedback control system.

For the development of the microscope software, LabVIEW version 8.20 and several of its specialized subcomponents are used. Installed on the host computer, the LabVIEW development system executes locally implemented VIs. This execution is based on the general–purpose operating system Microsoft Windows XP (compare with figure 3.14).

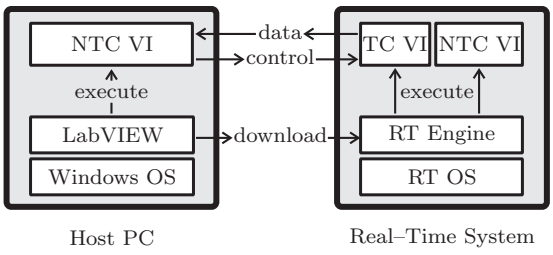

Figure 3.14: Distributed SICM control software layer interaction. LabVIEW downloads VIs to the real–time system and executes non time–critical VIs (NTC VI) that run locally on the HPC. Remotely, the RT engine executes both, non time–critical VIs and time–critical VIs (TC VI). The NTC VIs are responsible for communication and data transfer mainly.

The Real–Time Module 8.2 extends the capabilities of LabVIEW to allow for selection of a remote real–time controller on which to run time–critical VIs. The RT Engine is a version of LabVIEW that runs on RT controllers. It provides deterministic real-time performance for the following reasons. First, the RT Engine runs on a real-time operating system (RTOS), which ensures that the LabVIEW execution system and other services adhere to real-time operation. Second, the RT Engine runs on RT Series hardware. Other applications or device drivers commonly found on the host computer do not run on RT targets. The absence of additional applications or devices means that a third-party application or driver does not impede the execution of VIs. Lastly, RT targets on which the RT Engine runs do not use virtual memory, which eliminates a major source of unpredictability in deterministic systems. For keeping real–time capability of the system, all parts of the participating software on the real–time system have to be designed specifically to meet corresponding requirements. So, the communication between the distributed software components on the RTC and the HPC as well as the communication over the GPIB interface are facilitated by specialized drivers. National Instruments DAQmx 8.3 is used as the driver for controlling the DAQ device. NI-DAQmx offers a variety of VIs specifically designed for the data acquisition

device. Among these are device–configuration VIs and real–time triggering of analog I/O operations.

3.14 Image Analysis Software

Analysis of the scan data and visualization of the topographical image is done using Matlab (The MathWorks Inc., Natick MA, USA). The source data is encoded in a binary file using big Endian byte ordering and consists of a two–dimensional matrix with 12 columns. Details like the scan area size and the pixel numbers are read from the header file. Based on this information, the topographical data is illustrated by analysis of the pixel number column. Pixel changes are detected by changes of the value in this row and a predefined number of rows prior to this change is used for pixel data evaluation. According to the piezo–stages Z channel monitor signal, the spatial information of these rows is averaged and fed into the image matrix. This matrix is displayed as an intensity bit–mapped image. Because the piezo–stage scans a negative image of the surface, the image matrix is by default additively inverted. Naturally, in most cases the spatial information of the sample is used for construction of the image matrix to display the topographical information as a function $z = z(x, y)$. Besides that, it is possible to visualize other scan quantities like the control error e ($e = e(x, y)$) or the pixel–control time Δt ($\Delta t = \Delta t(x, y)$) (the time the probe was localized above one lateral coordinate) or others. This is useful for detailed scan analysis and debugging purposes.

Furthermore, it is possible to visualize the scanned surface by a three dimensional shaded surface plot. For doing so, the bitmap matrix is interpreted by a smoothing two–dimensional fitting algorithm ('gridfit'). It builds a surface over the complete bitmap lattice and extrapolates smoothly onto the edges. The user has control of the amount of smoothing, as well as interpolation methods. Therefore, this method must not be understood as an exact representation of the measured spatial information but as a guide for the eyes for better understanding the geometry of the scanned surface.

Image correction

In almost any case, the plane carrying the scanned sample can not be mounted perfectly complanar to the scan plane of the piezoscanner. This leads to a tilted scan area. Even

if the tilting angle is very small it leads to a significant decrease of the image contrast. For instance, a scan of 10×10 μm tilted by an angle of only 0.01 rad (0.57 degrees) will cause an additional difference between the maximum and the minimum of z of 100 nm.

Furthermore, any fluctuations of the LIA response will be compensated by the feedback control distance correction, independent from the source of the fluctuation. Components of the fluctuations with time–constants that are much shorter than the scan pixel time will simply lead to noise in the image information. Long termed fluctuations (drift) in the LIA response with time constants in the range of row–scan times (seconds to minutes) lead to the build–up of a gradient structure reducing the image's contrast (see figure 3.15). In many cases the errors caused by a tilted scanning plane and/or

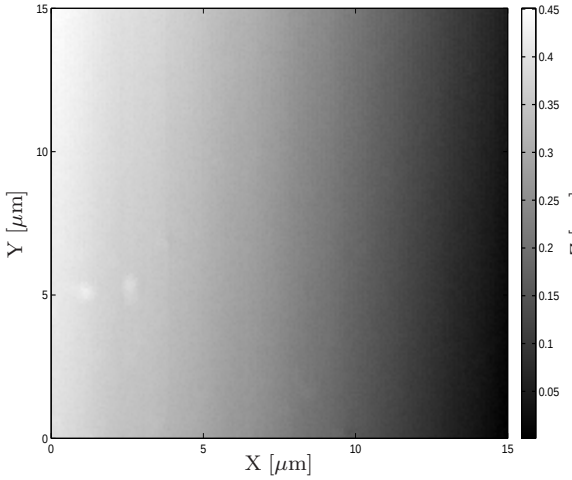

Figure 3.15: Uncorrected original SICM scan data. The image contrast is small due to slow vertical relaxation of the scanning probe.

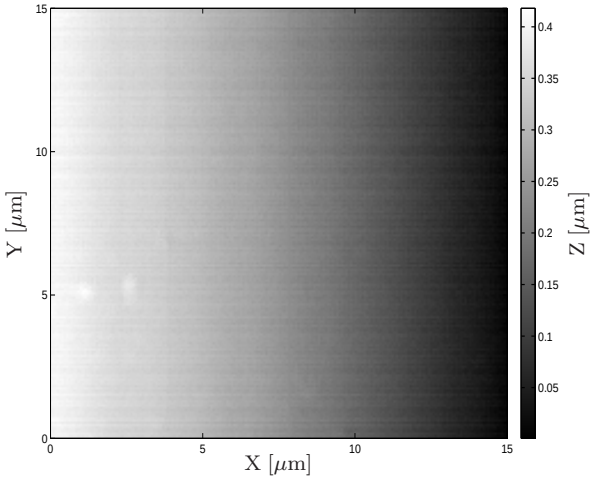

Figure 3.16: The same image with error correction in the Y–direction. Column 105 is subtracted from the 199 other image columns.

slow fluctuations, can be corrected out of the images by a simple procedure. It implies the assumption that the image is disturbed by a fluctuation slow enough so that the wave structure is only depending on one image dimension. If this is true, information about the error can be found in one single row or column. By subtracting this information from every row of the image matrix, the error can be corrected (figure 3.16). If necessary, this method can be applied also to the perpendicular image dimension. (see figure 3.17). Figure 3.18 shows the original image corrected for slow errors and tilted scanning–plane in both image directions. Obviously, the procedure enhances the image–contrast but introduces additional (but small) error. This new error is due to the additive smearing of the noise of one single row/column over the whole image

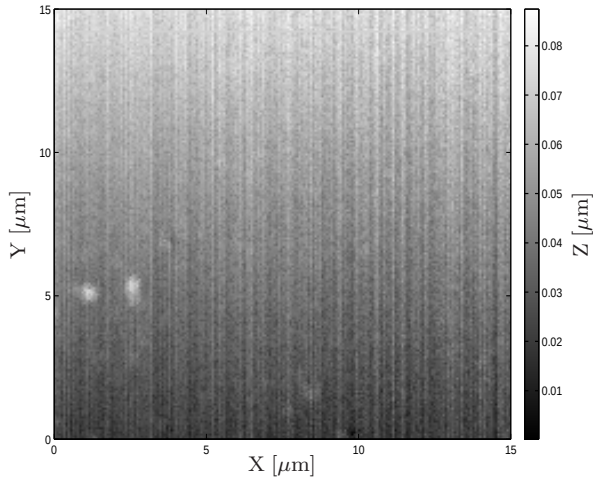

Figure 3.17: The same image with error correction applied for the X–direction. Row 190 is subtracted from the 199 other image rows.

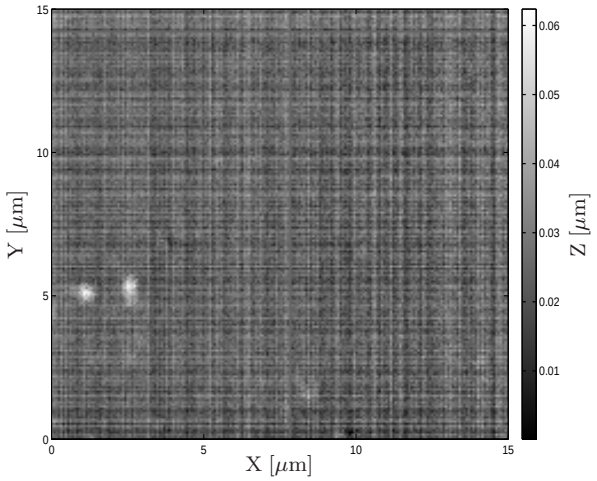

Figure 3.18: Simultaneous application of the above correction procedures. The image contrast is significantly enhanced.

matrix.

3.15 Sample Preparation

The scanned surfaces are in most cases prepared in Lab–Tek Chamber Slide Systems (Nunc A/S, Roskilde, Denmark) with eight wells. Lab–Tek Chamber Slides consist of a standard coverslip glass (d=0.13 mm), onto which a polystyrene grid is glued forming eight wells of equal volume. Each well surrounds an area of 0.8 cm^2 and a working volume of 1 cm^3. These wells are very appropriate for making SICM measurements since their dimension limits the horizontal spreading of the electrolytic solution and constrains evaporation. On the other hand it offers enough space for safe insertion of the scanning probe as well as the reference electrode.

3.16 Operating the Microscope

At this point a short description of a typical procedure for operating the SICM is presented.

The initial step is to start the SICM application. First, the software–component running on the RTC is downloaded and executed. Afterwards the control–component running on the Host PC is executed. During successful initialization of the hardware

and software the piezo scanning stage is lowered allowing for continuation of the SICM preparation. After successful preparation of the sample it must be manually positioned on the scanning stage above the microscope objective with the region of interest right above the center of the objective. After that the sample is immersed with electrolytic solution appropriate to the experiment. Using the SICM starts with preparation of the electrodes. It must be ensured, that both electrodes are dry, clean and chlorinated well. The reference electrode, whose silver wired end is clamped into a plug, is positioned such that the silverchloride pellet is bathed into the solution without getting into physical contact with either the probe or the sample or the support surface. After the scanning probe is pulled, it is filled with the same solution the sample is immersed in (see section 3.4). Then it is put into the cavity of the pipette holder and all six screws of the holder are tightened gently to secure clamping of the pipette. If the support of the holder/piezo–combination is located straight above the sample, the piezo stack is carefully positioned under the aluminum cantilever before it is tightly secured by turning the screw. At this point it is crucial to prevent the probes tip from getting into contact with any matter other than the solution the sample is immersed in. After securing the SICM probe on the Al–cantilever, the internal silverchloride electrode is put into the pipette. To do so the electrode is first contacted to the preamplifier by screwing the polycarbonate–holder into it. After that, the headstage is moved towards the SICM probe and carefully inserted into the back–opening of the pipette. To avoid damaging of the electrode, it is important not to bend the wire and to prevent extensive scratching of the electrode tip on the probe holder's surface. If not already done, the pipette tip should now be lowered until it is in contact with the solution. So a quick check of the pipettes resistance can be performed guaranteeing that the glass has not been damaged during mounting of the probe. In most cases, the electrodes potential relaxes during approximately the first 30 minutes after being immersed. This process can be monitored over the displays provided by the SICM control application. During relaxation of the electrodes potential no external voltage should be applied. After the electrodes have reached their equilibrium state, the remaining offset potential should be compensated using the 'Pipette Offset' potentiometer located at the control panel of the MEA.

Prior to starting the SICM scan, the oscillating pipette tip must be placed at the initial scan position. This is done in two steps. First, the probe is manually positioned by means of the micropositioning system (see section 3.7). During this process, the pipette is illuminated by the microscope halogen lamp from the back so that its shadow can be

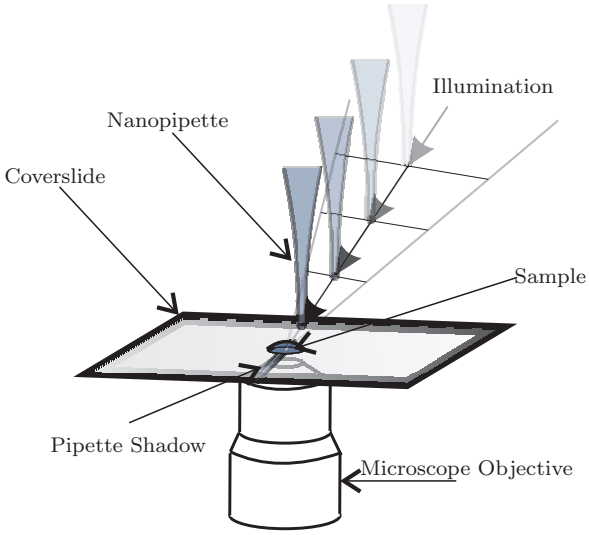

Figure 3.19: Optically controlled manual tip approach procedure. The probes tip is positioned manually until it is in the range of the computer–controlled piezo stage. This is done indirectly by controlling the pipettes shadow through the ocular of the optical microscope.

optically controlled through the microscope optics. Due to the limited resolution of the mechanical positioning system, both the lateral and vertical position can be adjusted with a precision of about one micrometer. Additionally, the optical recognition of the pipettes position by its shadow induces a large error in the lateral control precision. Manual approach of the pipette is stopped at a distance of 10 μm. Here, the pipette tip is within the range of the scanning piezo stage. Not later than now the electromagnetic shielding cage must be positioned and the plexiglass surrounding of the setup has to be closed. Further minimization of current noise can be achieved by turning off the IX70 inverted microscope as well as the lab light. Further approach is now done by

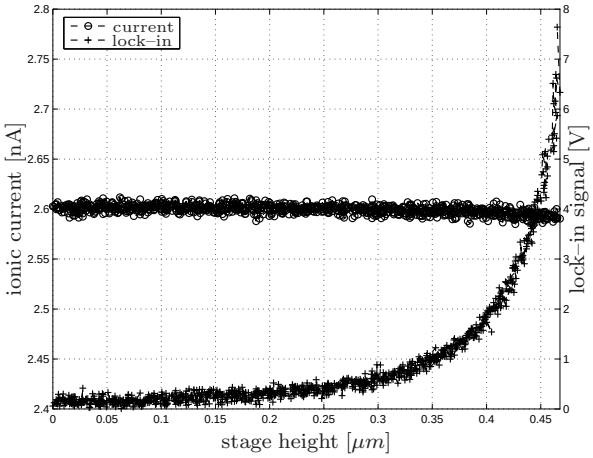

Figure 3.20: Ionic current and lock–in response monitored while tip–sample distance on a oil/water interface is decreased stepwise. It can clearly be seen that both the signal to noise ratio and the sensitivity in lock–in detection is much larger than in the ionic current signal itself.

computer–controlled raising of the stage. With successive vertical steps of adjustable size and rate, the tip–sample distance is reduced. Commonly, the step size is 5 nm at a

speed of 400 nm/s. The tip–sample distance is evaluated by monitoring the derivative dR/dz of the LIA output R. If this derivative is exceeding a predefined threshold, the control signal is obtained and the approach of the piezo stage is aborted by simply holding the command input voltage. In the case of reaching the stages maximum travel without obtaining the control signal, the stage is moved down into its initial position. Then the micropositioning system is used to move down the probe by an appropriate distance (most commonly about 10 μm) and the approach can be reinitialized.

4 Experimental Results and Discussion

4.1 SICM Development

4.1.1 Software Development

Successful operation of a SICM requires concerted manipulation of the various hardware components. In seldom cases this might be done manually, for instance when the probe or the sample have to be changed. Most of the operations on the hardware must be executed using a computer system. These operations are exercised by SICM software which is specially developed for integrating all hardware components. As explained in section 3.13, the software is a distributed system running simultaneously on two execution targets connected over a local network. One of these targets, named real–time target or real–time system, is employed by software components responsible for fast and undisturbed deterministic control of the distance control mechanisms and lateral scan procedure. The other one, named the host–PC, is concerned with making appropriate settings, manage data transfer and performing the image analysis and construction. The combination of both software components is bundled in a LabVIEW project, which logically bunches LabVIEW programs (VIs) together with their variables and configurations.

The software component running on the host PC is realized as a finite state machine with five states (figure 4.1). The different cases are named the initialization state INI, the configuration state CONF, the approach state APP, the scanning state SCAN. Finally, there is a shutdown case STOP.

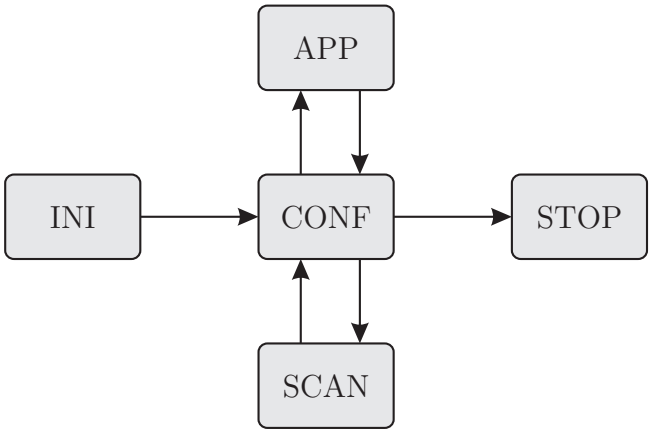

Figure 4.1: State–flow diagram of the SICM software running on the host PC. After state INI has finished (hardware– and software initialization), the default mode configuration CONF is entered. From here, the two states APP for probe–sample approaching and SCAN for scanning setup and initialization can be entered.

The primary state is the initialization state INI, after whose completion the system enters the default state CONF. From here the configuration of the system and software settings can be managed. Entering the state APP from here manages the tip–sample approach and switches back to CONF afterwards. The state SCAN handles the scanning, monitoring and initialization. The STOP state initializes a shutdown sequence of the SICM software.

At startup, the system enters the INI state. Here, the network connection to the real–time target RTT is checked and variables are initialized. Transportation of parameters and settings between the HPC and the RTT is managed by network–published shared variables. These variables are visible inside the distributed software, which means that their values can both be written and read from the HPC and from the RTT, although only one instance of each shared variable is defined. The LabVIEW Shared Variable Engine takes care about access management and value propagation of the shared variables. This data transfer mechanism is applicable only for simple elementary data types and moderate transfer rates.

The subsequently following CONF state is the default state of the software. Here, all SICM settings are made by updating the values of the shared variables which are containing all microscope settings. The CONF states includes a data acquisition (DAQ) category, a microelectrode amplifier category (MEA) category, a lock–in (LIA) category and an image parameter setting (IMAGE) category. Furthermore, sensors of the microelectrode amplifier and the lock–in amplifier are monitored and displayed continuously. The data acquisition category DAQ stores controls for the analog input and output channels. The terminal configuration can be switched between RSE, NRSE and DIFF

according to the connected hardware. Furthermore, the I/O voltage range is defined here between 0 V and 10 V. All settings for the adjustment of the image scanning area are bunched in the category IMAGE. Figure 4.2 illustrates the parameters function. The scanned area is a rectangle spanned by an initial position coordinate (Ix, Iy) and

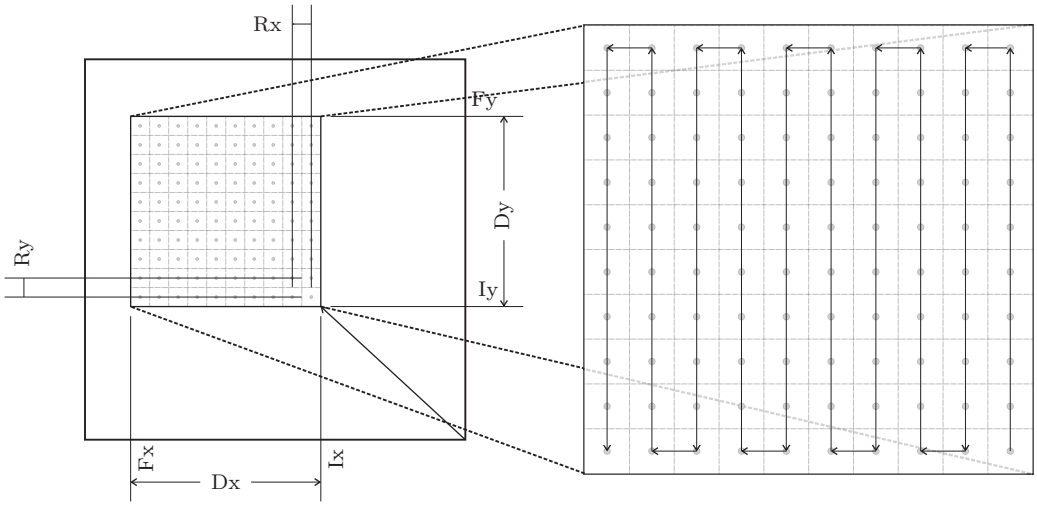

Figure 4.2: Left: Scanning area and scan resolution. Within the scanning stages range of $100 \times 100\ \mu\mathrm{m}^2$ (outer square), the rectangular scanning area can be defined over the initial probe position (Ix, Iy) and final position (Fx, Fy). The pixel (dots) resolution Rx, Ry is the ratio of lateral scan range dimension and the pixel counts n, m (here: (10,10)). Right: Path of the scanning probe in relation to the scanned area. The pattern is a line scan with alternating scan direction. Consecutive analysis of each pixel is performed.

a final position (Fx, Fy). The resulting area of size $Dx \times Dy$ is divided into $n \times m$ rectangles, resulting in pixel–resolutions of $Rx = Dx/n$ and $Ry = Dy/m$. The center of each sub–rectangle defines a location at which the tip–sample distance is evaluated. So n and m represent the pixel numbers of the scan in X and Y direction, respectively. All values Ix, Iy and Fx, Fy, are limited by the lower and upper range boundaries of the scanning piezo stage (commonly 0 μm to 100 μm).

In the category for configuring the microelectrode amplifier, all settings that are concerned with the measurement of the ionic current are placed. Here, the potential difference between the two silverchloride electrodes is set in a range between -200 mV and 200 mV. By continuous monitoring of the current, the corresponding (pipette–) resistance is indicated to give a rough estimation of the pipette aperture size. Information about the configuration of the microelectrode amplifier is provided by indicators

that show the setting of the lowpass Bessel filter frequency, the gain and the devices operation mode. In the LIA category, the lock–in amplifier is configured by controlling of the reference modulation frequency and amplitude, the sensitivity and the integrating time–constant. Filtering of the LIA input can be changed by adapting the lowpass–filter slope and the sync filter status. Automatic adjustment of the sensitivity, the dynamic reserve and the phase of the input signal can be made here.

The most crucial part of the software is the feedback control loop. All modifications of its settings can be made in the Control category. Besides the PID gains, the output range limits of the PID can be managed here as well as the feedback loop frequency and some more complex settings.

Entering APP state allows for calibration and initialization of the tip–sample approach algorithms. Basically, the stage is raised by linearly stepwise increasing the voltage at the appropriate piezo–stage input channel (corresponding to an analog output channel of the DAQ device) until the control signal has reached a predefined threshold. The control signal used is the derivative dR/dz of the LIA signal R, since this magnitude is independent of possible offsets of R. Furthermore, dR/dz is the magnitude the feedback control applies when controlling the tip–sample distance, therefore making an approach onto equal values of dR/dz makes comparable environments for different tip–sample approaches or different nanopipettes. Settings that can be made for adjustment of the approach algorithms are as follows. The lower and the upper limits of the raising of the stage can be set between 0 μm and 20 μm (default is starting from 0 μm and raising to 20 μm). The speed the stage is lifted with can be given in nm/s with a default of 400 nm/s. In most cases a vertical step size of 10 nm is chosen. All critical values (lock–in output, derivative of lock–in output, ionic current and the threshold) are shown in real–time on a display–graph. If the tip–sample distance is small enough (i.e. the sample is approached and the threshold of dR/dz is reached), the algorithm stops increasing the output voltage at the piezo–stage input. If the upper limit of the lifting is reached, the stage is lowered until the given lower limit is reached and a new approach can be started after manually lowering the pipette holder (by approximately half the lifting range). Optionally, during lifting the stage all crucial parameters can be stored in an ASCII–format. If needed for correction, the stage height can stepwise be adjusted after approaching by using software control buttons. Steps up and down of adjustable size (5 nm default) can be made.

The SCAN state is for initialization and monitoring of the scanning process. As long

as the scan is not initialized, the setpoint (reference value of the feedback control algorithm) can be set. Either manual setpoint selection is made or the setpoint is defined automatically as the value of the lock–in amplifier output at the start of the scan. Also the boolean VERBOSITY can be switched. If VERBOSITY is true, for detailed system analysis and debugging purposes all data generated in each feedback control loop iteration is transferred from the real–time target to the host PC and stored in the data file. If VERBOSITY is set to false, only the data produced by the latest n control loop iterations (before regarding distance control at the actual pixel to be steady) are transferred and stored. This is the default value. The count n can be set, in order to calculate the average and thus reduce noise. Also, this function is for speed, file size and overall performance optimization. Initializing the scan induces a sequence of actions. First, the VIs running on the real–time target are occasioned to switch into the EXEC/SCAN mode (see section 4.1.1). A new TCP connection is opened between the host PC and the RTT to receive image data and to make it possible to control the scan in process. After that, a while–loop is entered in which data is read from the TCP connection and stored in a binary file stream in big Endian byte order, which means that the most-significant byte occupies the lowest memory address. This loop iterates without any artificial delay implemented to follow up the data generation of the feedback loop, which in most cases iterates faster than the receiving loop on the HPC can do. The data generated by the feedback loop consists of rows of 12 doubles with 64 Bit of precision. Three of them, namely the monitor signals of the piezo–stage contain the spatial information of the scanned topography. The software interprets this information by feeding it to an intensity graph, giving the ability to make a runtime estimation of the scanned topography. The SICM data file is named 'SICMscan *YYYYMMDD-HHmmSS*.sicm', where *YYYYMMDD* stands for the scan date and *HHmmSS* for the time of the starting of the scan. In addition to the data file, a ASCII header file containing important measurement information is generated named 'SICMscan *YYYYMMDD-HHmmSS*.hdr'.

The software running on the real–time target is implemented as a finite state machine with four states (see figure 4.3). These cases are the initialization state INI, the waiting state WAIT, an execution state EXEC and the shutdown state STOP. The first state entered after starting the software is the INI state, in which the hardware, i.e. the DAQ device and the software (shared variables) are initialized. Afterwards, the WAIT state is entered. In the WAIT state, the shared variables containing the actual current flowing through the probe tip, the lock–in signals and the monitoring signals of the

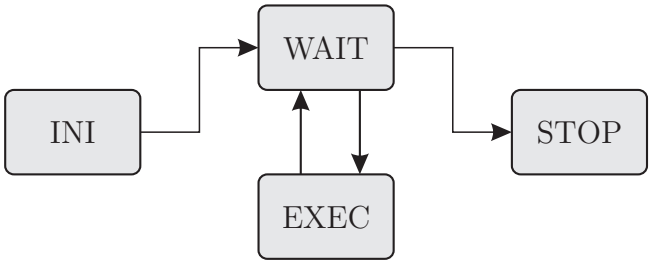

Figure 4.3: State–flow diagram of the SICM software running on the real–time controller. After state INI has finished (hardware– and software initialization), the default mode configuration WAIT is entered. From here, the system can enter the execution state EXEC.

stage channels are updated repeatedly. These variables are continuously monitored by the HPC software to provide information about the system state. Also, the piezo stage position is continuously adapted to the control values that are given by sharde variables. This gives ability of controlling the stage travel by simply changing the values of the a shared variable remotely from the host computer. So in the WAIT state, the DAQ device is utilized with slowly continuous analog input and output operations for monitoring and controlling hardware. Switching from the WAIT into the EXEC state is done by changing a string shared variable. At the beginning of the EXEC state this string is evaluated and according to its value different actions, like changing settings of the lock–in amplifier or starting the scanning procedure, can be released. Altering the LIA settings is done by VIs transmitting GPIB commands to the LIA.

Initializing the scan releases a sequence of actions starting with the allocation of the DAQ device. Here, the slow input output operations are aborted to give access to the full performance of the DAQ board. After a new TCP/IP connection has been opened by the HPC, a matrix of $n \times m$ voltage values corresponding to the $n \times m$ image–pixels is calculated to provide voltage–output coordinates for lateral positioning of the stage. Subsequently, the analog input and output operations for the high–speed deterministic feedback control are being armed.

Deterministic Control

Until allocation of the DAQ device, the software system implementation is done in a traditional way, meaning that no special efforts are made for minimization of jitter and realizing deterministic performance. Although the implemented software operates on real–time hardware, there is no real–time functionality involved.

Starting with the configuration of the DAQ input and output configurations, all soft-

ware functions are strictly implemented for maximizing real–time performance and speed. The feedback control algorithm consists of two timed loops. Timed loops are specialized software timing structures provided by the LabVIEW Real–Time Module. By using these loops it is possible to explicitly specify periods for sequential execution and to precisely monitor the successful timing of each iteration. Even more important, the execution of timed loops can be ordered by levels of execution priority. So one loop with high execution priority can inhibit the execution of all timed loops with lower priority if needed to realize a desired period.

In the SICM software, the higher priority (time–critical) loop is concerned with the feedback–control algorithms and with analog input and output controlling the scan. It is timed directly by the hardware sample clock of the analog input device (see figure 4.4). This guarantees exact synchronization of the analog and digital operations on the DAC card and the distance correction operations in the time–critical loop. The input sample clock triggers the analog input operation as well as the analog output operation. While the I/O operations are carried out, the time–critical loop is waiting (idle). After finishing the input operation, the time–critical feedback loop executes processing the main tasks, which are:

Analog Input Data Read: The environment is monitored by reading the analog input data of the lock–in amplifier signal, the magnitude of the ionic current and the position of the piezo stage.

Distance Correction Calculation and Evaluation of Steadiness: The lock–in signal is fed into the PID control algorithm and compared to the reference value corresponding to a defined tip–sample distance. The output is calculated using equation 2.7.7. At each pixel of the image matrix the feedback control corrects the tip–sample distance until the control is evaluated to be steady. The system regards the control to be in steady–state if two conditions are simultaneously true: First, the magnitude of the control error (i.e. the difference between the reference value and the actual lock–in signal) must not exceed a predefined limit. Second, the number of changes of the sign of the error must have exceeded a predefined threshold. This secures for simultaneous stable and fast topological analysis. On smooth surfaces, the scan requires less feedback–corrections so that the noise induces fast changes of the sign of the error. The scan becomes fast. When scanning more complex topography, the feedback control responds with larger corrections on the stages Z–channel control. Only if the control gets stable, the number of sign–changes is reached and the scan necessarily gets

slower. In seldom cases of detuned PID control, the feedback can get into steady–state oscillations which can cause reaching the desired number of sign–changes. But since the evaluation of the steadiness of a pixel in addition depends on the magnitude of the error (that is larger than the predefined limit if the control oscillates), this case does not lead to a successful steadiness evaluation of the actual pixel.

Analog Output Data Write: After the calculation of the step size for tip–sample distance correction is finished, all three values defining the samples position relative to the tip are written to the analog output operation channels. There are two situations in which the time–critical loop is idle. First, while it waits for data from analog input conversion and second after the loop execution has finished. Here, the timed loop waits for the next sample of the clock. During this idle time the non time–critical loop with lower priority receives processor time allowing it to iterate. This communicating loop is mainly concerned with transferring the scan data to the host computer.

In each loop iteration, an array of 12 numbers (each of 64–bit floating point precision) representing the actual SICM system state is generated. This vector is referred to as the scan data. It consists of the actual time (with microsecond precision), and the number of the actual controlled pixel (running from pixel number in X–direction times the pixel number in Y–direction). Furthermore, 6 numbers are generated for the desired and monitored sample position (X,Y,Z analog out and X,Y,Z analog in). The last 4 numbers are the feedback control signal generated by the lock–in amplifier, the ionic current, the control algorithm output and normalized PID gain. Altogether, one scan data array has a size of 96 Byte so that depending on the feedback loop frequency the scan induces a data flow of about 100 kB/kHz (feedback loop frequency) in the verbose mode. In non–verbose mode, only the data generated by the last n control loop iterations of each pixel is stored. Assuming n to be 5 (which is a common value), the data size resulting is 7.5 MB for a 128×128 pixel image. Although the time needed for one scan strongly depends on the topography scanned, a typical duration for a scan of the above dimension is 6 minutes. When scanning at 7 kHz feedback loop frequency, the size of the data generated is about 29 MB (96 bit/iteration $\times$ $2.52 \cdot 10^6$ iterations). This is a representative value for the data size that is generated and transferred in verbose mode. The non–verbose mode, which is the default, typically reduces the data size by 50% to 95% depending on the complexity of the topography and the resulting scan duration.

For guaranteeing the fast and deterministic performance of the feedback loop, the

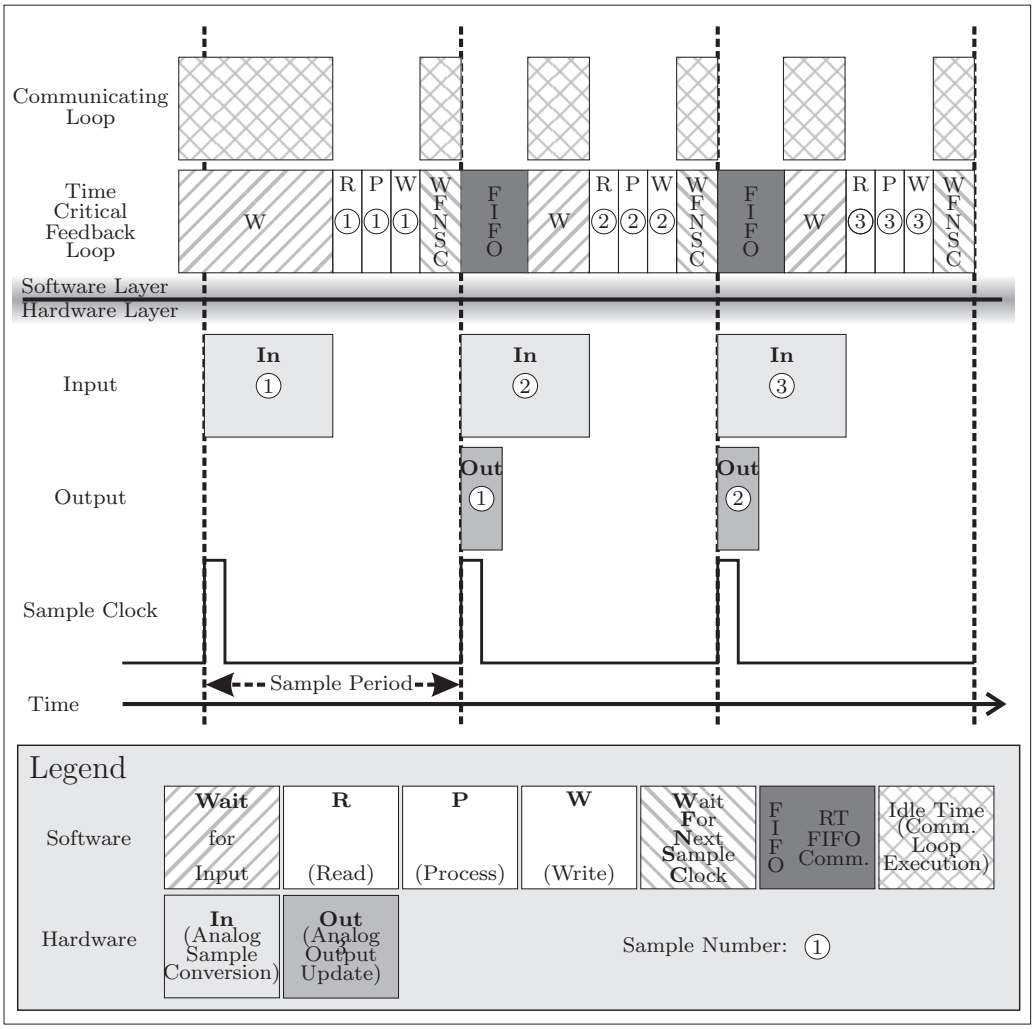

Figure 4.4: Timing scheme of the scanning software timed–loops. The sample clock of the analog input device triggers the time–critical feedback loop. In each iteration, data is read from analog input channels, processed by the feedback PID algorithm and written by an analog output update. Only while this loop is idle, the lower–priority communication loop is allowed to execute for transferring scan data to the host computer.

generated scan data must be buffered. In this particular case traditional global variables cannot be used for buffering. Since only one VI can access a global variable at a time, it can cause priority inversions, which in turn causes jitter, or increases execution time in the time critical loop. Therefore, after being generated, the data is written into a Real–Time First In First Out (RT FIFO), from which it is read by the low–priority communication loop. The RT FIFO is a specialized data type allowing that a write and a read can be performed at the same time. Also, the RT FIFO acts like a fixed size

queue, so that data elements that you write to it do not overwrite previous elements, unless the RT FIFO is full, in which case the oldest element is overwritten. A further advantage of using the RT FIFO is that even if the reader pauses momentarily and multiple writes occur during that time, data is not lost as long as the reader can catch up and read the elements out of the RT FIFO before it fills up. The RT FIFO is of fixed length, and its memory is allocated when the RT FIFO is created before scanning starts. If the RT FIFO was of unlimited length, then it would have to dynamically allocate more memory as the number of elements in the RT FIFO increased. Determinism, or real-time behavior, of time critical VIs would be harmed if this dynamic memory allocation occurred inside of the time critical VI.

The second timed loop ('low–priority loop' or 'non–time–critical loop' or 'communicating loop') executes in parallel to the time–critical feedback loop. It is concerned with reading the scan data from the RT FIFO and transferring it via the Ethernet connection to the host PC application. Because of its lower priority , this loop executes only when the higher priority feedback loop is idle (see figure 4.4). This can be the case if either the feedback loop waits for data from the analog input device operation before doing the feedback control itself or if waits for the next sample of the clock after the control process is finished.

For understanding the complex timing behavior of this two–loop–priority system, one has to keep in mind that the action of the communicating loop is inhibited instantaneously (i.e. without waiting for finishing the actual iteration) when the control loop needs to execute. Nevertheless, missed periods of the low–priority loop are not discarded but restarted later. By doing this it is guaranteed that the data transfer process is consistent, i.e. that there is no data loss. Increasing the feedback loop frequency decreases its idle time. Therefore, high feedback loop frequencies are resulting in fast scans, but can result in slow data transfer rates due to strongly decreased communication loop execution times.

Feedback Loop Frequency

The iteration speed of the time–critical loop determines the dynamics of the feedback control. For realizing a stable and robust tip–sample distance control, the loop frequency must significantly exceed 1 kHz. By monitoring the microsecond time of every loop iteration, analysis of the iteration speed is made. Doing so, the systems limits for deterministic control can be estimated by comparing the desired loop periods with

the ones measured. The histograms for desired frequencies from 8 kHz to 14 kHz are shown in figure 4.5. The histograms show that for loop frequencies of 8 kHz and 10 kHz

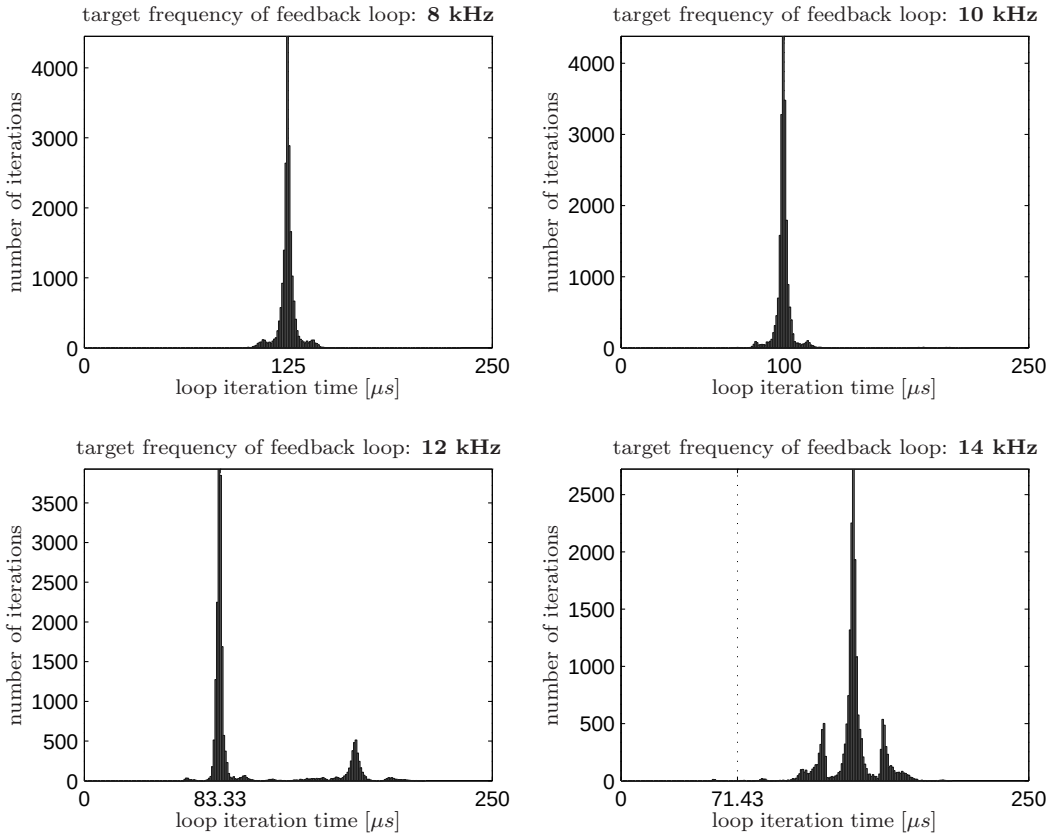

Figure 4.5: Timing analysis histograms of the time–critical feedback loop (20.000 iterations monitored). With the developed system, stable real–time performance is possible for control loop frequencies up to 10 kHz.

the duration of all iterations is within a small error–interval around the corresponding desired loop period. This is not the case for 12 kHz and 14 kHz frequencies. Obviously, for 12 kHz many loop periods are much slower than the desired 83.33 μs. A significant number of iteration takes twice the time as is demanded. If the target feedback loop period is lowered to 71.43 μs (14 kHz), then nearly all of the loop iteration periods are too long to follow up. The main peak of the 14 kHz histogram is at about 143 μs (7 kHz). Nearly all of the iterations execute twice as long as demanded.

Scanning Piezo Stages Dynamics Compensation

The scanning piezo stage is controlled over input voltages for each of its three axes. In closed loop mode this control signal is compared with the actual position of the stage using built–in sensor signals. The response of the stage on input signal changes takes time. As can be seen in figure 4.6, the time needed for answering to a voltage input change is in the 10 ms region for the P–517 stage. Hereby arises the problem of how to

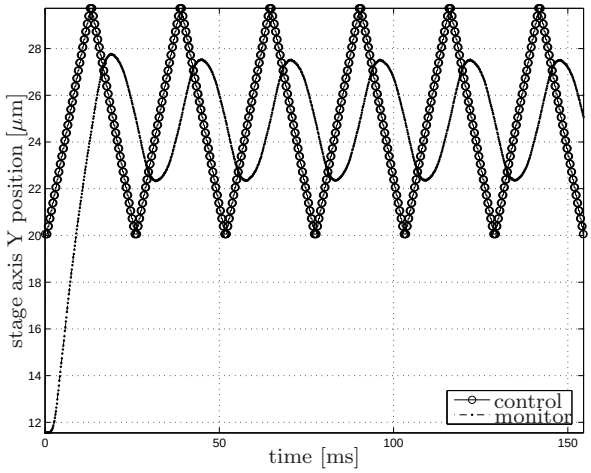

Figure 4.6: Scanning Stage Speed Limitation. The fast scan control signal is applied for scanning 12 rows of 10 micrometers within 155 ms. The monitored signal illustrates that the stages answer is delayed by about 10 ms and that the lateral positioning error is almost 50%.

exactly analyze the lateral position of the stage (and sample) during the SICM scan. A solution is given by taking the difference between the control signal and the monitor signal of the stage's X and Y axis into account (figure 4.7). For each pixel the vertical control of the tip–sample distance is made by the PID. Lateral control is made by evaluating a pixel to be stable only if the absolute value of the difference between the control and the monitor of both lateral stage channels is below a mutually chosen threshold. By adding these two conditions (one for each channel of X and Y, respectively) to the distance–control stability condition, the error in the lateral resolution due to the slow stage dynamics can be reduced. This reduction increases the scanning time. But figure 4.6 shows, that without waiting for the closed–loop position control of the stage, the displacement must be expected to be some hundreds of nanometers. The influence of waiting for the movement of the stage at each pixel is illustrated in the comparison of the detailed plots shown in figure 4.7. The left plot shows the lateral movement of the stage without waiting. The dashed line shows the control command increasing with time (and pixel number) to give command for the execution of a row–scan. Reaction of the stage is depicted by the solid line. The dots show the stages position during the last six iterations of the control loop before evaluating a pixel to be stable concerning

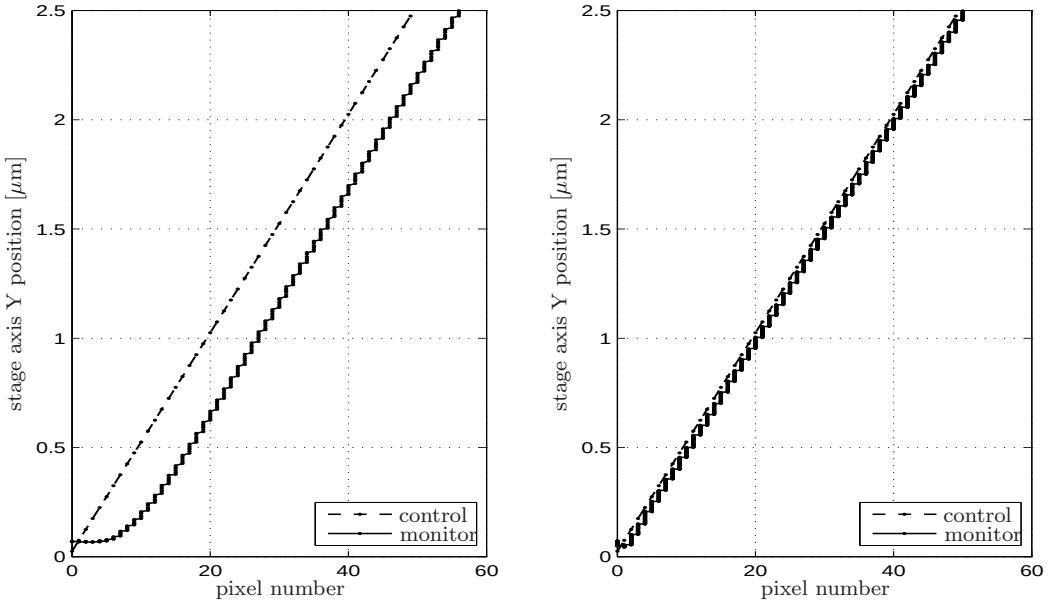

Figure 4.7: Scanning stages lateral axis at first 60 pixel of a SICM scan. Left: Without waiting for the stage to fully come into desired lateral position. Right: Waiting at each pixel until the absolute difference between control and monitor signal of the stage is below 25 mV (= 25 nm).

the vertical distance correction. This is a visualization of the verbose mode. After a slow movement in the first 10 ms (initialization time), the stage reaches its steady–stage velocity. Nevertheless, a large steady–state difference between the control input signal and the output signal of approximately 300 nm is measured. In the right plot a row scan with applied waiting–function is visualized. For both channels, X and Y, the control loop waits until the difference between input and monitor signal is equal to or below 2.5 mV or 25 nm.

Generation of the Feedback Transfer Function

Figures 4.8 and 4.9 show a curve of the LIA response depending on the tip–sample separation while approaching on an oil/water interface (black). First, the feedback transfer function plotted in figure 4.8 is compared with a single exponential fit. The fitting algorithm terminates yielding

$$\mathrm{LIA_R(z)} = 4.577 \times 10^{-3} \cdot \exp\left(15.23\mathrm{z}\right) \tag{4.1.1}$$

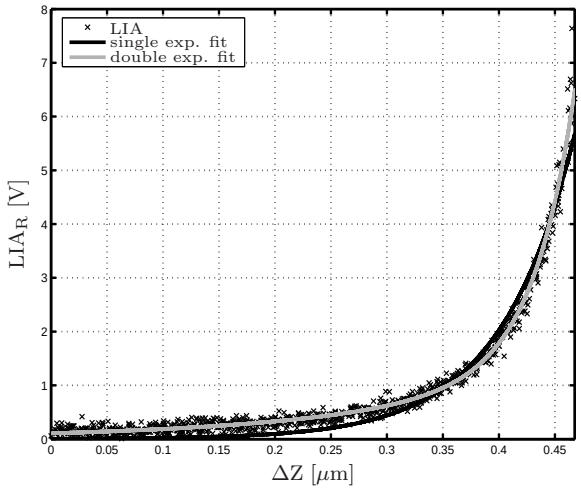

Figure 4.8: Comparison of the LIA response during approach on an oil/water interface (black) with a single–exponential fit and a double–exponential fit. Fit parameters can be found in the text.

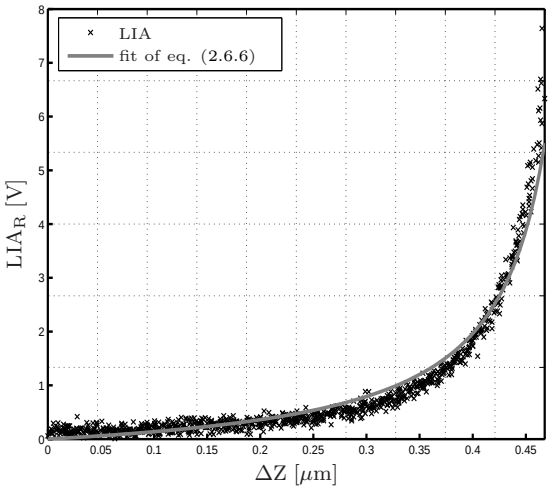

Figure 4.9: LIA response during approach on an oil/water interface (black crosses) compared with a fit of equation (2.6.6). Fit parameters can be found in the text.

(black curve). Obviously, the goodness of the fit is relatively poor (root mean–squared error is 0.237). Fitting a sum of two exponentials yields

$$\mathrm{LIA_R(z)} = 1.074 \times 10^{-1} \cdot \exp\left(5.566\mathrm{z}\right) + 1.364 \times 10^{-5} \cdot \exp\left(27.41\mathrm{z}\right) \tag{4.1.2}$$

(gray curve). The latter result is in good agreement with the experimental data (root mean–squared error is 0.129). Figure 4.9 shows the LIA response compared with a fit of equation (2.6.6). The plotted line (gray) is proportional to a function given with the following parameters: $\mathrm{r_0} = 69$ nm, $\mathrm{a} = 40$ nm, $\mathrm{L} = 20 \times 10^{-7}$ m, $\mathrm{d} = 100 \times 10^{-9}$ m, and $\mathrm{f} = \omega/2\pi = 1.2$ kHz.

Linearization of Feedback Transfer Function

Distance control is calculated by the PID algorithm according to equation 2.7.7. As is described in section 2.7, a stable control depends on a linear transfer function.

The transfer function that transfers from an input into the physical scanning system (tip–sample distance change) and an output of the system via the lock–in detection is given by equation 2.6.5. It is non–linear, and for stable control this function has to be linearized so that equal magnitudes of the control output result in equal magnitudes of the system response. This is done by dynamical normalization of the PID gain $\mathrm{K_C}$ (see figure 4.10). Even in the small working range of the feedback control – some hundred

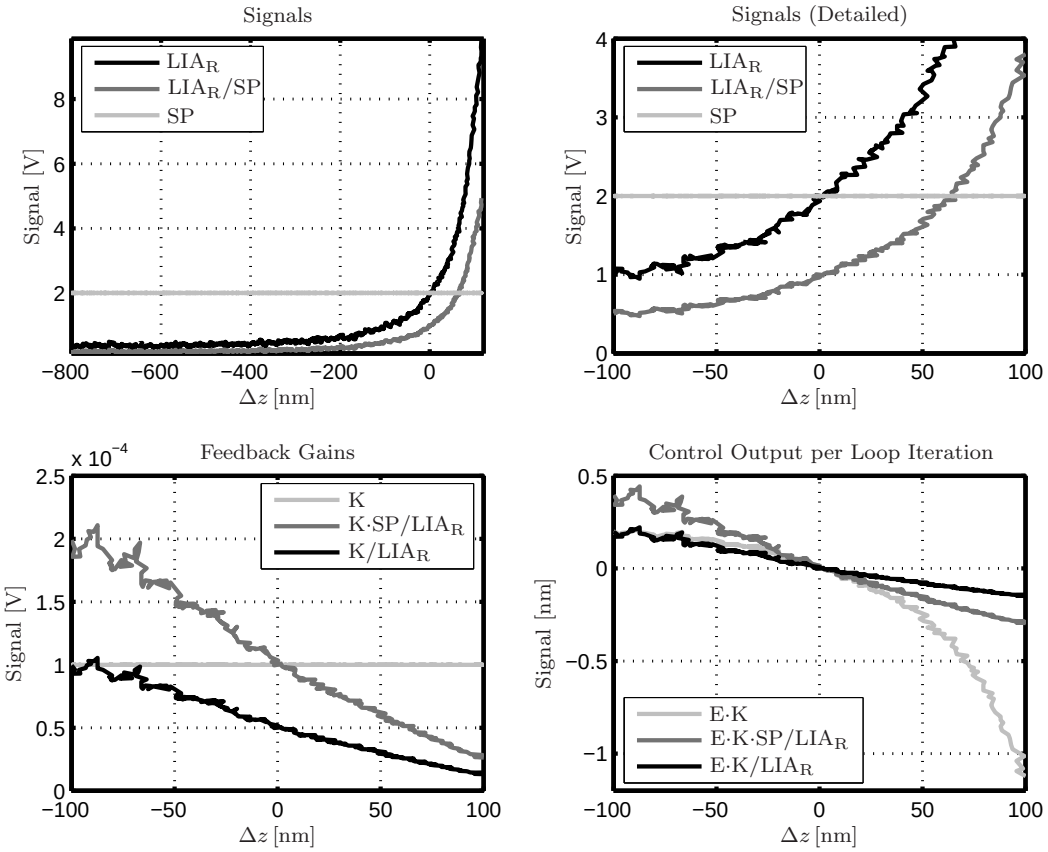

Figure 4.10: Top left: The nonlinear control signal (black) and a mutually chosen setpoint of 2 (light gray). The line in dark gray shows the normalization ratio that becomes unity at the working point at $\Delta z = 0$. Top right: Details in the working point region. Notice the asymmetrical shape. Bottom left: Normalized PID gains. Bottom Right: Linear normalized output.

nanometers around the reference point, the control signal provided by the lock–in amplifier (black curve in figure 4.10) is nonlinear. For multiplicative linearization of this input response, a signal is needed that compensates for the exponential shape of the lock–in signal. Furthermore, this signal must become unity in the setpoint (reference) region. By dividing the PID gain K_C by the ratio of the LIA-response to the reference point, $K_C = K_C / (LIA_R/SP)$, a reasonable linearization strategy of the feedback control is obtained (dark gray curve in the feedback gains plot and in the control output plot).

The non–normalized light gray curve in the control loop output plot indicates the extremely strong control responses that would occur at small tip–sample distances. On the other side, the feedback correction would become small at large separations. This

shape would make the feedback tending to oscillations if the PID gain K_C is chosen high enough for realizing a fast error minimization from too large tip–sample distances. These oscillations would be disturbing to the scan process or even make the probe tip come in contact with the sample surface. In the case of setting K_C small enough for avoiding too aggressive error correction at small tip–sample distances, the control could be 'switched off' at large distances.

The dark gray curve shows the linear dependency of the control loop output from the tip–sample separation in the case of linearized PID algorithm gain. This makes the control stiff and stable and avoids tending of the control to oscillating behavior when setting the proportional gain large enough for fast error correction. To limit the dynamic adjustment of K_C for not letting the control become too aggressive, the normalization of K_C can be confined within a predefined percentaged interval around the initial value of K_C. Most commonly, 50% to 90% are chosen here for the limitation of upper and lower values. If the nomalized gain is above the upper limit, the upper limit itself is chosen as the actual control gain. If on the other side the LIA signal is high enough to decrease the gain below the lower limit, the lower limit is fed into the PID algorithm for not disabling the distance control. Disabling of the feedback control could otherwise occur if the gradient of the transfer function becomes smaller than the noise in the working distance of the control (some tens of nanometers) or if the control output becomes infinitely small by strong normalization.

4.1.2 Probe Holder

The pipette holder is a crucial mechanical part of the SICM, since it has to fulfill several requirements of which the most important is the transmittance of the mechanical oscillation of the piezo stack to the scanning nanopipette with a sub–nm accuracy. The holder has been manufactured by the machine shop of the physics department at the Bielefeld University. It consists of three parts (A to C, see figure 4.11). Part A is an aluminium–bail of 13 mm width and 32 mm height, permanently fixed at the PA8/12 piezo stack movable thread. Part B has a T–shaped profile resulting in formation of a bar. This bar contains a U–type groove of 1 mm depth which can contain the pipette. The pipette is then held by adding the complementary part C that has an U–type profile and gently tightening six screws (M2×10), hereby increasing compressive force between part B and C thus clamping the pipette. Both parts B and C are made of Victrex® PEEK™ (polyetheretherketone),Victrex plc, Lancashire, UK, a

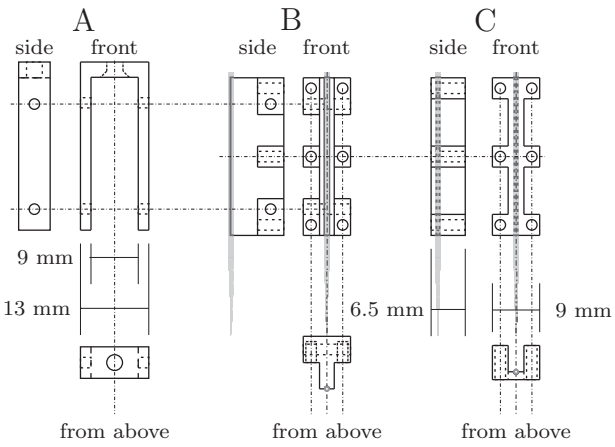

Figure 4.11: Drawing of custom–made holder for 1 mm outer diameter nanopipettes. The holder consists of three parts (A to C). Adaptor Part A is screwed into the 3 mm thread of the piezo–stack and consisting of aluminium. Parts B and C are made of polyetheretherketone (PEEK) due to weight optimization, electrical insulation issues and less capacitive coupling. These two parts are fixed by 6 screws (M2×10) and holding the pipette by clamping it in two half–cylindrical grooves. The pipette is denoted in grey color. Total weight of the holder without pipette: 4.8 g.

high–performance thermoplastic. This is because the density of polyetheretherketone is only 1.3 g/cm^3 thus the total weight of the pipette holder is below 5 g. As has already been mentioned in section 3.9, during dynamic applications of piezo–stacks, a low accelerated mass increases the maximum dynamic frequency and ensures minimal amount of shear–forces that could otherwise be harmful to the piezo–system mechanics. Besides that, PEEK–polymer possesses several advantageous properties. It is chemically resistive and inert, offers a high wear resistance, has a high electrical volume resistivity of 10^{14} Ωm at room temperature, a dielectric constant of $\epsilon = 3.2$ and finally a low dielectric loss factor of $3 \cdot 10^{-3}$ at 1 MHz *[*Victrex plc*, 2007]*. Especially the electrical properties of this polymer are important for its application as pipette–holder material for SICM. The steel housing of the piezo–stack itself is electrically separated from the driving signal only by a low resistivity of about 20 Ω. PEEK's high volume–resistivity allows for good shielding of the probe from the housing of the piezo stack. Furthermore, low dielectrics of the material surrounding the pipette lead to less capacitive coupling (see section 2.4).

4.1.3 Isolation and Damping

Electromagnetic Isolation

Due to the small aperture size of the pipette tip, the resistivity against currents flowing through it is in the range of tens to hundreds of megohms. So, a potential difference of 100 mV between the inner and the outer solution causes an ionic current of about

Figure 4.12: Photograph of the piezo stack actuator with the pipette holder attached.

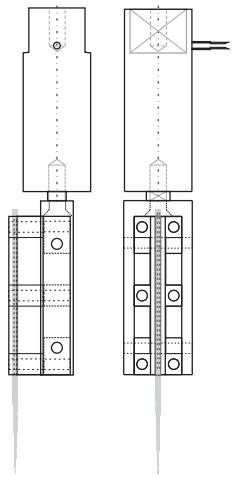

Figure 4.13: Drawing of the pipette holder and the stack actuator. Side view (left) and front view (right).

1 nA. Stable low–noise measurement of this signal and phase–sensitive detection of its modulation is a task that is performed by the headstage–amplifier, the microelectrode amplifier and the lock–in amplifier. For optimal performance, segregation of the ionic current circuit against electromagnetic pickup has to be realized due to the extensive noise signals radiated from power supplies and other equipment inside the lab. This is done by surrounding the local setup, i.e. the headstage with its connectors and the bathing solution with the pipette and its holder by a grounded metal cage (Faraday cage). Effectiveness of this EM–isolation is presented in figure 4.14. Here, a period

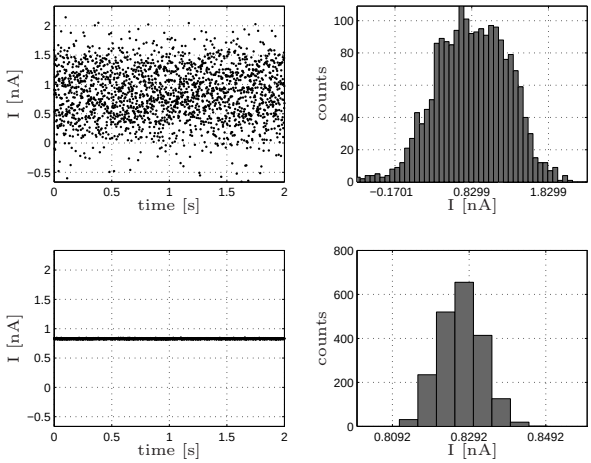

Figure 4.14: Top: Ionic current while circuit is not isolated against electromagnetic pickup. Bottom: Current with ionic current circuitry isolated by grounded metal shielding. Right: Histograms of current signals shown at the left. Standard deviation changes from 475 pA for not isolated setup to 5.8 pA for when circuit is isolated. The mean current does not change (0.8299 nA to 0.8292 nA). Measurement bandwidth 10 kHz.

of 2 seconds of current recording with a bandwidth of 10 kHz is shown. While the setup is not covered by the metal cage, the mean current is about 0.8 nA superposed

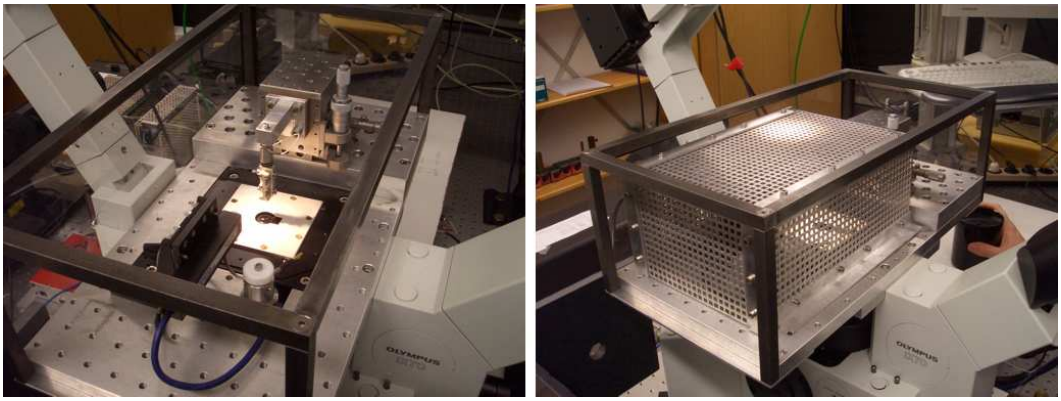

Figure 4.15: Overview over the setup. Left: without Faraday shield surrounding the setup. Right: shielding applied to the setup.

by a large noise. The standard deviation of the current signal recorded is 0.475 nA. Surrounding the setup locally by grounded metal, the mean signal is unchanged, while the standard deviation decreases by two orders of magnitude to 5.8 pA. This noise is near the theoretical limit one can expect using this type of microelectrode amplifier *[*Molecular Devices Corp., *1999]*.

Temperature– and Air Flow Isolation

The SICM scanning principle bases on the phase–sensitive detection of the modulated ionic current. This control signal is extremely sensitive to changes of the oscillating frequency, since the bandwidth of the detection is much smaller than 1 Hz. Furthermore, the inner working principle of the SICM bases on the tip–sample sensitivity of the modulating current amplitude. Making use of this sensitivity forces to make efforts in stabilizing the temperature of the scanning environment. Temperature fluctuations and subsequent thermal movement of mechanical parts of the microscope can cause changes of the tip–sample distance. These changes are being compensated by the feedback control and hereby cause artifacts in the topographical scan information. Any differences of the scanning probe's oscillating frequency from the reference wave are causing sensitive decreases of the lock–in detection signal. As thermal movements, these changes are compensated by the distance control. Therefore the local SICM environment is isolated against air flow by five plexiglass elements attached to a cuboid steel frame (figure 4.16).

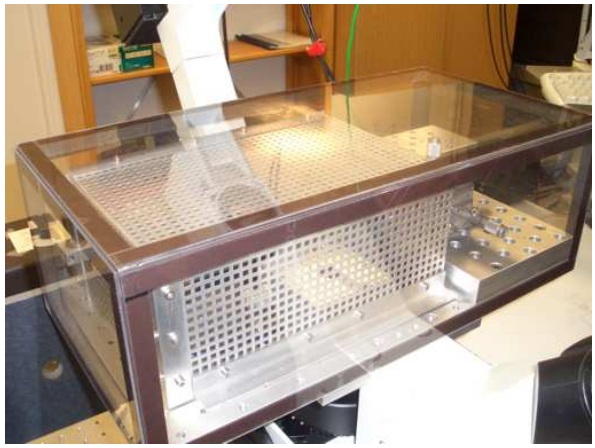

Figure 4.16: The SICM with electromagnetic shielding and plexiglass surrounding for isolation against air flow.

4.1.4 Distance–Control Signal Generation

If the tip–sample distance is short enough, the oscillating tip induces a modulation of the ionic current. Two different approaches for examining the successful transformation of the oscillating input voltage into a mechanical oscillation of the pipette tip and a successive modulation of the ionic current are made.

When the pipette tip is illuminated with a focused laser beam, analysis of the back scattered light intensity at high temporal resolution should yield a modulation that is steadily in–phase with the oscillation frequency. To measure this modulation, the scattered light intensity signal is analyzed by an optical hardware autocorrelator. The result of this autocorrelation is presented in figure 4.17. Here, the reference frequency

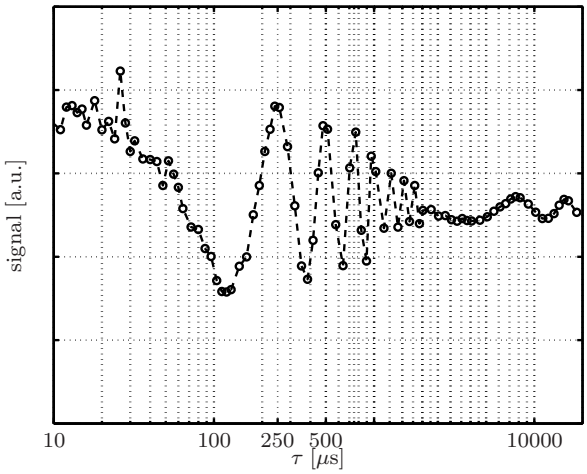

Figure 4.17: Time–correlation analysis of the light intensity back–scattered from the pipette tip at an oscillation frequency of 4 kHz. A time constant of 250 μs shows up.

of the LIA output that is connected to the input of the piezo stack is 4 kHz. The time constant of 250 μs shows up while other time constants are negligible, indicating that the frequency of 4 kHz is transmitted to the pipette tip. Unfortunately, it does not

become clear if the oscillation consists of a mere vertical component only or if there are lateral oscillation components that would not contribute to an effective modulation of the current. To overcome this limitation, the current signal is evaluated at a fixed

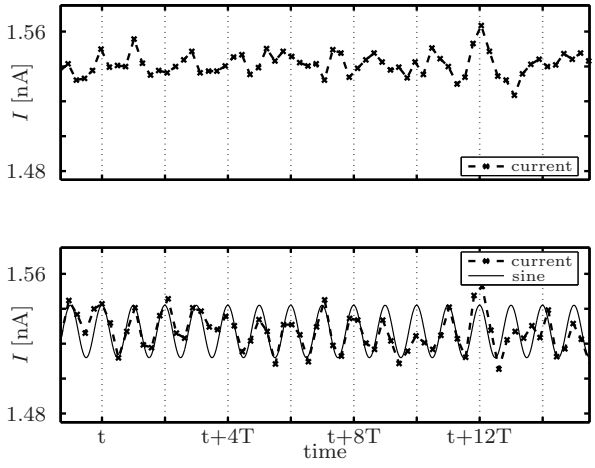

Figure 4.18: Current signal (microelectrode amplifier output). Oscillating frequency 1050 Hz (T=9.52 ms). Oscillation amplitude = 95 nm. Top: Tip–surface distance about 1 mm – current unmodulated. Bottom: Small tip–surface distance: Current modulated with an amplitude of about 15 pA.

oscillation frequency of 1.05 kHz while a glass surface is approached to it. Figure 4.18 shows a period of 16 ms of the current recorded. At a large tip–surface distance, no modulation on the current can be observed, while as the surface is further approached to the tip a modulation of 1050 Hz shows up. As a guide to the eye, a sine curve with a frequency of 1.05 kHz and an amplitude of 15 pA is plotted in parallel to the experimental data. Due to the decrease in the ion conductance, the mean current is decreased by about 10 pA.

Fourier–transformation of the current data gives analytical spectral information (see figures 4.19 and 4.20). The power spectra of the current show that only for the small tip–sample distance there is a significant peak at a frequency of 1050 Hz. All this indicates that the oscillation of the piezo stack successfully transforms into a modulating ion current if the distance between the surface and the sample is short enough. The upper limit of the modulation frequency successfully applied and verified is 8 kHz with an amplitude of 50 mV (53 nm).

Discussion

SICM Control Application

The most important SICM function controls the probe–sample distance. It relies on the strong dependence between the ion current and the tip–sample separation. This sensitive signal is used as process parameter in a feedback control algorithm to keep the

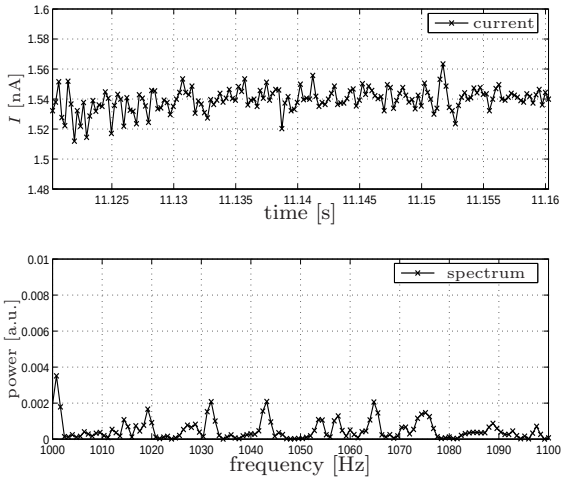

Figure 4.19: Power spectrum (bottom) of current signal (top). Tip oscillation is 95 nm at 1.05 kHz but since the mean tip–sample distance is too large, there is no modulation in the current.

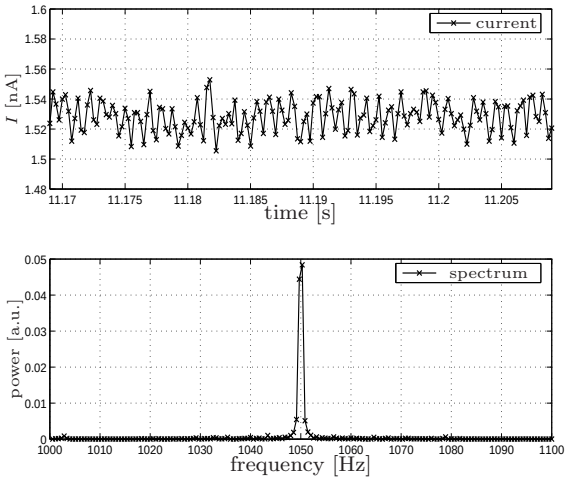

Figure 4.20: Power spectrum (bottom) of current signal (top). Tip oscillation is 95 nm at 1.05 kHz. A modulation with an amplitude of about 15 pA at a frequency of 1050 Hz comes up. A decrease of the mean current can be observed.

(mean) tip–sample distance constant. There are two reasons for driving the feedback control algorithm as fast as possible, i.e. at loop frequencies between 5 kHz and 10 kHz. First, high feedback loop frequencies let the control process become more stable. If there is little time between acquiring the control input signal and giving the output to the microscope stage, small errors in the feedback input can smoothly be intercepted by the control. Second, as any other SPM, the scanning ion–conductance microscope suffers from serial pixel acquisition that makes imaging of large areas taking long time. Therefore, a fast pixel–acquisition time is an aim for being able to achieve a fast scan duration. This pixel–acquisition time depends on how fast the control system is able to reach a steady–state in distance correction. In turn, for fastest reaching of the steady state the feedback loop needs a flat topography leading to no vertical disturbances and high calling rates of the PID algorithm. For securing a constant timing scheme inside the data I/O– system of the feedback control, determinism is necessary. If the time between the acquisition of the input data, the calculation of the error and the output of the correction is not constant for every loop iteration, a stable control would not be possible. Because of the above reasons, special hardware that is capable of fast and deterministic feedback is used for performing scanning ion–conductance microscopy. The SICM application is conceptually adapted to the fact that two CPUs in two different computers are responsible for the microscopes

operation. The software is designed in a way that allows adjustment of all microscope settings, data acquisition and scan control to be executed by the host computer. The successful implementation of the real–time controller program is demonstrated, yielding a fast and deterministic two–loop concept (figure 4.4) which is doing both, feedback correction as well as scan–data transmittance to the host PC. The determinism of the feedback process is maintained by specialized hardware, but this can only be provided up to a certain loop–frequency limit. As can be seen by figure 4.5, the developed system realizes deterministic control for iteration frequencies up to 10 kHz (100 μs period). At shorter desired loop–periods (12 kHz and 14 kHz in figure 4.5), a significantly increasing number of iteration times is beyond the limit that corresponds to the desired period. For a target frequency of 14 kHz, almost all loop iterations are late: The control is still fast, but there is no determinism at all. The fact that for demanded frequencies above 10 kHz most iterations take twice the time as the targeted period, suggests that every second iteration is interrupted by the operating system before its execution has finished. These results are in the region of the limits that are achievable by using this kind of RT controller. Furthermore, a deterministic feedback control at a frequency in the 10 kHz regime is far beyond the capabilities of general purpose computer hardware.

Compensation of the scanning piezo–stage dynamic is important, since the speed of the stage is strongly limited compared to the potential of the microscope's control algorithms. A control input step of 1 V is fully executed after a time of 10 ms to 15 ms. If not taken into account by special waiting routines, the slowness leads to a steady–state error of some hundreds of nanometers when performing a fast row scan. The error can not be decreased by the internal closed loop position control of the piezo stage, since the gradient of the control signal is too large. Therefore, a method is implemented to make the software 'wait' for the movement of the scanning stage and to exactly correlate the lateral coordinates with the image pixel matrix. This error correction is especially important for fast scanning processes, which could preferably occur in smooth topography. As is demonstrated, the waiting function significantly reduces lateral depositioning caused by the delayed movement of the stage. An upper limit for the lateral error induced by the slowness of the stage can be defined, leading to an increase of the positioning accuracy at the cost of time.

Isolation and Damping

Performing SICM measurements without damping and isolation of the central experimental setup against external perturbations is impossible. For the isolation of the central ionic–current circuit against noise pickup by high–frequency electromagnetic radiation, the applied metal shield is demonstrated to be an effective tool. The reduction of the broad band HF–noise by applying the shielding induces a decrease of the ionic current standard deviation by two orders of magnitude. Common values for the standard deviation during SICM scanning are in the range of 1.5 pA_{RMS} to 2.5 pA_{RMS}. So, the application of the metal shielding brings the current noise magnitude as specified by the microelectrode amplifier into the region of the amplifiers intrinsic limitations. Nevertheless, turning off any electrical equipment inside the lab that is not essential to SICM operation is helpful for reaching these low noise level. Especially laboratory light and the microscope power supply have turned out to be responsible for an increase of the current noise. In summary, further improvement on the high–frequency shielding of the setup does not seem to be necessary.

The stability of the microscope's probe with regard to the mean tip position while it oscillates, as well as the frequency of the oscillation is important for successful scanning. These factors are strongly influenced by external influences like movement of the air. On one hand moving air can disturb the probe directly by transportation of momentum when pushing against the probe. On the other hand indirect manipulation of the mean position of the tip can occur through inducing temperature fluctuations and following contraction and expansion of the aluminium cantilever and other microscope equipment. Therefore efforts concerning the isolation against convection of air significantly improve microscope performance.

Distance–Control Signal Generation

Independent from the detection of the modulated ionic current by the LIA, an optical approach for the oscillation of the SICM probe is made. These two independent methods show the successful modulation of the nanopipette together with its holder over an amplitude of up to 100 nm at a frequency of up to 4 kHz. Theoretically, up to 20 kHz should be possible *[*Piezo System Jena GmbH*, 2004]*, though not helpful for the overall scan performance, since other speed limitations do not allow for successful using of such fast oscillations. The time–correlation method of detecting the pipette

oscillation is based on the detection of the pipettes stray–light. Thus, this method does not yield information about the direction of the movement of the pipette. Based on the correlation analysis, it is not possible to distinguish between a desired vertical and useless axial oscillation modes. If the pipette tip would be oscillating in parallel to the surface through excitation of non—axial oscillation modes of the nanopipette, an effective current modulation would not be detected. Therefore, in combination with the results of the fourier–analysis of the current a successful determination of the pipettes oscillation is made, showing that pipette oscillation performs as intended.

4.2 SICM Characterization and Demonstration

4.2.1 Characterization of Scanning Probes

Because of the necessary metal coating, the direct visualization of the scanning probe by scanning electron microscopy destroys the functionality of the nanopipette. Non-destructive examination of nanopipette characteristics is made by measurement of U/I characteristics under standard PBS buffer conditions.

HEAT	FIL	VEL	DEL	PULL
350	3	30	220	
330	2	27	180	250

Figure 4.21: Program for pulling 50 nm apertured nanopipettes out of GB100F-8P glass capillaries using the Sutter P–2000 puller.

By increasing the voltage between the inner and outer electrode from -200 mV to 200 mV while continuously monitoring the ionic current, the current is analyzed as a function of the voltage. Klenerman et al. have reproducibly pulled nanopipettes with aperture size of 50 nm, as is confirmed by SEM. Kindly, they made a set of these nanopipettes available to us for comparison. Results are shown in figure 4.22. All measurements using these pipettes show a resistance of 40 MΩ to 60 MΩ. Comparable pipettes are pulled in Bielefeld from GB100F-8P glass with the following two–line program: They show resistances in a range of 50 MΩ to 100 MΩ, thus comparable to that of the ones fabricated in Cambridge. As can be seen in figure 4.23, the resistance of the nanopipettes linearly depends on the driving voltage. For both kinds of glass, borosilicate and fused silica, it is observed that the overall resistance increases with increasing

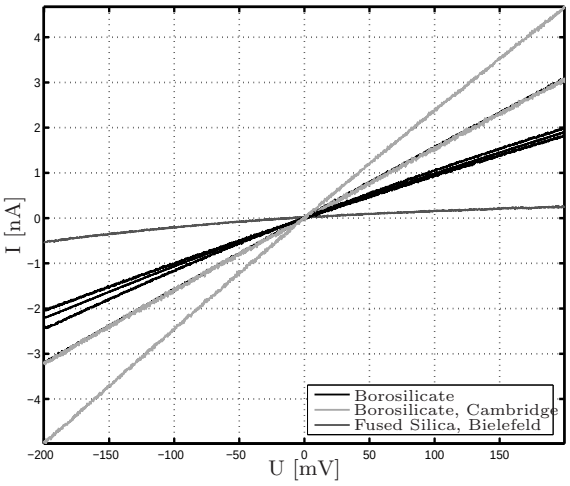

Figure 4.22: Current through tip aperture as a function of the BIAS voltage for different pipettes. Resistances of pipettes pulled from 0.58 mm I.D. and 1.00 mm O.D. range from 50 MΩ to 100 MΩ. Pulling extremely small pipettes with resistance in the GΩ–range is possible by using fused silica (QF100-70-7.5).

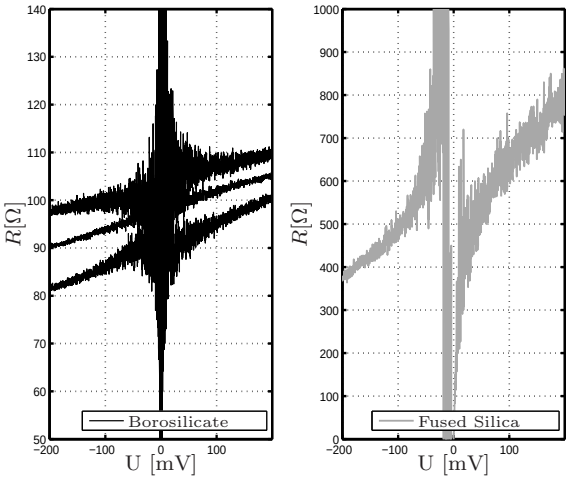

Figure 4.23: Left: Resistances R of 3 borosilicate–pipettes (GB100F-8P) under variation of voltage U. R increases as the potential is increased. Right: R as a function of the voltage measured for a fused silica pipette (QF100-70-7.5). R significantly increases from 400 MΩ to 800 MΩ as the potential is increased.

voltage (potential of inner electrode with respect to grounded outer electrode). This effect increases with decreasing nanopipette aperture size.

4.2.2 Feedback Control System Examination

The feedback control is the most central structure of the microscope software. It ensures stable tip–sample distance and directly influences the scanning process since it steers the samples vertical position. Theoretical description of the feedback calculation method is given in section 2.7. At this point, an experimental investigation of the scan parameter dynamics during an experimental control process is made. To do so, a test surface is prepared.

Onto a LabTek–well glass surface that is covered with PBS solution, a drop of some μl of immersion oil is placed. This produces a spherical–shaped liquid/liquid boundary layer between the oil sticking to the glass and the solution. Because it is assumed that this surface is perfectly smooth down to the nanometer scale it should be a useful surface to test the SICM scan control dynamics. Since the surface is soft it does not destroy the pipette tip even if the probe is inserted into the solution. In figure 4.24, a series of three consecutive approaches onto the oil–surface and even into the bulk of

the oil are presented.

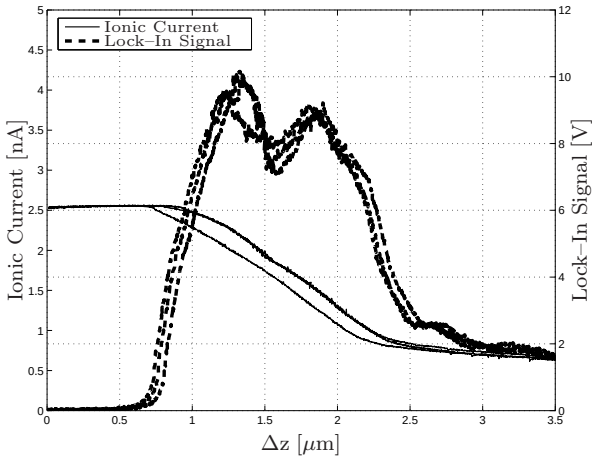

Figure 4.24: Three consecutively performed approaches of a probe (60 MΩ resistance, 100 nm oscillation amplitude) onto an immersion oil/PBS boundary layer. The ionic current reproducibly and linearly decreases within a range of approximately 1.5 μm. The lock–in response is generated as the surface is reached, but includes complex but reproducible behavior when inserted into the drop.

As can be seen by the increasing lock–in response, the SICM control signal can be successfully generated when the tip approaches the oil–surface. Furthermore, the tip resistance is left unchanged after each approach, proofing that the oil does not clog or otherwise permanently influence the pipette opening. Interestingly, both the ionic current as well as the lock–in signal do reproducibly show a characteristic complex shape while the tip is entering the oil. Clearly, these results show that there are complex sample interactions in the tip–region of the pipette. These processes are not well understood and therefore any further experiments on the oil/water layer are being made at large tip–sample distances, where the lock–in response shows its describable exponential shape (in the region of $\Delta z \approx 0.5\mu$m in figure 4.24).

Topographical analysis of an oil drop is shown in figure 4.25. As the contour lines in

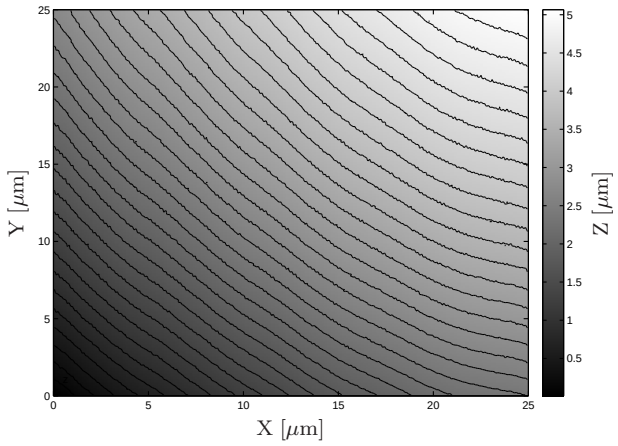

Figure 4.25: SICM scan of the surface of an immersion oil drop. 2D intensity visualization. The contour lines are indicating a vertical distance of 150 nm. Scan range is 25×25 μm^2 resolved with 256×256 pixels.

the image indicate, the height information yielded represents a radial symmetry. A

comparatively large difference between the maximum and the minimum of the height information of 5 μm is measured.

If the number of pixels is decreased, then the lateral step size at a pixel change increases. On the shown area this leads to a strong increase of the vertical displacement of the sample with respect to the probe, i.e. the distance the feedback control algorithm has to move the stage to annihilate the tip–sample separation error. This is a good experiment for testing and tuning the feedback control system. Figure 4.26 illustrates the temporal evolution of the PID control values after a large lateral step to the next pixel of 1.56 μm ($50 \times 50 \mu m^2$ scan resolved with 32×32 pixels). After the voltage step

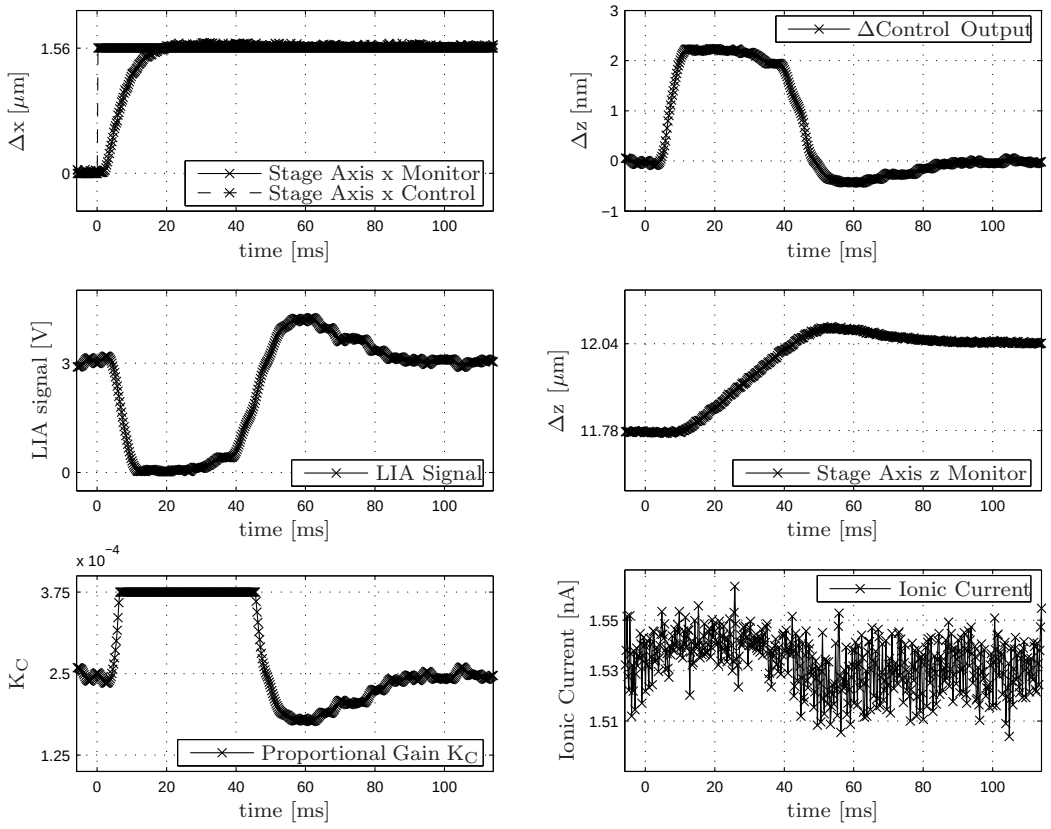

Figure 4.26: Response of the feedback control system to a large lateral step. Sample: Immersion oil drop. The step of 1.56 μm is given to the X channel control of the piezo stage. Within 20 ms the stage follows this command and has reached the desired lateral position. Meanwhile, the lock–in signal vanishes since the tip–sample distance increases. Also the normalized PID gain $\mathrm{K_C}$ increases, leading to a strong growth of the control algorithm output Δz. Subsequently, the stage is raised until the lock–in response reaches the reference value. Overshoot is visible in the lock–in signal as well as the stages vertical position dynamics. For details see text.

corresponding to the 1.56 μm lateral step is applied to the X–channel control input of the scanning stage, (solid line), the stage needs about 20 ms until it has moved (dashed line). Subsequently to the command voltage step, the LIA response vanishes within 10 ms, i.e. before the stage has reached its final position. An increase of the ionic current of some tens of pico–amperes can be detected. The feedback control output per loop iteration increases from 0 nm to 2 nm. Additionally, the normalization of the PID gain K_C takes place (described in detail in section 4.1.1) leading to a further growth of the control output. As can be seen, the normalization of K_C is limited at 50% of the static value of static K_C, which is $2.5 \cdot 10^{-4}$ during this scan. Accumulation of the control loop outputs leads to a linear–shaped raising of the piezo stage until at t=40 ms the LIA reference begins to increase. From now on the vertical correction step size gets smaller since the normalization of the gain leads to a weaker control amplification. Furthermore, the ionic current starts to decrease. At t=45 ms, the error detected by the feedback control is zero. Therefore there is no control algorithm output at this time. After approximately 80 ms the feedback control has steadily eliminated the control error so that depending on the settings for the evaluation of the steadiness the next pixel can be approached. This analysis illustrates the feedback control parameters dynamics and shows the functional principle of the distance correction algorithm.

Adjustment of the Feedback System Gain

In the SICM control system described in this work, participating hardware and software components are designed to work hand in hand by sensitive adjustment of scanning parameters. Most sensitive to the scanning process are the settings for the distance control gain. Empirically it has been proved that for this particular microscope a pure proportional control ($T_I = T_D = 0$) is most suitable for performing the distance control. Nevertheless, complex feedback gains (PI/PD/PID) are applicable but – as far as it has been observed here – always at the cost of overall time and stableness of the SICM scan.

The optimal range for the magnitude of the proportional gain K_C depends on several factors. Responding to an input error arising from a LIA detection change, the feedback loop minimizes the error by performing accumulation of voltage steps at high frequency of up to 10 kHz (feedback loop frequency). The correction should be as fast as possible for decreasing scan–time and for stabilizing the scan by performing fast rejection of the scanned sample if necessary. On the other hand, the gain must

not be too large to prevent the control system from tending to oscillatory behavior, which can be harmful to the sample or the probe. Oscillating feedback loop parameter dynamics are demonstrated in figure 4.27. Since the control overcompensates the error

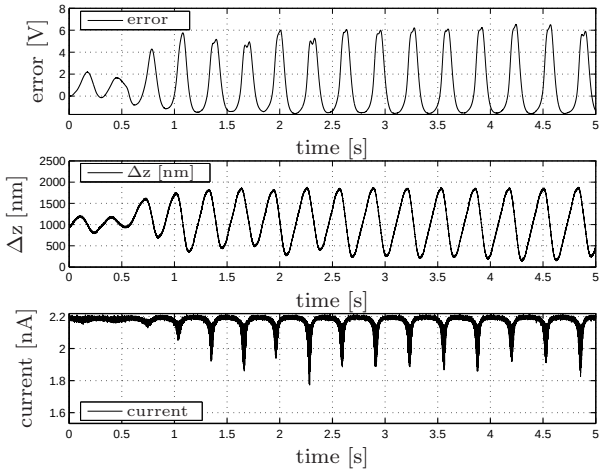

Figure 4.27: Oscillating distance control due to intense control. An oscillating control occurs if the product of the PID gain K_C and the gradient of the transfer function gets too large.

by altering the tip–sample distance, the control gets into steady oscillations. The deviance of the periodical signal from a sinusoidal shape is due to the convolution of the exponentially shaped transfer function $\mathrm{PID_{in}} = \mathrm{LIA_R(z,t)}$ (see equation 2.6.6) and the sinusoidal probe oscillation. However, since the output of a proportional control algorithm also depends on the input signal, the gain K_C must be regarded as the product of the value set in the software and the sensitivity of the LIA. Most commonly, a full scale sensitivity of 20 mV is suitable in a combination with a value for K_C of 10^{-4} to 10^{-5}. Any physical influence that changes the transfer function $\mathrm{PID_{in}} = \mathrm{LIA_R(z,t)}$ (like the LIAs time–constant, the overall gain of the MEA, the scaling ratio of the scanning stage, or the pipette diameter) is associated with a change in the control performance. Also, any significant alteration of the transfer function has to be compensated by an adjustment of the control gain. Empirically, a step size for adjusting the gain K_C of 1×10^{-5} has been found to be suitable.

One–Dimensional Distance Control

Estimating the feedback control quality, resolution and noise can be done by performing pure axial scanning (point scanning), where the lateral movement of the scanned sample is not executed. The only difference between 'point scanning' and normal SICM scanning operation is that the command outputs from the scanning realtime–controller for the lateral channels (X,Y) are not being fed into the piezo–controller inputs. This

means that no lateral scanning but solely vertical distance control takes place. All other scan parameters are kept unchanged. With no lateral movement of the sample, the feedback control is analyzed under nearly realistic conditions but without disturbances from the surface scanning process. Regarding this, an one–dimensional scan produces not a real topographical image, but a matrix containing a time–trace of the scan parameters. Since the system works under nearly realistic conditions, these time–traces contain information about the system–intrinsic scan quality limitations as well as harmful movement of microscope parts. Especially the axial resolution limit can be estimated by this method. Figure 4.28 shows a pseudo–image produced by an one–dimensional scan on a glass surface. As can be seen, although the scanned sample is

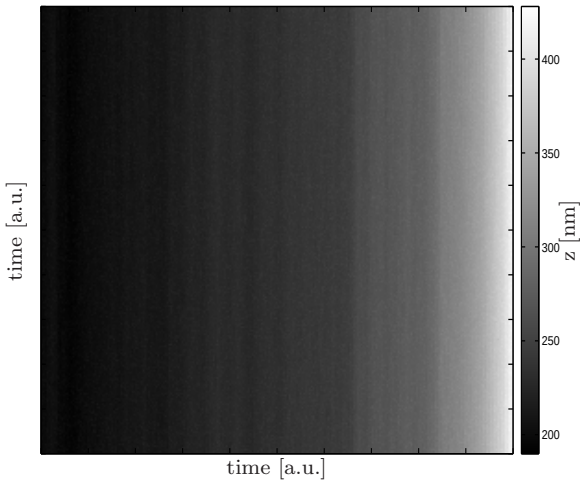

Figure 4.28: SICM image on glass without lateral movement of the sample surface. This testing method provides information about the intrinsic details of the feedback control system and the dynamics of the microscope parts.

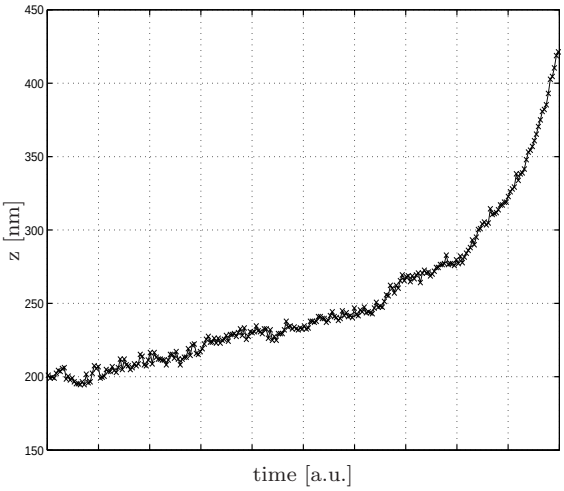

Figure 4.29: Cross section profile of image 4.28. Scan direction is from right to left.

not actively moved in lateral directions, there is a monotone decrease of the samples vertical position by about 200 nm (4.29). This slow vertical movement of the stage is visible throughout the whole scan duration of 860 s. After this relaxation is settled, the result of a one–dimensional scan is similar to that presented in figure 4.30. This image is not corrected for any errors. Besides the fast error component (noise) there is a slow error leading to a wave–like structure. These fluctuations cause an error of about 20 nm in magnitude that can be easily corrected (described in part 'Image Correction' of section 3.14). Presented in figure 4.31 is the whole scan time trace $\Delta Z(t)$. By looking on the histogram of the difference between the Z–values and the mean value of the image (figure 4.32), a rough estimation of the axial resolution of the SICM can be

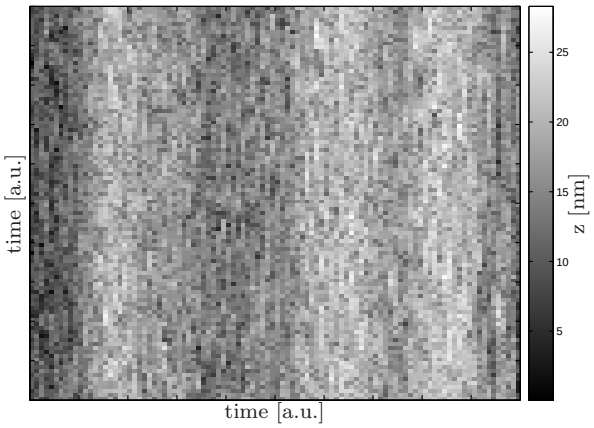

Figure 4.30: Single–point scan on glass. Same sample and position as presented in figure 4.28, after waiting for about 30 min.

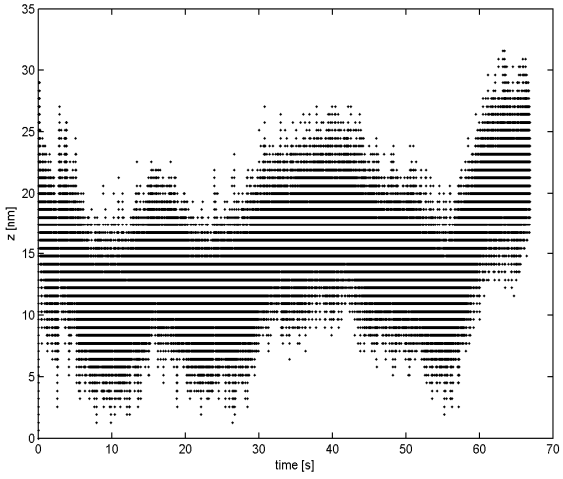

Figure 4.31: Time–trace of the scan presented in figure 4.30. The wave–like structure is due to fluctuations in the LIA–response, compensated by the distance feedback.

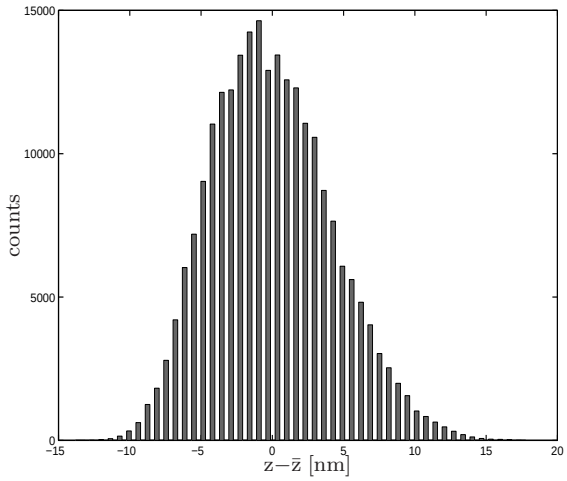

Figure 4.32: Histogram of the height–distribution of the full length of the single–point scan presented on the left.

made. A histogram over 234.000 iterations performed within 66.85 s (3.5 kHz) shows a Gaussian–like distribution of the vertical sample position data. In the histogram plot, peaks positioned every 0.6 nm indicate digitalized character of the step size. The standard deviation of the data distribution is calculated to be 4.2 nm. More detailed studies of the temporal progress of the height are presented in figure 4.33. Here, Z(t) is plotted for different time scales from 1 s down to 2 ms. Regarding long times in the region of one second, the fluctuations that have already be mentioned overrule the intrinsic fast noise, leading to a relatively large variation of the height between 0 nm and 29 nm. This large variance is depicted by the histogram of the Z–distribution, shown in figure 4.34, with a full width at half maximum (FWHM) of 7 nm. Successively decreasing the time–scale from 1 s, 0.1 s to 10 ms and finally 2 ms, the variance

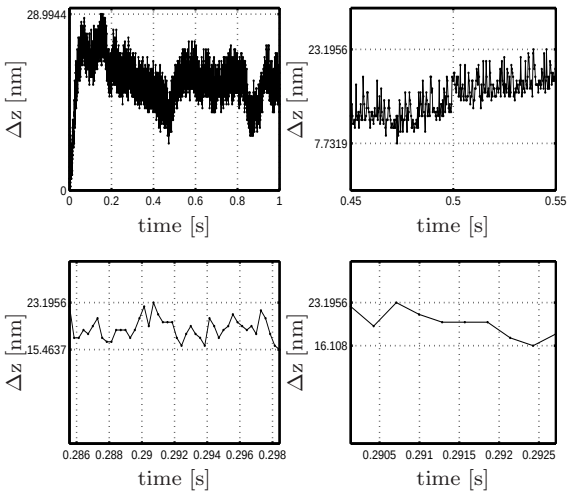

Figure 4.33: Time–traces of different duration (1 s, 0.1 s, 10 ms and 2 ms) of a single–point scan. Feedback loop frequency is 3.5 kHz. The overall height variation decreases towards a limit of about 7 nm.

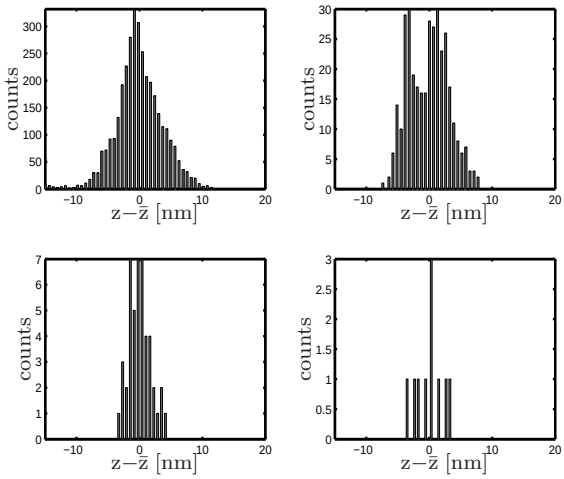

Figure 4.34: Histograms of Z–Distributions of different Lengths. While the sample length is decreased the variance gets smaller, with a bottom line near 5 nm.

as well as the FWHM of the histograms decrease.

Obviously, there is a bottom–line of the variance of the height distribution that is different from zero. For further examination of the time– and amplitude–dynamics of the height distribution, analysis of its standard deviation at different time–scales is performed. To yield information about different time–scales, the standard deviation σ is calculated for different interval lengths. As the sampling rate for the analyzed height–data is 3.5 kHz, one sample equals about 0.286 ms. The whole time–trace under examination consists of 3500 samples. Interval lengths for the calculation of σ are from i=2 samples up to i=1750 samples, corresponding to time–intervals of Δt = 0.58 ms to 0.5 s. In order to enhance the statistic weight of the calculation, for each interval length i the whole 3500 samples are split into $n = 3500/i$ disjoint intervals. For each of the n intervals of length i, the mean standard deviation $\sigma_{\mathrm{n}}^{\mathrm{i}}$ is calculated. Resulting information is depicted in figure 4.35. For short times below 10 samples, corresponding to times between 0.57 ms and 2.86 ms, the mean standard deviation is between 1 nm and 2 nm and increases towards larger times. At large time–scales between i=100 samples (29 ms) and 1750 samples (0.5 s), σ increases from approximately 2 nm to 4 nm. Interestingly, between i=10 and i=100, there is a plateau visible, showing mean deviations of about 2 nm.

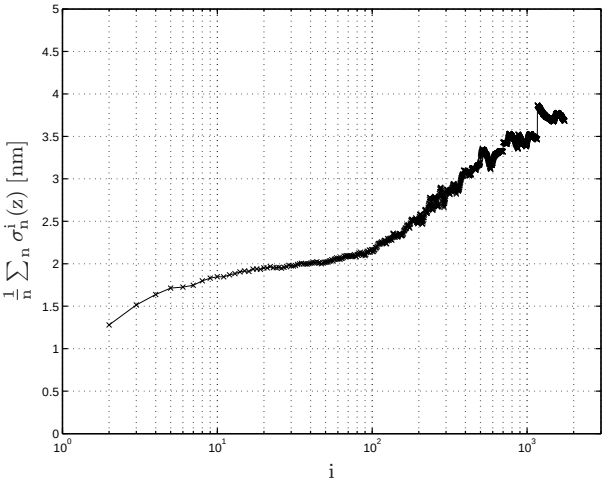

Figure 4.35: Standard deviations σ calculated from the height–distribution shown in figure 4.33 (length: 3500 samples = 1 s). σ is calculated for intervals of lengths between i=2 samples (0.57 ms) and i=1750 samples (0.5 s), summarized and normalized by a simple unweighted mean calculation. The mean deviation is in the range of 4 nm for large interval lengths (0.2 s to 0.5 s) and in the range of 1 nm for a sample length between i=2 and i=10 (0.57 ms to 2.9 ms). A plateau is visible at approximately 2 nm for i=50 samples (10 ms to 20 ms).

Discussion

Characterization of Scanning Probes

Comparing the results of the resistivity curves (U/I–characteristics) yields reliable information about the pipette tip geometries. As no analytical knowledge about the relationship between tip–aperture size, resistance, and the concentration of ions in the solution is available, only a qualitative analysis of the tip size can be made. The borosilicate pipettes pulled the way described obtain a resistance that is equal to or higher than that of those, whose diameter has been determined to be 50 nm as investigated by electron microscopy. Based on this facts it is assumed that the aperture size of the pipettes pulled from GB100F-8P glass with the program shown is 50 ± 10 nm. Considering the approximately 10–fold higher resistance of pipettes pulled of fused silica with a special program gives an idea of the corresponding aperture diameter. It is assumed that the diameter of these pipettes is in the range of the theoretical minimum achievable with this kind of pipette puller, which is 15 nm.

Feedback Control System Examination and Adjustment

Scanning of an oil/water interface is a good method for non–invasive examination and adjustment of the feedback control system. Non–invasive means that the SICM probe is allowed to come into contact with the sample without being damaged or otherwise permanently manipulated. The presented measurements confirm that the distance control mechanism functions well when the probe tip is approached onto the oil surface.

Demonstrated results of the detailed temporal analysis of the distance control routines show a variety of details that elucidate its working principle. Subsequent to the command voltage step, the LIA response vanishes within 10 ms, i.e. before the stage has reached its final position. This is because of the large negative gradient of the drop's surface. The tip–sample distance increases so fast, that there is no LIA signal due to non–existent current modulation. Because of the small LIA response, the feedback control output per loop iteration increases from 0 nm to 2 nm. Additionally, the normalization of the PID gain K_C takes place (described in detail in section 4.1.1) leading to a further growth of the control output. This is in accordance with the data of the ionic current monitor. Because of the increase of the tip–sample distance and subsequent decrease of the resistance, an increase of the ionic current of some tens of picoamperes can be detected. Afterwards an accumulation of the control loop outputs leads to a linear–shaped raising of the piezo stage until after t=40 ms the LIA reference begins to respond. From now on the vertical correction step size gets smaller since the normalization of the gain leads to a weaker control amplification.

Nevertheless, because of system–intrinsic temporal delay, overshoot can be seen at the lock–in detection. This delay is most probably dominated by the delay in the response of the scanning stage, which is in the range of ten milliseconds. Furthermore, this overshoot of the feedback control is partially due to the large vertical error induced by the lateral step on a steep surface.

To summarize, the data of the control loop experiments show that the control system algorithms are working well as far as the qualitative and quantitative behavior is considered. The distance is corrected even for large errors without large overshoot. The normalization of the PID gain works as intended resulting in a well defined limitation of the PID output per loop. The normalization itself is successfully limited, too. This prevents the control system from reaching too aggressive at extreme error levels and hereby makes the distance control more stable.

But although many sophisticated methods are implemented to give stability and speed to the distance control, careful manual adjustment of the feedback gain(s) is still necessary. The sensitive and complex dependency between the control and the transfer function must be understood to be able to adjust the control settings. Although the linearization of the transfer function successfully makes the control independent from its nonlinear shape, it is still not possible to keep the gradient of the linearized function constant from experiment to experiment. For a transfer function ($LIA_R = LIA_R(z)$)

having a large gradient, a smaller feedback gain has to be chosen than for an experiment with a smaller gradient. Mainly, the steepness of the transfer function depends on the probe's tip–aperture diameter.

One–Dimensional Distance Control

The method of point scanning reveals information about intrinsic limitations of the SICM. Since the sample is assumed to be fixed with respect to the scanning stage, all 'topographic' data obtained in point–scanning are no real topographic data but a response of the feedback loop to artificial fluctuations in the LIA signal. These fluctuations are assumed to be caused by several mechanisms. First, there is the monotone drift of the LIA signal. This signal is supposed to be due to a vertical movement of the SICM probe together with its holder and the oscillating piezo actuator caused by mechanical stress relaxation inside the micrometer screw that is responsible for vertical adjustment of the probe. This suggestion is stressed by the fact, that the slow relaxation can only be observed directly after manual adjustment of probe position. Furthermore, the direction of the slow relaxation changes from measurement to measurement, most probably depending on the direction of the 'last turn' (directed up or down) of the micrometer screw before finishing manual probe positioning.

The wave–like structure remaining in the SICM image even after waiting for the slow relaxation to settle before starting the scan, is caused by another mechanism. It has been proven that the signal controlling the PSA oscillation is radiated as an electromagnetic wave from the metal housing of the piezo–oscillator. This signal can induce a small electronic current oscillation at the reference frequency inside the silver wire that forms the electrode inside the nanopipette. Although it contributes to an artificial LIA–response, this signal is still not harmful to the SICM image, since only introducing an constant offset to the height control signal. Unfortunately, the efficiency of the parasitic energy–transmittance between the piezo–housing and the silver wire seems to be time–dependent thus fluctuating on a timescale of tens of seconds. Therefore the LIA signal fluctuates and these fluctuations are being compensated by the feedback control, inducing the wave–like structure that can be seen in almost any SICM raw image. Additionally, alternations in the LIA signal can arise from expansion or relaxation of SICM parts due to thermal flux. As has already been described, this problem can be minimized by isolating the central SICM experimental location. Looking on the time trace presented in figure 4.31, the minimum magnitude in the LIA response fluctua-

tions becomes visible. In this work, fluctuations of amplitudes below 10 nm have not successfully been rejected. The time traces illustrate further the digitalization of the height data. The horizontal stripes are separated by approximately 0.6 nm due to the 16–bit resolution of the DAC. Converting the height data distribution into a histogram yields additional information about the control accuracy. The standard deviation of 4.8 nm of the long–term height–distribution gives a first rough estimate for a resolution of the SICM that can be expected to be approximately 5 nm.

More detailed studies are made using the time–correlated standard deviation analysis presented in figures 4.33 to 4.35. Here, the amplitude of the noise at different time–scales is estimated, resulting in the ability to distinguish between different kinds of noise and fluctuations in the height signal. When the time scale of the noise analysis is decreased, at a certain point all slow fluctuations are singled out. Since these slow fluctuations are due to the fact that alterations in the LIA response are compensated by the distance–feedback system, the noise signal that is left at short time–scales represents a different kind of intrinsic noise of the microscope. This noise cannot be compensated by the feedback–loop since it is faster than for example the stage can be moved in the Z–direction. It is suggested that this intrinsic noise is responsible for the origination of the plateau in the standard deviations shown in figure 4.35. The amplitude of this intrinsic noise is about 2 nm which in this presumption is a bottom–line for the theoretical resolution of the microscope. Naturally, an even smaller bottom line is represented by the 0.6 nm digitalization steps of the DAC. This 'height–quantum' causes the mean standard deviation to tend to values of extrapolated 0.5 nm to 1 nm for an infinitely small interval length. But as is shown by all results, this limit is far below the amplitude of intrinsic noise–limitations. Further analysis of the resolution of the microscope is given in section 4.2.6.

4.2.3 Calibration of the SICM

Demonstrating and testing of the SICM overall functionality and calibration of its topographical measurement capabilities is done by studying a sample with known lateral and vertical dimensions. For this purpose, a commercially available AFM calibration sample is used.

Silicon AFM–Calibration Sample

The calibration sample consists of a quadratic grid of silicon rectangular elevations with rounded edges and with dimensions of $5 \times 5 \times 0.1\ \mu\text{m}^3$ on a silicon surface. The lattice parameter of $0.1\ \mu\text{m}^{-1}$ gives a separation of 5 micrometers between the objects. Result of a SICM scan of this chemically homogeneous sample is presented in figure 4.36. Scanning is carried out with a 50 megaohm borosilcate pipette that is oscillated with 2.76 kHz. The dimensions of the scan area are $26 \times 26\ \mu\text{m}^2$ resolved with 175×175 pixel. Contour lines are plotted every 10.8 nm. Four ashlars are fully imaged and five are scanned partially. Furthermore, four circular shaped signals with a diameter

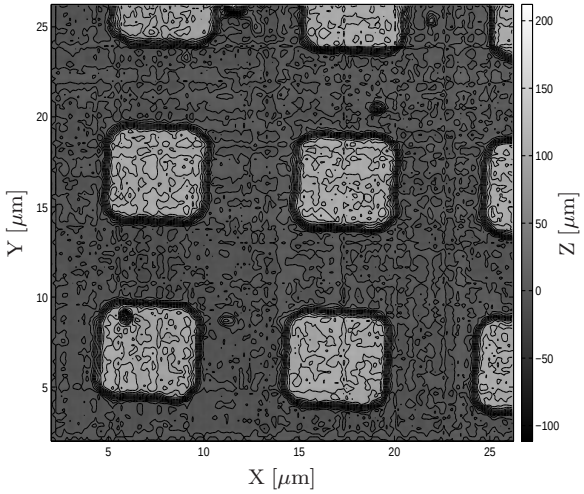

Figure 4.36: Silicon cuboids on silicon surface. Image area is $26 \times 26\ \mu\text{m}^2$ 175×175 pix. The nominal size of the rectangular elevations is $5 \times 5 \times 0.1\ \mu$m.

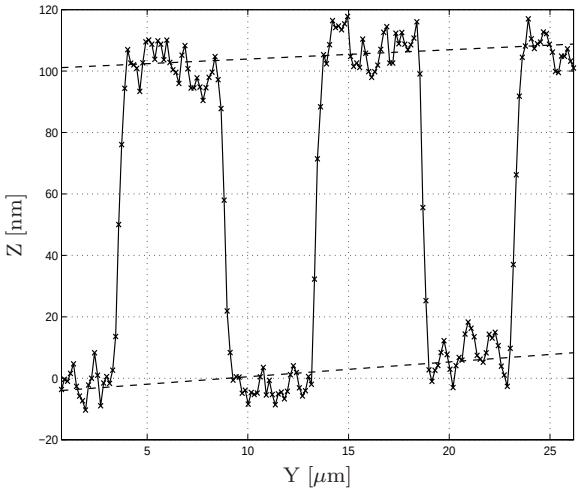

Figure 4.37: Cross section of the Si calibration sample. Upper and lower dashed lines correspond to linear fits of the upper and lower planes, respectively.

of some hundred nanometers and a height of some tens of nanometers are detected. The top plane characterizing the tops of the elevations can be distinguished from the bottom plane by a significant contrast. More precise height information is given by examination of a cross section profile. A profile of this sample is shown in figure 4.37. Fitting linear polynomials to the data for the top– and bottom planes of this sample yields a separation of the planes to be 105 nm ± 12 nm.

Discussion

The scan of the silicon calibration sample proves the correct operation of the SICM. The distance correction works as intended, transferring the interaction of the scanning

probe with the silicon ashlars to an appropriate rejection of the scanning stage. The height corresponds to the nominal height, though superposed by a relatively large error of 12 nm. The large error might be due to the high oscillation frequency of the SICM probe. It is worth mentioning that the probes resistance is not changing during the experiment, indicating that no contact between the probe and the sample takes place. Considering that the nominal shape of the ashlars is a vertical step of 100 nm, it is good to notice that the tip–surface interaction is capable 'climbing' such steps. A lateral component in the influence on the conductivity modulation results in an anticipatory effect that allows to image vertical steps at least of a height of 0.1 μm. If this anticipatory effect would not be present, vertical steps would inevitably lead to a loss of the probe–sample separation and subsequently at least to a malfunction in microscope operation. Understanding of this effect is possible, considering of the hyperbolic, axial–symmetric shape of the electric field direct in front of the tip. Unspecific contamination or non–nominal sample surface is detected, represented by four circular shaped spots. In summary, the scan of the calibration grid documents that the SICM working principle is established and that reliably and stable scanning of samples with a vertical accuracy of at least 10 nm is possible. Lateral precision is demonstrated to be better than some hundred nanometers. Large vertical steps of up to 100 nm can be analyzed without any noticeable tip–sample interactions or irreversible disturbances of the feedback control system.

4.2.4 Scanning of Support Surfaces

In the following sections, applications of the SICM are presented that demonstrate its manifold capabilities. SICM topographical analysis of different systems sized down to the single–molecule level is made to demonstrate the resolution of the microscope. The study of such small samples requires the immobilization of the probes on a substrate (support surface), which must fulfill several criteria. First, its roughness must be small compared to the dimensions of the scanned sample so that it can be well discerned from substrate features. This is especially important for small globular samples. Second, the interaction between the sample and the substrate must be large enough to prevent diffusion of the sample or even interaction with the scanning probe. Lastly, the surface should be transparent and thin to allow for applying optical microscopy and the optical control of the pipettes position during manual approach.

The latter criterion is fulfilled by LabTek chamberslide glass. Because the wells of

these slides can furthermore easily be filled with electrolyte solution, and their walls are repressing disadvantageous evaporation, LabTeks are chosen to serve as the support surfaces in SICM. For further characterization, scans of unmodified LabTek surfaces are executed.

Unmodified Chamberslide Glass

As has been explained above, SICM studies of small samples are prepared on LabTek chamberslide glass surfaces. To see if these surfaces are suitable for SICM application, the pure glass surfaces are scanned initially in an unmodified state ('out of the stack'). The surface of such an unmodified LabTek surface is presented in figure 4.38. Here, an

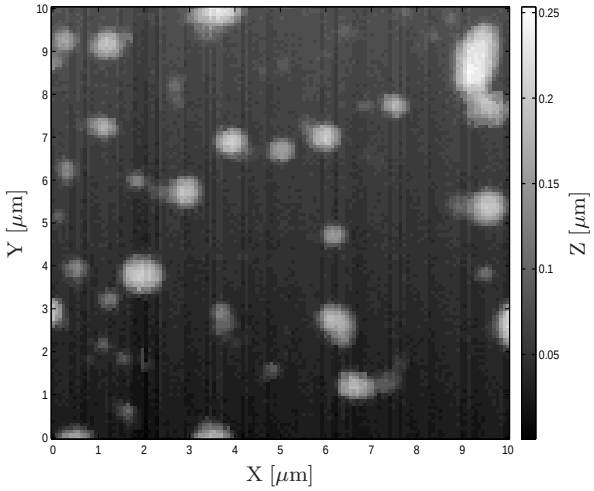

Figure 4.38: $10 \times 10\ \mu m^2$ of an unmodified LabTek glass surface. Many irregularities are detected on the surface indicating that the surface is contaminated with unspecific impurities.

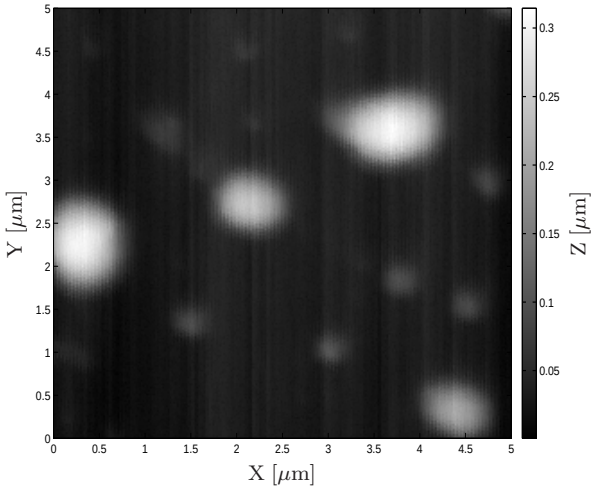

Figure 4.39: $5 \times 5\ \mu m^2$ SICM scan of a fingerprint on cleaned glass. Signals similar to those detected on unmodified glass are scanned.

area of $10 \times 10\ \mu m^2$ is scanned with 128×128 pixels. The electrode voltage is 200 mV and the oscillation amplitude of the probe is 50 nm at 2.460 Hz. A reference point of 2.2 V is chosen for the distance control. Unspecific spots are detected with different diameters sized between 1 μm and 200 nm. The height of these signals is varying between 240 nm and 20 nm. Figure 4.39 shows a high–resolution scan ($10 \times 10\ \mu m^2$, 256×256 pixels) of a glass surface that is touched with the tip of a finger forming a fingerprint. It shows a similar result like the ones of the scan of unmodified LabTak glass.

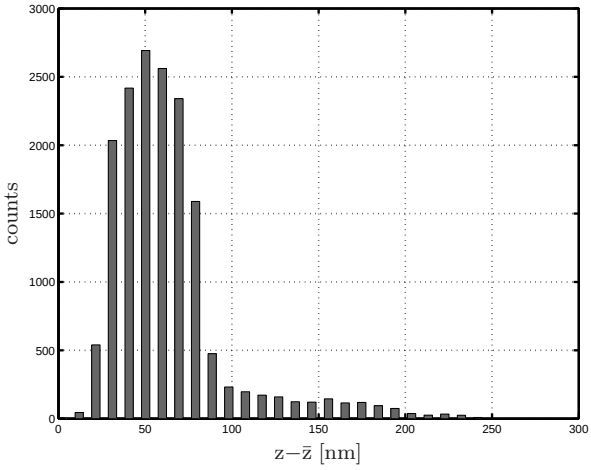

Figure 4.40: Histogram of the scan on an unmodified glass surface. Since for this scan the DAC resolution is 12 bit only, the minimum vertical step size is 9.7 nm.

Etched Chamberslide Glass

Scanning of unmodified glass surfaces reveals that its smoothness is not sufficient for resolving the intrinsic microscope limits or detecting nanometer–sized globular samples.

Therefore, the LabTek well is incubated with 250 μl of a hydrofluoric acid solution

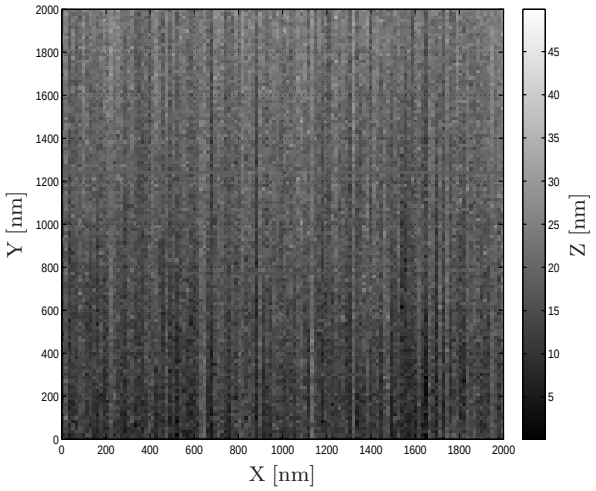

Figure 4.41: Intensity image of a scanned glass surface. LabTek chamberslide well after 1 minute of etching with 0.5% HF.

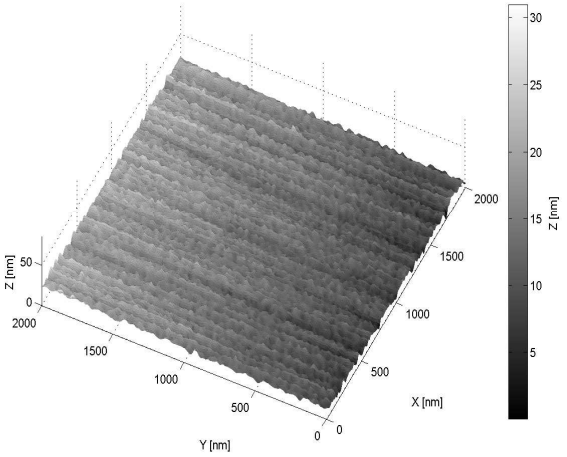

Figure 4.42: 3D–interpretation of a glass surface scan. LabTek chamberslide well after 1 minute of etching with 0.5% HF.

(0.5%) for one minute to etch the glass surface. Afterwards it is rinsed 3 times with pure PBS. Figures 4.41 and 4.42 show results representative for SICM scans performed on etched chamberslide glass. Image dimensions are $2 \times 2\ \mu m^2$ with 128×128 pixels. After HF–treatment, no signals are detected indicating that the etching significantly smooths the glass surfaces. This is confirmed by several SICM scans of other areas and on different chamberslides and wells.

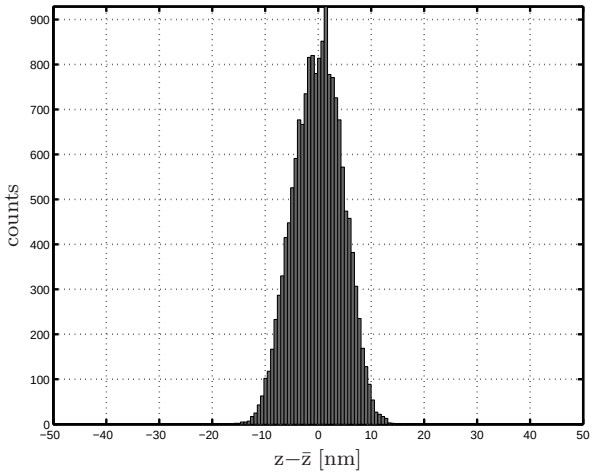

Figure 4.43: Histogram of the scan on a HF–treated glass surface.

APTES Surfaces

Functionalization of glass surfaces is necessary for introducing specific binding interaction between the sample and the surface. For binding of small negatively charged samples like DNA, a functionalization strategy utilizing aminosilanes has been proposed that has been demonstrated to be applicable for AFM *[Bezanilla et al., 1995]*. Coating of the surface with aminopropyltriethoxysilane (APTES) produces a positively

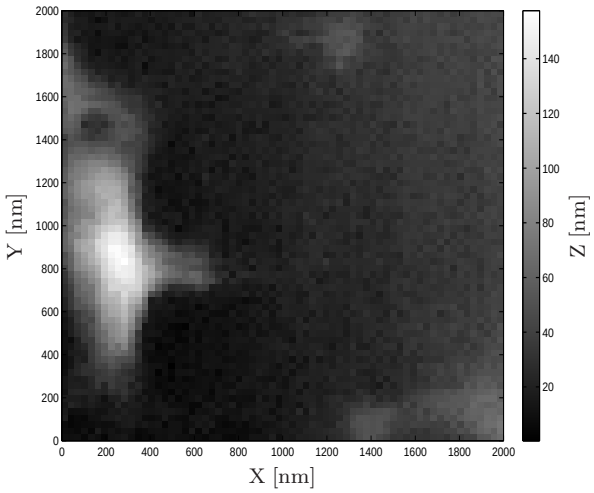

Figure 4.44: APTES on glass. $2 \times 2\mu m^2$, 30 nm/pixel. Surface structures are significantly larger than the SICM axial resolution.

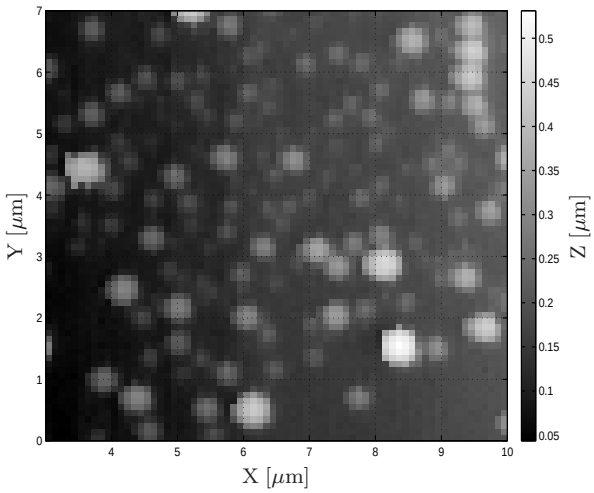

Figure 4.45: APTES on glass. $7 \times 7\mu m^2$, 100 nm/pixel. Many aggregates of different sizes are detected.

charged surface. The binding of negatively charged samples is thought to occur through an electrostatic interaction between the immobilized protonated amine groups of the APTES and the negative charges of the sample *[Crampton et al., 2005]*. The interaction of the APTES coating with the surface is strong even under aqueous solution

and therefore well suited for ion–conductance microscopy. Before scanning, the glass surfaces are treated with a 0.5% solution of hydrofluoric acid in water. Afterwards, a solution of 1% of 3-aminopropyl-triethoxysilane (APTES, Sigma–Aldrich, USA) in methanol is added and washed off with water after one hour of incubation. Figure 4.44 portrays the result of a detailed SICM scan of a 2×2 μm^2 area of this surface. As is confirmed by scanning larger areas (figure 4.45), many objects are being detected on the surface. Most of the signals are circularly shaped with a diameter of between 0.3 μm and 0.8 μm. The measured height varies between 10 nm and 400 nm.

BSA/Biotinylated BSA Surfaces

A different approach in functionalizing a surface for immobilization of molecules under aqueous conditions is a protein–based anchoring technique. Here, the binding of biotin

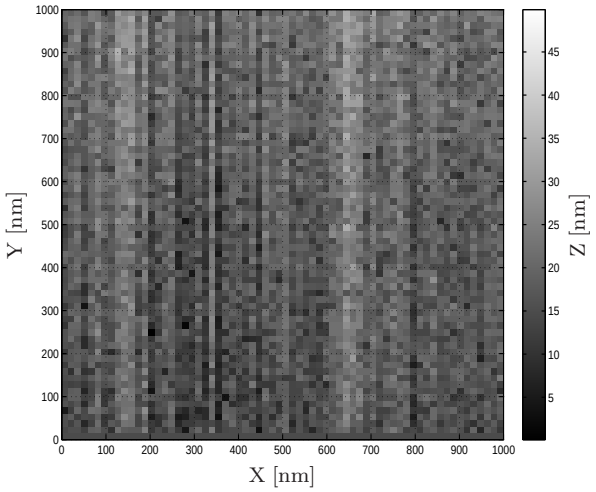

Figure 4.46: Representative result of a scan on a glass surface coated with pure BSA. Roughness cannot be resolved.

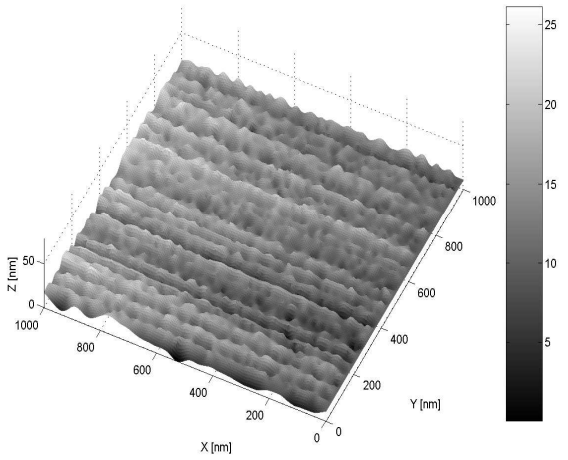

Figure 4.47: 3D–interpretation of a representative result of a scan on a glass surface coated with pure BSA.

molecules with the protein streptavidin is utilized for immobilization. For application of this technique the surfaces are first cleaned by 30 s to 60 s of incubation with hydrofluoric acid (0.5%). After washing off the acid, the surface is incubated for 12 hours with a solution of 5 mg/ml of bovine serum albumine (BSA, Sigma–Aldrich, USA) and about 1 mg/ml of biotinylated BSA in PBS. By variation of the ratio between biotinylated BSA and pure BSA the effective density of the achoring sites on the funcionalized surface can be changed. Afterwards the BSA solution is washed off several times with PBS. Subsequently, the surface is incubated with a solution of 0.1 mg/ml

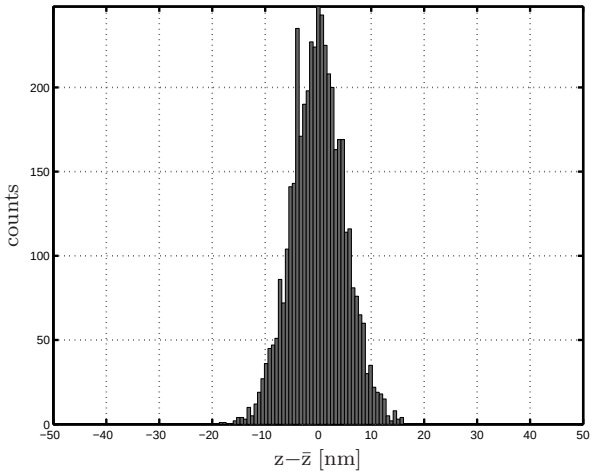

Figure 4.48: Histogram of the scan on a surface of glass, coated with pure BSA.

streptavidin (Roche, USA). Samples having a biotin linker can attach to this surface by binding of the linker to the streptavidin. Figures 4.46 and 4.47 show representative high–resolution SICM images of LabTek glass surfaces coated with pure BSA. Here, even after 12 hours of incubation no signals can be detected indicating a smooth topography of the BSA coating. As can be seen in figures 4.49 and4.50, also a surface coated with BSA and biotinylated BSA (ratio 1:10) does not introduce surface inhomogeneities measurable with the SICM. So it is assumed that the BSA/biotinylated BSA–functionalized LabTeks can serve as support surfaces for SICM topographical analysis of particles sized in the range of the microscopes resolution limits. Surfaces

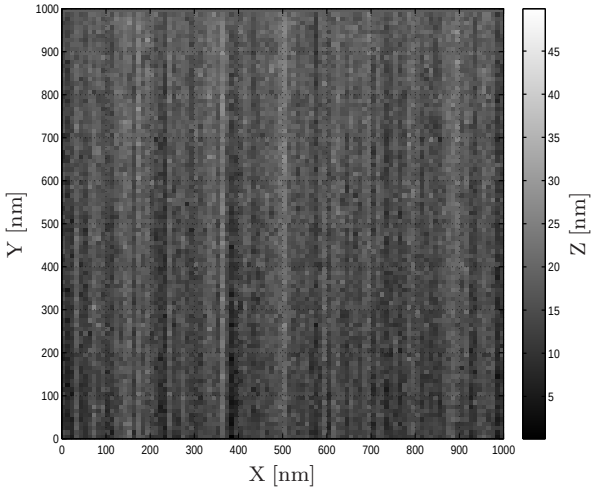

Figure 4.49: BSA / BSA with Biotin. On the SICM–resolution scale, adding of biotinylated BSA does not seem to change the surfaces roughness.

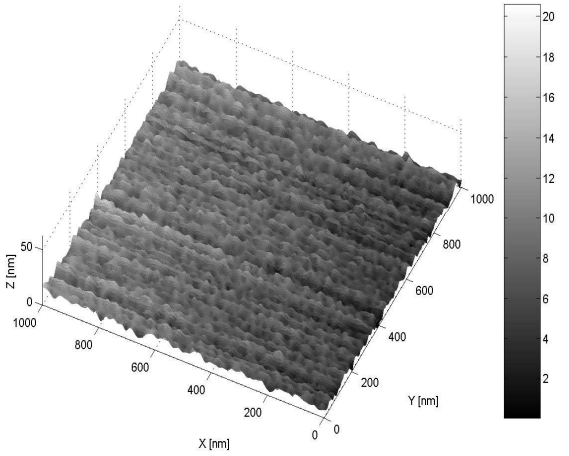

Figure 4.50: 3D–interpretation of the data shown in figure 4.49

coated with BSA / biotinylated BSA are reproducibly analyzed to be smooth without

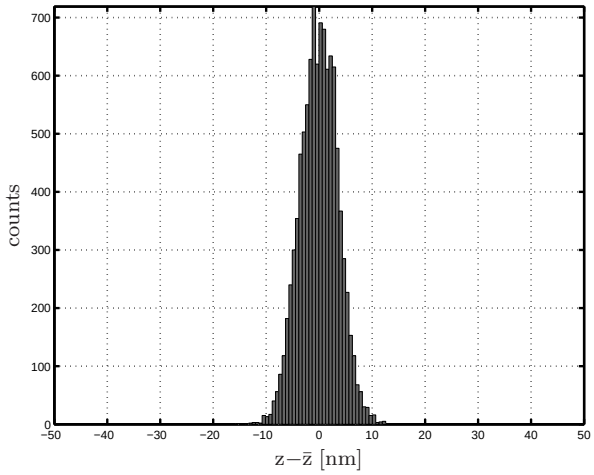

Figure 4.51: Histogram of the scan on a BSA / BSA with Biotin surface.

any signals detectable by the SICM. Therefore the functionalization of surfaces with a solution of BSA and biotinylated BSA is regarded to be the method of choice for the immobilization of molecules and nanoparticles for SICM–scanning.

Discussion

Unmodified Chamberslide Glass

The scanning results on unmodified glass surfaces demonstrate that without further treatment the glass is not suitable for nanometer–resolved surface analysis. Comparison of the unmodified glass surface with a fingerprint shows similar results. This suggests that the signals detected on the LabTek surfaces are not due to intrinsic roughness of the glass surface. The spots are most probably caused by unspecific contaminations that have to be removed by careful cleaning of the surface.

Etched Chamberslide Glass

Etching of the glass induces a large improvement of the surface's smoothness. The scanning studies on HF–treated glass depict the absence of any structures and surface signals. This is even the case for high–resolution imaging of the glass. It is found that the differences in elevation of the surface (due to its roughness) are smaller than about 3 nm and therefore are below the axial resolution of the SICM. These results point out that LabTek wells cleaned by etching with HF represent surfaces that are suited as specimen stages for high–resolution SICM scans.

APTES Surfaces

As indicated by the high density of localized responses in SICM studies, the APTES coating seems to result in the formation of rough surfaces. Occurrance of these signals is possibly due to partial polymerization of the APTES. Factors mainly influencing the roughness of APTES surface coatings have been reported to be the incubation time and the concentration of the solution *[Howarter and Youngblood, 2006]*. Thus, reproducible homogeneous functionalization using APTES with the aim of smooth coatings is regarded to be difficult to realize.

BSA/Biotinylated BSA Surfaces

Support surfaces treated with BSA or BSA/Biotinylated BSA give SICM results that suggest the formation of extremely smooth surfaces. Any signals contained in the SICM images are caused by SICM intrinsic noise and slow control signal fluctuations. Therefore, surfaces functionalized by BSA with biotinylated BSA are well suited for experiments which aim at the examination of the SICM resolution limit.

4.2.5 Combination of SICM and Fluorescence Microscopy

Nanocrystals on Biotinylated BSA

BSA/biotinylated BSA–coated LabTek surfaces are utilized for immobilization of Nanocrystals (QDot 655, Invitrogen, Germany). The Qdot 655 streptavidin conjugate features a red–fluorescent QDot nanocrystal core within a functional coating to which streptavidin has been covalently attached. The product is provided as a 1 μM solution. Nominal size of the nanocrystals as measured by fluorescence correlation spectroscopy (FCS) is reported to be 20 nm to 30 nm *[Doose et al., 2005; Larson et al., 2003; Yao et al., 2005]*. Simultaneous SICM– and fluorescence studies on single semiconductor nanocrystals provide an interesting testing application, since there is a certain fraction of NCs that is non–fluorescent *[Ebenstein et al., 2002]*. The combined simultaneous detection of single NCs by means of SICM and fluorescence imaging could yield information about the fraction of 'dark' nanocrystals.

Surface preparation is done like described in section 4.2.4 with a ratio of 1:1 between biotinylated BSA and BSA. The LabTek well is filled with about 0.75 ml of fresh PBS before 10 μl of a 10^{-9} M diluted solution of the Qdots 655 is added. After some minutes

of incubation the chamber is rinsed gently with fresh PBS, while taking care of not letting the surface come in contact with air. The fluorescence of the nanocrystals is excited by wide–field illumination through a 60x/1.35NA oil–immersion objective using a high-pressure mercury lamp like described in figure 3.1. The excitation light is filtered with a 490 nm bandpass filter, whereas the fluorescence photons are separated from the excitation light by a dichroic transmitting the 655 nm wavelength of the nanocrystal's fluorescence. The collimated beam carrying the fluorescence image is mapped by a sensitive EMCCD camera. Figure 4.52 illustrates the fluorescence intensity of the nanocrystals immobilized on the surface, while the tip of the SICM probe is positioned 10 μm above the center of the imaged surface. The surface is additionally illuminated from above by the microscopes halogen lamp. It is observed, that the density of the

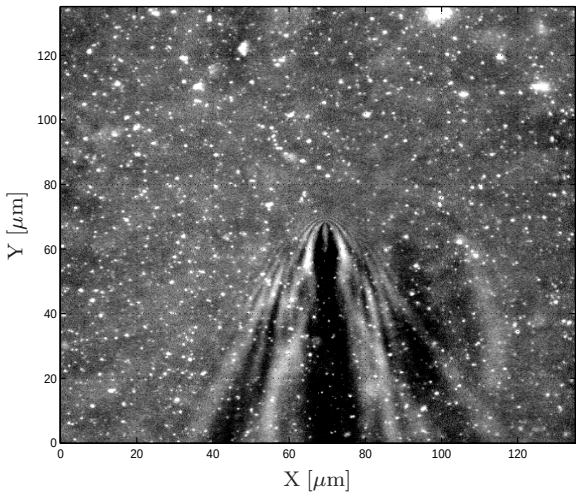

Figure 4.52: Fluorescence image of QDot655 nanocrystals on biotinylated BSA surface. Since the sample is weakly illuminated from above by the microscopes halogen lamp, there is a large background signal and the SICM probe's shadow can be located in the center of the image.

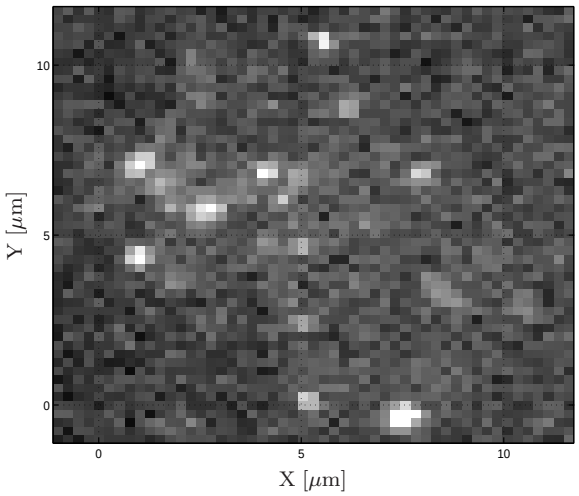

Figure 4.53: Detailed fluorescence–image of an area comparable to that scanned by the SICM. NC density is in the range of 0.2 μm^{-2}.

fluorescence signals decreases fast after washing with PBS. The initial density of approximately 1 μm^{-2} decreases within about one minute down to 1×10^{-4} μm^{-2}. This is confirmed to be the case even without illumination of the sample. The wide–field fluorescence image analysis yields a homogeneous distribution of differently sized spots spread over the whole image. This is the case even after washing the surface several times with PBS. Density of the signals is in the region of 0.1 μm^{-2} to 0.2 μm^{-2}. There is a huge variance in the intensities of the signals, which is stressed by a detailed view

onto the surface (figure 4.53). Here, an area of $12 \times 12\,\mu m^2$ is depicted. While the resolution of the EMCCD becomes visible with 260 nm per pixel, about 20 signals of different size and intensity are detected.

SICM detection on these surfaces is started applying a $10 \times 10\,\mu m^2$ scan. This small area is chosen for being able to do scans at necessarily high lateral resolution in reasonable time. Pixel size is set to be 100 nm (i.e. with 100×100 pixel). Figures 4.54 and 4.55 present results of scanning the nanocrystals on a biotinylated BSA surface directly after adding the solution containing the NCs to the PBS. Obviously there

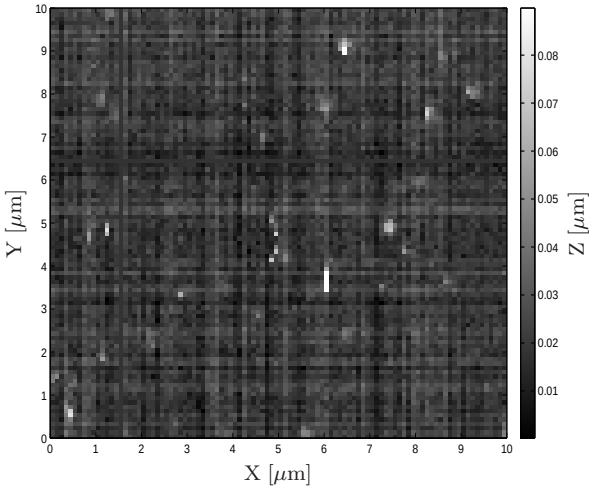

Figure 4.54: SICM scan of QDots655 immobilized on a biotinylatedBSA/BSA surface.

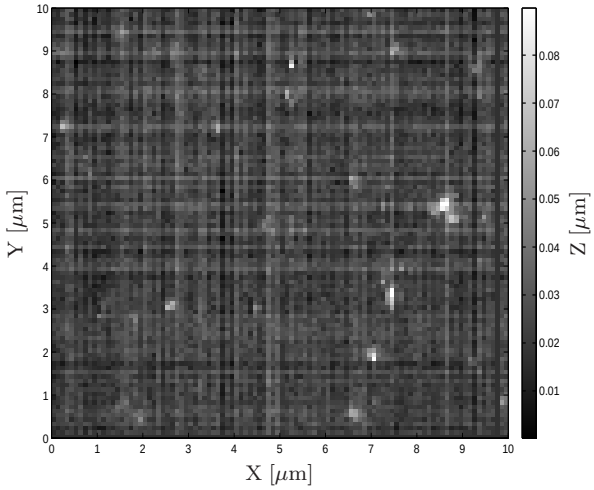

Figure 4.55: SICM scan of QDots655 immobilized on a biotinylatedBSA/BSA surface. Different area.

is a significant difference between the images obtained here and those of the smooth surfaces scanned on glass functionalized with pure BSA/biotinylated BSA. Locally correlated signals are detected in a lateral density of 10 to 20 per $100\,\mu m^2$. Their height is determined to be 20 nm to 30 nm and most of the signals show up to be circular shaped. This density is in good agreement to the density determined by fluorescence analysis. Correlating of characteristic signal–patterns within the fluorescence images and the SICM image data for identification of individual NCs is not successful.

Streptavidin–Labeled Microspheres

For further demonstration of the co–operation of SICM and fluorescence microscopy, streptavidin–labeled fluorescent polystyrene microspheres (TransFluoSpheres, Invitrogen, Germany) are used es scanned specimen. Their diameter is specified to be 40 nm

(manufacturer information). These fluorescent microspheres have an optically excitation peak at 488 nm wavelength and offer an extremely large Stokes shift, since incorporating a series of proprietary dyes allowing excited–state energy transfer between multiple dyes. So fluorescence emission at 645 nm is possible. Again, the immobilization of the samples is realized by functionalization of glass with biotinylated BSA and a ratio of 1:5 between biotinylated BSA and BSA.

In figure 4.56 the fluorescence image obtained by wide–field illumination with a Hg–lamp and an bandpass excitation filter at 488 nm is shown. Successful detection of the

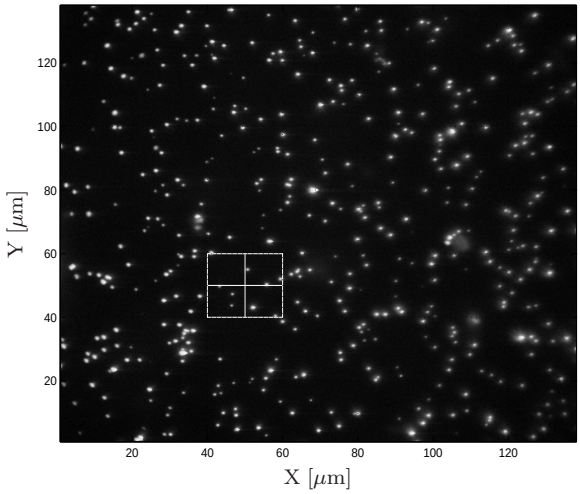

Figure 4.56: Fluorescence image of microspheres bound to a biotinylated BSA surface. Excitation at 488 nm. The emission wavelength is 645 nm.

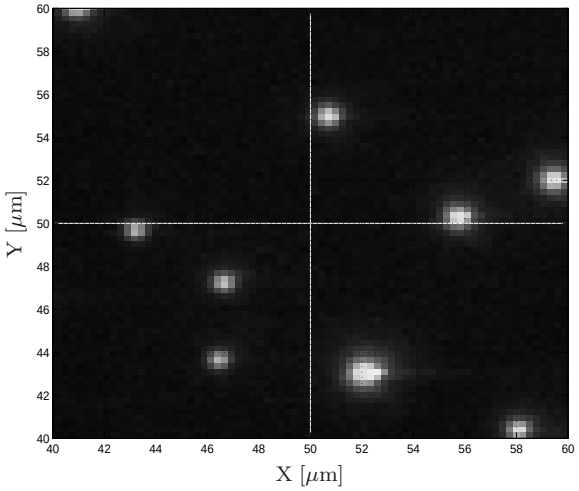

Figure 4.57: Fluorescence image of microspheres immobilized on biotinylated BSA. Detail (rectangle) of the figure 4.56.

streptavidin coated nanoprobes by fluorescence microscopy is demonstrated, with the mean lateral density obtained by optical detection of approximately 2.5×10^{-2} μm^{-2}. The four rectangles visible in the image each mark an area of 5×5 μm^2, which is the size of the area that is scanned by the SICM (data shown below). Figure 4.57 presents a zoomed view onto the fluorescence signals of theses rectangles. The signals are characterized by different diameters and intensities. In contrast to the fluorescence signals of the nanocrystals, the spots monitored on this surface are detectable for several hours. Their density is confirmed to be not changing at measurable levels.

SICM studies on this surface are done using a 40 MΩ borosilicate–pipette, oscillated with an amplitude of 100 nm at 1.2 kHz on an area of 10×10 μm^2 resolved by 100×100 pixel. The result is depicted in figures 4.58 and 4.59. Several signals are detected with heights of 140 nm, 60 nm and 40 nm. The large inhomogeneity and the

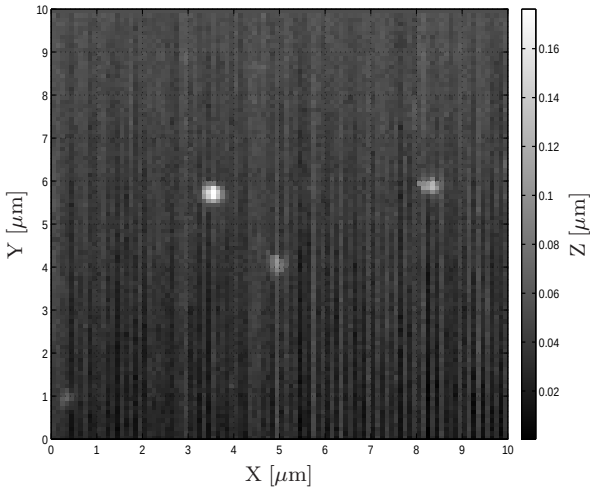

Figure 4.58: Scan of streptavidin–coated polystyrene microspheres (40 nm diameter) on a biotinylated–BSA surface. The density of the signals is corresponding to the one detected optically.

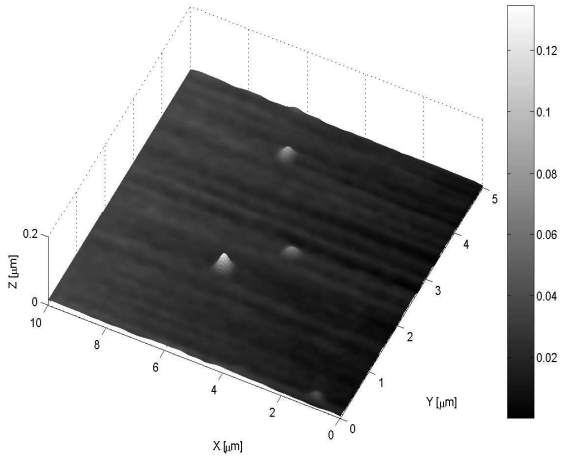

Figure 4.59: 3D–visualization of a study on streptavidin–coated polystyrene microspheres on biotinylated BSA.

difference between the detected height and the nominal height is remarkable. When scanning such small areas, specification of the signal density is afflicted with an large error of about 5×10^{-3} μm^{-2}. Nevertheless the density of the signals is measured to be in the range of 10^{-2} μm^{-2}, thus comparable to the one detected optically.

Discussion

Nanocrystals on Biotinylated BSA

The successful demonstration of combining SICM with fluorescence microscopy illustrates some remarkable aspects of this challenging technique. First of all, the fluorescence data confirms that immobilization of streptavidin–coated NCs on biotinylated surfaces is possible. Even after several times of washing with PBS, the strong signals in the fluorescence detection are present, indicating that the binding of NCs is due to a specific surface interaction between streptavidin and biotin. Furthermore, the initial density of the signals is appropriate for distinguishing individual NCs. The assumption that the fluorescence signals are representing single NCs is stressed by the inhomogeneity in the intensities of equally sized signals. Naturally, some of the larger and brighter spots are detected to be clusters of many aggregating NCs. Nevertheless, much of the variation in the intensities is due to intermittent photoluminescence of the NCs

(blinking) in combination with a limited exposure time of the EMCCD.

A difficulty in measuring the quantum dots is the circumstance that their density decreases so fast. Since this effect is independent from the intensity of the excitation light, it is not explainable by photobleaching of the NCs. A probable explanation is given by unstable binding of the streptavidin–coated NCs to surface biotins. This is confirmed by measurements confirming that the streptavidin–biotin binding constant is reduced by approximately five orders of magnitude when coupled to CDSe/ZnS quantum dots *[Heuff et al., 2007]*. This effect makes it impossible to reliable correlate and identify individual nanocrystals by SICM and fluorescence microscopy.

Figure 4.52 illustrates further difficulties that render the successful identification of individual NCs in the optical and SICM images more difficult. Because of the unprecise and indirect optical definition of the SICM probe tip by referencing to the shadow of the tip, its exact lateral positioning is difficult to determine. Since the illumination of the probe is not done from a position straight vertical above the tip, but is located about 45 degrees from the back of the tip, there is a large parallaxial error between the tip of the probe's shadow and the physical location of the tip. Therefore, a positioning of the probe is possible only with an lateral error of at least 5 μm. This is the second reason that prevents the successful simultaneous identification of an individual nanocrystal by fluorescence microscopy and SICM.

Studies on this probe give a strong indication that the microscope is able to successfully image individual NCs. The signal heights are reproducibly between 20 nm and 30 nm, which is in agreement with their nominal diameter measured by diffusion analysis by fluorescence correlation spectroscopy. Second, the density of the spots detected by the SICM probe is equal to that determined by the analysis of the fluorescence image. The width of the spots is about three pixels. This corresponds to 300 nm, thus ten–fold the nominal cross section of a single NC, which can be explained by the broadening of signals from samples that are smaller than the probe diameter. The effect of broadening of small sample signals is explained in detail in section 4.2.6, where the determination of the SICM resolution is described.

In conclusion, the SICM–detection of the spots is difficult because their height is in the range of the microscope vertical resolution limit, and a fast decrease of the nanocrystal density is observed. Nevertheless, the signal height of about 25 nm and the corresponding fluorescence optical and SICM densities, indicates the successful SICM detection of single NCs.

Streptavidin–Labeled Microspheres

Fluorescence images of streptavidin–labeled microspheres immobilized on biotinylated BSA surface demonstrate the successful immobilization. Contrary to the binding of Qdot 655 streptavidin conjugates, the concentration of the signals is measured to be constant over several hours. The binding of the microspheres streptavidin layer obviously is significantly more stable than that of the NCs. An identification of individual samples in both the SICM and the fluorescence images is not successful. Explanation might be given considering the fact that the SICM probe is not solely scanning the topographical information but also responding to the surfaces chemistry (a detailed explanation is given in section 4.2.7). Besides that, the spatial correlation between the position of the SICM probe and the fluorescence information is difficult, further impeding identification of patterns of individual microspheres.

The width of the signals is broadened by the SICM probe to about 300 nm to 400 nm, which is quite reasonable, since according to its relatively low resistance the pipette tip diameter in these experiments was in the 200 nm region.

4.2.6 Determination of the SICM Resolution

The resolution of a microscope is an important and meaningful property. For determination of the resolution, different samples are scanned, partially after immobilization on functionalized support surfaces. All samples have in common, that their size is much smaller than the expected diameter of the SICM nanopipette and therefore their detection is challenging.

Cell Membrane Proteins

Prokaryotic glutamate transporting cell membrane proteins (ecgltP) from *Escherichia coli* are examined. Having a n-terminal streptavidin–tag (Strep–Tag II, consisting of the amino acids tryptophan, serin, histidine, proline, glutamine, phenylalanine, glutamine acid, lysine), they can be immobilized on a BSA/biotin surface that is saturated with streptavidin via the strep–tag/streptavidin bond. The glutamate–tranporting protein is a homomer, since it consists of three identical subunits, which have a mass of 48 kDa. Each of the subunits is made of 449 amino acids. The nominal size of these biomolecules is 10 nm in diameter.

The preparation of the support surface is performed like described in section 4.2.4 with a ratio between 5:1 and 1:1 between biotinylated BSA and BSA. After that the LabTek well is filled with a concentrated solution of recombinant streptavidin. After an incubation time of 1 hour, the streptavidin is washed off and about 0.5 ml of fresh PBS is filled into the well, before the solution containing the proteins is added.

A presentation of a SICM study on a surface containing ecgltP–proteins is given by figure 4.60. Here, scanning is performed with a borosilicate–probe having a resistance of 50 MΩ. The amplitiude of the probe–oscillation is 40 nm at 1.2 kHz. On an area of 36 μm^2, 10 to 15 circular spots are detected that have a width of 300 nm. The determined height of the spots varies from 5 nm to 20 nm. A cross section profile gives a better illustration of the scanned surfaces geometry (figure 4.61).

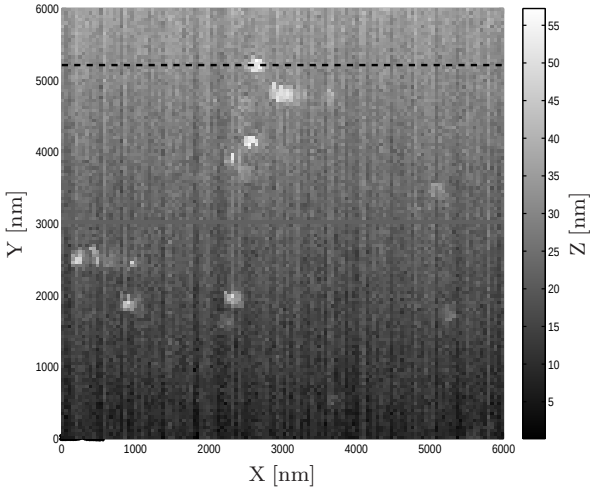

Figure 4.60: SICM image of a biotin–BSA surface with immobilized glutamate transporter proteins. The signal's height is between 5 nm and 20 nm.

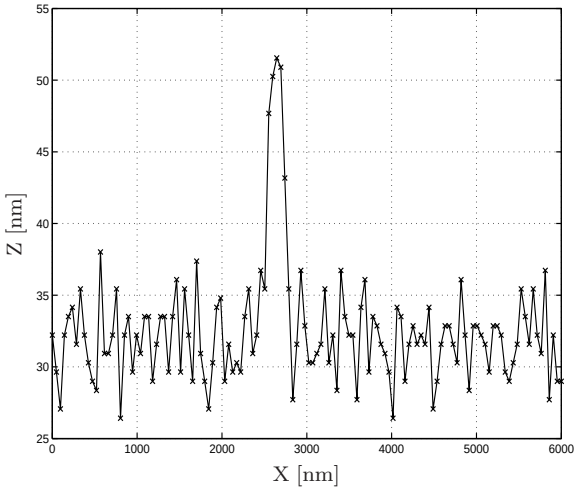

Figure 4.61: Cross section profile of a SICM–detection on a surface with glutamate transporter proteins. (Line in figure 4.60).

Different SICM scans are performed, driven at a substantially higher pixel–resolution. Results are shown in figures 4.62 and 4.63. Figure 4.62 shows a scan of 2×2 μm^2 resolved by 256×256 pixel. For figure 4.63 the pixel–resolution is only half, with 128×128 pixel over an area of 2×2 μm^2. Here, no circular spots but donut–shaped rings are detected on the surface. Since the measured height of these signals is only 5 nm, the rings are buried in noise and are hardly visible. Dashed circles are plotted around the rings to guide the eye. Together, in both plots three rings are visible. For all three cases the outer radius of the rings is 130 nm while the inner radius is 60 nm.

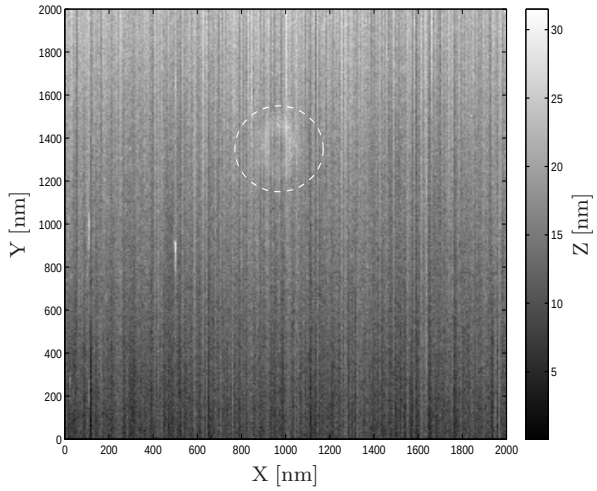

Figure 4.62: Donut–shaped structure (the circle is a guide to the eye) detected on a surface occupied with prokaryotic membrane proteins. The image is acquired using a high pixel–resolution.

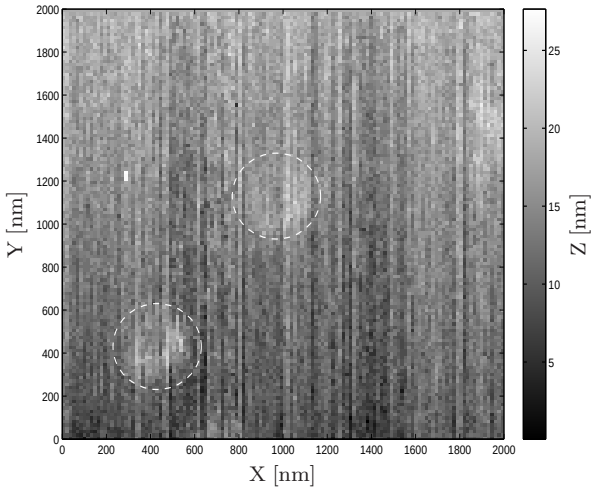

Figure 4.63: Donut–shaped structures (the circles are a guide to the eye) detected on a surface occupied with prokaryotic membrane proteins.

Nanocrystals on Biotinylated BSA

For further analysis of the resolution of the SICM, BSA/biotinylated BSA–coated LabTek surfaces are utilized for immobilization of Nanocrystals (QDot 655, Invitrogen, Germany). The Qdot 655 streptavidin conjugate features a red–fluorescent QDot nanocrystal core within a functional coating to which streptavidin has been covalently attached. The product is provided as a solution of 1 μM concentration. Nominal size of the nanocrystals as measured by fluorescence correlation spectroscopy (FCS) is reported to be 20 nm to 30 nm *[Doose et al., 2005; Larson et al., 2003; Yao et al., 2005]*.

Surface preparation is done like described above with a ratio of 1:1 between biotinylated BSA and BSA. The LabTek well is filled with about 0.75 ml of fresh PBS before 10 μl of a 10^{-9} M diluted solution of the Qdots 655 is added. After some minutes of incubation the chamber is rinsed gently with fresh PBS, while taking care of not letting the surface come in contact with air.

Scanning of a surface that is prepared in the described way gives a topographical image like presented in figure 4.64. Here, a scan of a $5 \times 5\ \mu\mathrm{m}^2$ of the surface is scanned with pixels of $50 \times 50\ \mathrm{nm}^2$ size. While the overall number of signals is only three, the average density of 0.12 $\mu\mathrm{m}^{-2}$ is at least comparable to the ones obtained by fluorescence microscopy, presented in section 4.2.5. The lateral dimension of the spots can be roughly estimated to be between 250 nm to 300 nm, which is much broader than

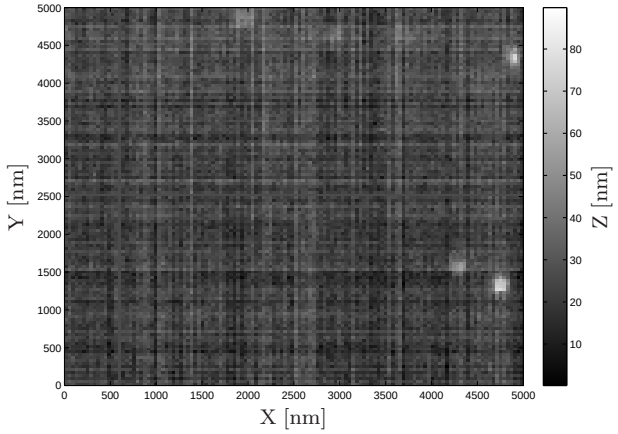

Figure 4.64: SICM scan of QDots655 immobilized on a biotinylatedBSA/BSA surface.

the (nominal) size of the NCs. A detailed SICM scan of the region surrounding a single NCs signal is shown in figure 4.65. Here, a probe of 50 MΩ resistance is oscillated at

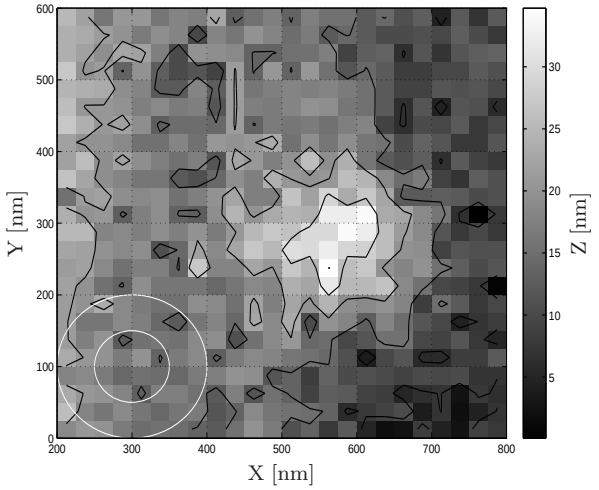

Figure 4.65: SICM signal of a single NC. The circles represent the estimated inner and outer diameter of the SICM probe.

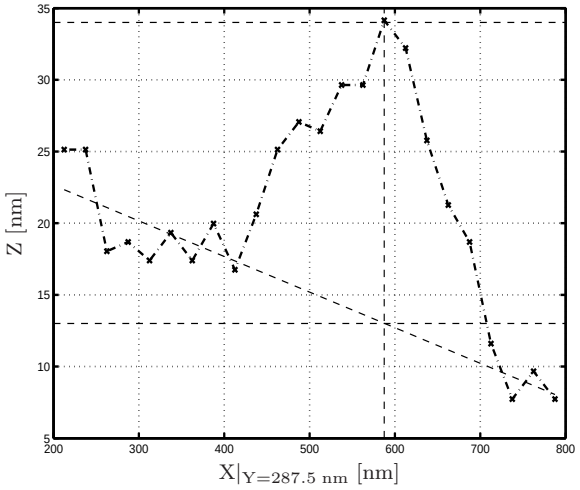

Figure 4.66: Cross section profile of a single NCs SICM signal. The dashed lines represent the linearly fitted surface–profile and points of intersection to guide the eyes in estimating the signals height.

1.2 kHz and 30 nm amplitude. An area of $0.8 \times 0.8\ \mu\text{m}^2$ is scanned with 32×32 pixels and out of this scan a part of 600×600 nm is presented. As a guide to the eye, contour lines are drawn every 7.5 nm. It shows that the NC signal is approximately circular–shaped. The two circles in the lower left corner of the plot indicate the outer and inner diameter of the probe used. As estimated from the resistance measured, these diameters are 200 nm and 100 nm, respectively. Further studies on the detailed signal are visualized in figure 4.66. Here a cross section profile is shown that elucidates the height of the signal, which can be given as 20 nm $\pm$ 5 nm. The overall width of the

signal is 200 nm to 250 nm.

Goat rhIGF-1 Antibodies

Monoclonal recombinant human antibodies IgG (goat anti rhIGF-1, R&D Systems, Inc., MN, USA) are studied to extend the presented analysis of the SICM resolution. The antibodies are large biomolecules with a mass of 52 kDa. Their size can be described by an ellipsoidal hull whose axes have a length of 14 nm, 6 nm and 3 nm *[Yu et al., 2005]*. Since the antibodies should bind to glass non–specifically but strong enough for reliable SICM scanning, HF–etched chamberslide surfaces are used as support surfaces. The scanning is done using a borosilicate nanopipette with a comparatively large resistance of 100 MΩ indicating a small tip aperture radius of significantly below 50 nm. Furthermore the reference value for the distance feedback is increased from commonly used values of 1 V up to 3 V, thus reducing the referenced tip–sample distance during scanning. The amplitude of the probe oscillation is lowered to 25 nm. Commonly used values for the probe oscillation amplitude are between 50 nm and 150 nm. All these adjustments should lead to an increase of the resolution of the SICM towards its intrinsic resolution limits. The surface is scanned at a high resolution of 128 × 128 pixel

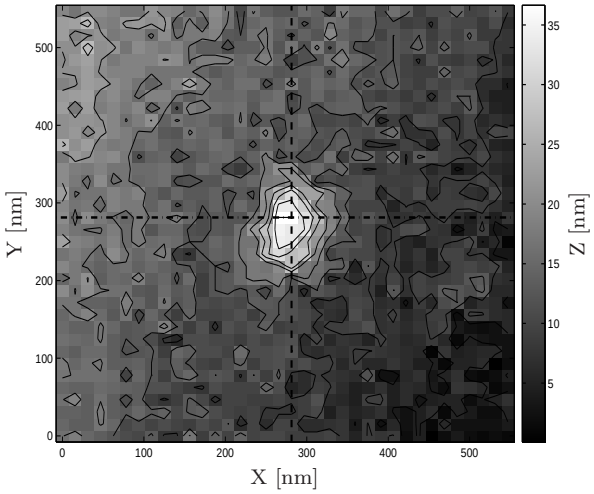

Figure 4.67: Single antibody (goat, anti rhIGF-1) on etched glass.

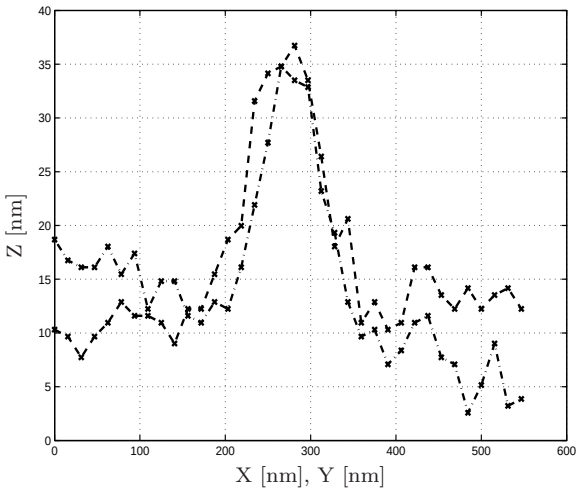

Figure 4.68: Cross section profiles of a single antibody on etched glass. Compare with the lines in figure 4.67.

on 2×2 μm^2. To have an overview over the homogeneity of the surface structure and the density of detected antibodies, several locations are scanned, each separated from another by some hundreds of micrometers. The surface is characterized by circular

shaped dots at a density of $\approx 0.1\ \mu\mathrm{m}^{-2}$. Figure 4.67 illustrates a representative spot. The dots can be identified due to the sharp discrimination from the surface, since they are featuring a height of $\Delta z = 20$ nm. Magnitude of the noise of the height information scanned on the etched glass plane is only 2 nm to 3 nm. Width of the dots is measured to be 100 nm to 120 nm.

Discussion

Cell Membrane Proteins

Studies on the surface prepared with bacterial membrane proteins yield results that give information about the resolution of the SICM. Since several equally sized spots are detected by the SICM after adding the proteins to the surface, it is assumed that the binding of the proteins to the surface did succeed. The strep–tag amino acid sequence immobilizes the glutamate transporter by specific binding to the streptavidin. Therefore, the successful detection of the proteins by SICM could be demonstrated.

The measured width of 300 nm is about 30–fold the real size of the protein. This difference can be explained by the fact that for samples that are smaller than the probe, the resulting signals lateral size minimum is limited by the dimension of the probe. This can be understood by thinking of scanning a rectangular step of fixed height h and infinite width. Keeping the scan direction of the SICM probe perpendicular to the step, the resulting height information would be a monotonic increase of the control function (and therefore a monotonic decrease of the stage height) from $\Delta z = 0$ to $\Delta z = h$. This increase is spread over a distance of Δs in scan direction that is at least equal to the width of the SICM probes outer tip diameter. Therefore, as a rough estimate, samples of dimensions smaller than the scanning probe are imaged to the size (and geometry) of the probe itself. So the probe diameter represents a minimum boundary for the SICM's resolution, which is also the case for all other types of SPMs.

The aspects discussed above are concerning the lateral resolution of the microscope only. Concentration on the analysis of the vertical or axial resolution, height information gathered from the protein's signals must be compared with their real height. In lack of detailed information, the shape of the proteins is assumed to be globular with a diameter of 10 nm. In any case, the biomolecule for sure is significantly smaller than the outer diameter of the scanning probe. Their height determined by the microscope varies between 5 nm and 20 nm. This means, that a difference of 5 nm to 10 nm between

the measured and nominal height occurs. Determination of the standard deviation of the SICM height signal generated on this surface yields a value of 8.2 nm.

Indicated by the donut–shaped structures shown in figures 4.62 and 4.63 is that an interesting process can take place when samples much smaller than the probe are scanned. It is presumed, that the ring–structure occurs due to the effect of imaging the probes cross section. While the immobilized protein is rastered by the microscope, the LIA response increases only while the sample is located directly beneath the glass wall of the probe. While it is located under the tip opening, the current modulation amplitude detected by the LIA is smaller. This suggestion is supported by the geometry of the rings. Their outer and inner diameter are reproducibly scanned to 250 ± 10 nm and 120 ± 10 nm, respectively. These values match those above, estimated to be the outer and inner diameters of the pipette. Because of the small diameter of the proteins scanned, the signal height is only about 5 nm and so hardly above the detection limit of the microscope. The circumstances responsible for the difference in the height of the signals between the scans of figures 4.60 and 4.62 / 4.63 are not understood. The only mutually alteration between the scans is a significant increase of the pixel–resolution.

Nanocrystals on Biotinylated BSA

Similar to the results for scanning of membrane proteins, the signals obtained from nanocrystals immobilized on biotinylated BSA are much broader than the NCs cross-section. Again, this can be explained by the fact that for samples that are much smaller than the probe, the resulting signals lateral size minimum is limited by the dimension of the probe. In this experiment a borosilicate pipette with a tip–resistance of 60 MΩ is used, corresponding to a tip–radius of approximately 50 nm to 70 nm. Assuming a ratio between the inner and the outer radius of the pipette that is constant (and equal to 0.58:1) throughout its whole length, the outer diameter of the tip should be between $2 \cdot 50/0.58$ nm ≈ 170 nm and $2 \cdot 70/0.58$ nm ≈ 240 nm, which is, as is indicated by the representative circles shown in the plot, in the range of the detected signals diameters.

Hints on the axial resolution limit is given by the fact of being able to detect single spherical objects with a diameter of 20 nm to 30 nm (NCs). The measured height of the NCs is 20 ± 5 nm, which is a reasonable result. The standard deviation of the height distribution plotted in figure 4.64 is 5.3 nm. Together, this again suggests a vertical resolution limit of 5 nm.

Goat rhIGF-1 Antibodies

Using the SICM under specialized conditions did successfully result in a measurable increase of the SICM resolution. By simultaneously using a pipette–tip with reduced diameter, increasing the control loops reference value, and decreasing the oscillation amplitude, the signals produced by immobilized antibodies have a diameter of only 100 nm to 120 nm. The smaller pipette tip leads not only to an increase of the tip–resistance to 100 MΩ, but also to a stronger confinement of the electric field that locally interacts with the surface to yield the modulation of the current. Two further factors that increase the resolution are the reduced oscillation amplitude and reduced mean tip–sample separation. Contrary to the assumption, a smaller amplitude would lead to less sensitive distance detection, in combination with the smaller tip–sample separation, the opposite is the case.

In summary, all three samples studied by the SICM consistently confirm that its lateral resolution is limited by the cross section diameter of the probe. Further improvements of the resolution can be made by adjustments of the mean tip–sample separation as well as the amplitude of its oscillation. So a lateral resolution down to 100 nm is realized. The vertical resolution is demonstrated by successfully imaging objects of 10 nm to 20 nm size. The analysis of the height distribution of different scans yields standard deviations of 5.3 nm and 8.2 nm. These findings demonstrate that the maximum vertical resolution of the SICM is approximately 5 nm.

4.2.7 Surface Chemical Mapping

The interaction of the current flowing through the nanopipettes aperture with the surface is the basis of the scanning ion–conductance microscope. In SPM, the reliable topographical imaging as far as it is understood as the reproduction of the physical surface is only possible, if the probe–surface interaction used as the control function is independent from the lateral position. In SICM, this is not commonly the case. In the present section, problems and chances are presented that arise from the dependence of the distance–control functions from other observables than the tip–sample separation.

Inconel/Glass Calibration Sample

One sample that is scanned to demonstrate the effects mentioned above is an AFM calibration grid consisting of lines of Inconel fixated on a glass substrate (Figure 4.69). Inconel is a metallic alloy consisting of nickel, chromium, iron, titanium, aluminium,

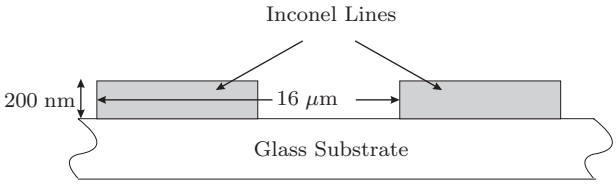

Figure 4.69: Cross section of the inconel/glass calibration samples nominal dimension.

and niobium. The grating period is 16 μm and the height of the inconel lines is 200 nm $\pm$ 10%. SICM analysis is made using a 85 MΩ borosilicate glass pipette. BIAS voltage is 180 mV with an oscillation amplitude of 80 nm at a frequency of 1.632 kHz. Figure 4.70 shows the information obtained from a 50×50 μm^2–scan with 256×256 pixel. The inconel lines are detected to be arranged perfectly parallel. The width of

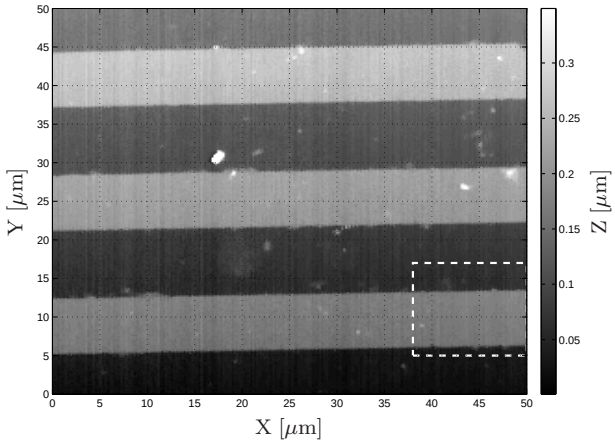

Figure 4.70: Intensity plot of the surface of the inconel/glass calibration sample. Three lines of inconel, each 7 micrometers wide (bright) are separated by grooves with a width of 8 micrometers. Unspecific contamination is detected.

the lines is measured to be 7 micrometers. The grooves separating the metallic lines are measured to be 8 micrometers wide. About 50 locally correlated signals with a size between 200 nm to 2.000 nm in diameter and a height of up to 250 nm are detected. A detailed scan of an area of 12×12 μm is shown in figures 4.71 and 4.72. In the 2D–intensity plot, contour lines are drawn every 20 nm. The inconel line width is detected in accordance to its nominal value of 7 μm. Again, some unspecific contaminations are scanned. Lateral variations (curves) off the nominal linear shape of the metal line sized by about 200 nm are detected reliably.

A cross section of the inconel line scan at X = 3.2 μm is shown in figure 4.74. Because the images exhibit a large aspect ratio of ΔY/ΔZ = 12 μm/0.2 μm = 60/1, dumping

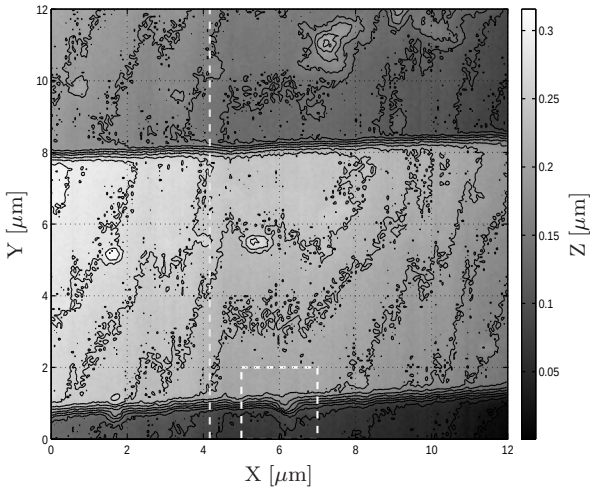

Figure 4.71: Detailed scan of an inconel line on glass substrate (square shown in figure 4.70). The contour lines represent a difference in height of 20 nm.

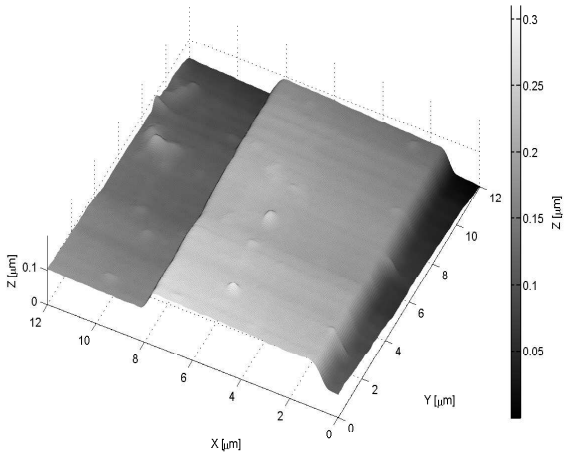

Figure 4.72: 3D–interpretation of the scan of a inconel line on glass.

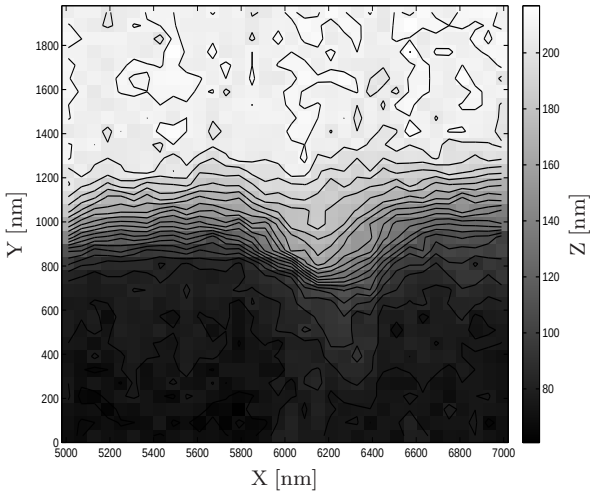

Figure 4.73: Detail (square in figure 4.71) of the inconel/glass AFM calibration sample.

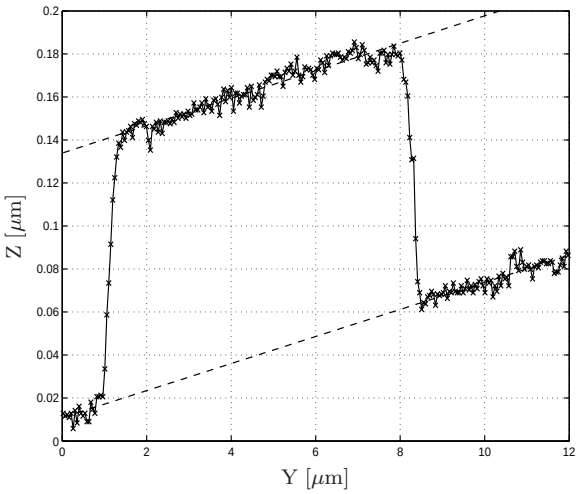

Figure 4.74: Cross section of an inconel line on glass. (line in figure 4.71) Nominal height is 200 nm $\pm$ 10%. Dashed lines represent linear fits to the upper and lower planes data.

of the sample plane with respect to the scanning stage movement is visually intensified. The data representing the top–plane of the inconel line is successfully fitted by a linear equation, $Z(Y) = 6.384 \cdot Y + 133.9$ [nm]. The same procedure yields for the lower (glass) plane $Z(Y) = 6.291 \cdot Y + 10.86$ [nm]. Hence, by analyzing the separation of the two virtual planes, the measured height of the metal lines is 123 nm.

Paramecium Bursaria Chlorella Viruses

The second sample is *paramecium bursaria* chlorella virus type 1 (PBCV-1), on which studies are executed for exploring the capabilities of the SICM towards imaging of large biological systems and surface consistency analysis. The PBCV is a virus infecting certain unicellular, eukaryotic, chlorella–like green algae and is common in freshwater bodies worldwide *[Etten, 2000]*. Confirmed by AFM and electron microscopy, the outer shape of PBCV-1 is icosahedral *[Kuznetsov et al., 2005]*. They have a lipid bilayered membrane located inside an outer glycoprotein capsid with a diameter of 190 nm *[Yan et al., 2000]*. Variations in the size of individual viruses were shown to be in the range of only some nanometers. The viruses are prepared for SICM scanning by diluting

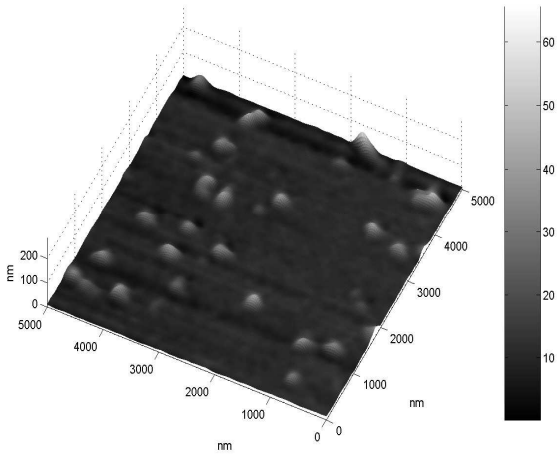

Figure 4.75: SICM study of PBCV-1 spread on a cleaned glass surface.

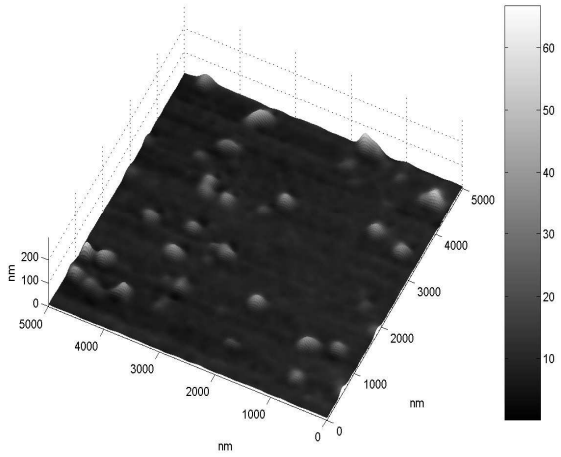

Figure 4.76: Scan of the same area as is presented in figure 4.75. Scanned 30 minutes later.

100 μl of the stock solution (containing 12 mg of virus mass per ml) in 1 ml of fresh PBS. A chamberslide well is cleaned with 0.5% HF before 50 μl of the solution is added to 0.5 ml of PBS in the well resulting in a overall dilution of 1:100 and a virus mass of 0.06 mg inside the well. Because it is assumed that the viruses unspecifically bind to the glass surface, no additional functionalization of the surface for immobilization is made. Again, scanning is executed using a borosilicate–glass nanopipette for probing the suface. This actual pipette has a resistance of only 5 MΩ, indicating a large pippette opening radius compared to the probes commonly used in this work, which have a resistance of about 50 MΩ and a known aperture radius of approximately 50 nm. The scan area is $5 \times 5\ \mu\text{m}^2$ divided into 100 $\times$ 100 pixels. (figure 4.77). Results of two scans of this area scanned with a temporal separation of 30 minutes are visualized in

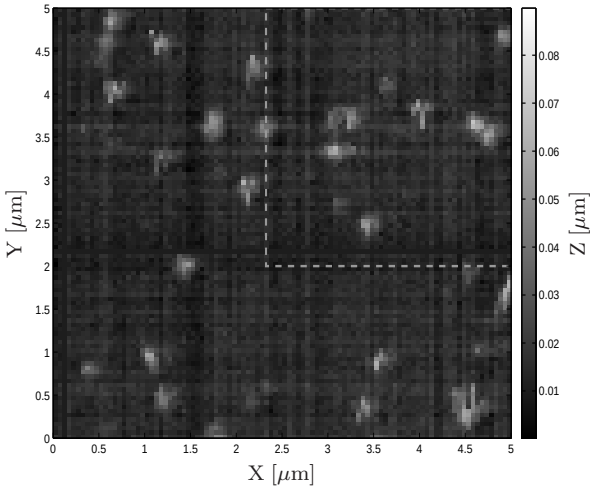

Figure 4.77: Scan of PBCV-1 on glass. The dashed square indicates the scan region of figure 4.78. Characteristic striped patterns can be seen for some viruses that is not arising from the correction of the image.

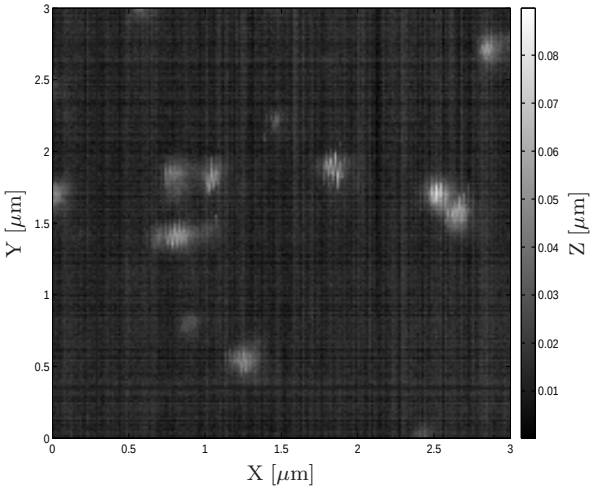

Figure 4.78: High–resolution (15×15 nm^2/pixel) scan of PBCV on glass. Striped patterns are formed by some of the samples. Strength of 'striping' corresponds to that of the signals in figure 4.77.

3D shaded surface plots in figures 4.75 and 4.76. Both images show about 30 signals with heights between 30 nm to 50 nm and 200 nm to 250 nm width. Significant similarity of the scan results can be observed concerning the position and dimensions of each individual signal. The 2D intensity matrix of the scans presented shows further details of the scan. While about one half of the spots has a circular shape, the rest has a characteristically striped pattern. The vertical height measured by the SICM in this work is only 40 ± 10 nm.

Discussion

Inconel/Glass Calibration Sample

The results are elucidating several detailed aspects of the scanning process. First, regarding the noise limitations the gradients determined for both planes are measured to be equal, which is in accordance with the nominal squared geometry of the sample (see figure 4.69). The gradients indicate a tilting angle of the sample surface of 0.36° with respect to the scanning stage. On the other hand, the vertical separation of the two fitted surfaces yields a value for the height of the inconel line of only 123 nm, which is 57 nm less than the lowest nominal tolerance of 180 nm. This significant difference is confirmed by other SICM measurements on this calibration sample. A possible expla-

nation can be found in the chemical heterogeneity of the sample. The metallic surface of the inconel line can be expected to form a strong chemical contrast to the silanoles of the glass–surface. If the surface influences the ionic current through the tip aperture via electrostatic interaction, the transfer function (the dependency of the conductivity on the tip–sample separation) will depend on the chemical characteristics of the sample surface. While keeping the reference value for the distance control unchanged, this will lead to an alternation of the working distance (mean tip–sample separation) because the surfaces chemical properties.

Paramecium Bursaria Chlorella Viruses

PBCV viruses scanned by AFM in solution show a deformation from the original icosahedrical shape with a diameter of 190 nm *[Kuznetsov et al., 2005]*. Using AFM, the particles have a height of 175 nm and a width of 200 nm which corresponds to a compression of about 8%. Presented SICM results give a height of only 40 ± 10 nm. This is an error of 70% to 80%. But as is depicted by the similarity of the figures 4.77 and 4.78, this difference is no statistical error. Like for the inconel/glass calibration grid, its origin might be the heterogneity of the chemical properties of the surface introducing an alteration in the transfer function, which is the dependency of the LIA response from the tip–sample separation.

The correlated striped pattern formation on individual viruses can be explained by differences in the binding strength of the sample to the glass. Since a two–way scan is performed like it is presented in figure 4.2, the scanning direction is alternating from row to row (from column to column in the figure). The intensity of the striped signals is shifted into the scanning direction, giving an alternating intensity pattern. Interestingly, the characteristic shape of each spot shows up to be reproducible, which is shown by the high–resolution scan shown in figure 4.78. This all indicates that the samples producing a striped signal pattern are eluding from the pipette during scanning, suggesting different mobilities and a tip–surface interaction of the scanned viruses.

In summary, an influence of the chemical properties / the charge of the surface must be taken into account when doing SICM measurements. The distance dependency seems to be significantly altered by temporal or local alterations in surface chemistry. This is the fundamental effect utilized in scanning electrochemical microscopy (SECM) *[Bard and Kwak, 1988; Bard et al., 1990; Lee et al., 1990; Bard et al., 1991; Wipf and*

Bard, 1992]. Here, the influence of the surface chemistry is used to perform 'chemistry mapping' of a surface. Therefore, the interaction of the chemistry with the tip–sample distance dependency is not necessarily harmful. However, if the chemical interactions with the ion current flow are understood they can be used advantageously as additional parameter to retrieve important information about the surfaces properties.

5 Conclusion and Outlook

This thesis reports about the development, characterization and demonstration of a scanning ion–conductance microscope (SICM). SICM is a scanning probe microscopical technique useful especially for the study of soft surfaces like cell–membranes. Adapted to SICM setup is a fluorescence microscope that is capable of gathering optical information from the probe that is scanned by the SICM. Fluorescence information can be collected simultaneously without any significant interaction between the SICM scanning process and the fluorescence detection. The combination of individual advances of both microscopical techniques makes the developed system very suitable for any application dealing with structural and/or functional analysis of macromolecules in complex biological environment. The following section will summarize the central results and point out possible next steps for further investigation and application. Some suggestions regarding the improvement of the SICM by equipping it with useful additional features and the latest technological developments are mentioned as well.

Results presented in this work point out that all components of the developed microscope operate as intended. Due to sophisticated isolation against electromagnetic noise pickup and thermal fluctuations as well as improved mechanical damping, nearly all intrinsic SICM functions work at their theoretical limits. Detection of the ionic current through the SICM probe tip is performed at a noise level of approximately 2 pA. This is in the region of the theoretical limit that can be achieved using the microelectrode amplifier used for SICM. Measuring the amplitude of current modulation by means of phase–sensitive detection has been demonstrated to work reliably and robust. A vertical oscillation of the SICM probe at frequencies of up to 2.5 kHz and amplitudes between 20 nm and 150 nm was shown. Regarding the resonance frequency of the piezo–stack of 50 kHz and the low mass of the probe holder, frequencies of about 20 kHz should be practicable. However, since other hardware limits the SICM scan speed and a high

oscillation frequency could introduce additional noise, currently 2 kHz is a reasonable upper limit. The distance feedback algorithm operates reliably at a frequency of up to 10 kHz. Studies on the dynamics of its parameters during scanning showed the correct adjustment of the feedback gains. No overshoot and no tendency to get into oscillation in the control's response to large input steps are visible, while the speed of the distance control is faster than that of other hardware components involved in the scanning process. Namely, the slower hardware is the scanning piezo stage. A custom function inside the function was implemented to make the scan process wait for the stage until it has fully executed the control signal. Any effort to further increase the SICM scan velocity should start at this point.

Reliable surface analysis has been demonstrated to be possible within the range of the piezo scanner of $100 \times 100 \times 20\ \mu m^3$. Statistical evaluation of scan data from smooth oil/water interfaces revealed an intrinsic noise level that forms a theoretical bottom line of 2 nm for the vertical SICM resolution. However, height data shows a practical axial resolution of 5 nm. This limit is due to pickup of noise components faster than approximately 10 ms. Signals that are that fast cannot be compensated by the distance control, since the scanning stage responds within about 5 ms to 10 ms. Further improvements in the axial sensitivity were achieved by lowering the oscillation amplitude and increasing the reference point of the feedback control. The lateral resolution is limited by the outer diameter of the scanning probe. For the borosilicate pipettes used, this diameter is about 200 nm. Correspondingly, the SICM's lateral resolution was determined to be between 150 nm and 250 nm. It was demonstrated that utilizing probes with a smaller tip diameter can result in an enhancement of the lateral resolution down to 100 nm. An additional error component in the axial SICM control with aperiodic temporal structure is detected with an amplitude of some tens of nanometers. It is a fluctuation changing the control signal on a timescale between ten seconds and one minute. Its origin is thought to be either remaining temperature fluctuations inside the positioning system or time–depended electromagnetical pickup of the reference oscillation from the bias electrodes, radiated by the piezo–stack housing. Since this error is slow enough to be compensated, it inevitably leads to a distortion of the scan data and results in a wave–structure in the image.

Surface scanning using the SICM is a process characterized by high dynamics. For each image–pixel, the feedback loop corrects the tip–sample separation with subnanometer vertical steps at a frequency of up to to 10 kHz. From the software point of view, a pixel is evaluated to be successfully scanned if the control is stabilized, i.e. if the

distance error magnitude is below a certain minimum for a predefined time. Applying this method ensures fast and efficient scanning on smooth topography, but also for stability and robustness (at the cost of scanning time) on complex terrain. Because of this, the overall scan duration of a SICM scan is not determined. Empirically, mean scan velocities of 30 ms to 40 ms per pixel can be expected resulting in scan durations of 10 minutes for an image of 256×256 pixels.

SICM studies on support surfaces showed that etched LabTek glass surfaces form an appropriate basis for SICM sample preparation. Roughness of these support surfaces is significantly below 5 nm, thus cannot be resolved by the SICM in the configuration used. Functionalization of these surfaces for specific binding of molecular samples succeeded using a protein based anchoring technique. Even after functionalization with biotinylated BSA, the roughness of etched glass surfaces is below the axial resolution of the microscope. On glass surfaces functionalized with biotinylated BSA, specific immobilization of QDot 655 streptavidin conjugate nanocrystals and streptavidin–labeled polystyrene microspheres has been demonstrated. Fluorescence detection revaled that the binding of the nanocrystals is not stable for longer than about 10 minutes. Contrary, binding of the polystyrene microspheres to the surface proved to be stable throughout many hours. Surface studies in parallel to fluorescence detection on the surfaces yields information about the density of NCs or microspheres attached to it. The SICM system successfully detected the nanocrystals as well as the microspheres at a density corresponding to that measured optically. The measured height corresponds to the one expected from nominal values. However, direct identification of individual NCs or beads was yet not possible due to problems in defining the lateral position of the SICM probe in fluorescence microscopy.

Influence of the surface's chemistry on the scanning results are shown by studying surfaces of strong chemically heterogeneity. Therefore scanning was performed on metal–lines with a nominal height of 200 nm $\pm$ 10% on a glass substrate. The height of these lines was measured by the SICM to be only 125 nm. The difference of 60 nm arises from a strong dependency of the SICM control signal from the surface chemical properties. This is confirmed by measurements of chlorella viruses. Their nominal height of 190 nm is measured by the SICM to be only 50 nm. This effect known as 'chemical mapping' is the basis of scanning electrochemical microscopy (SECM). If taken into account, chemical mapping can possibly serve as an additional channel of information in SICM.

From studies on the sample consisting of metal lines on glass not only information about the interaction between the surface chemistry and the SICM control signal can be revealed. Additionally, it is worth mentioning that the experiments show that the SICM probe is able to 'climb' a step of 200 nm nominal size. This result shows that there must be an anticipatory effect, allowing the probe to interact with surface components in the scan–direction. Since the probe's interaction with the scanned surface is based on the electric field at its tip, an anticipatory effect can occur due to the diverging character of the field's shape. The efficiency of this effect should depend on the pixel size and the amplitude of the probe oscillation. To a certain degree, this should allow even for the climbing of overhanging regions of topographies. However, this effect cannot substitute for a sophisticated method that makes scanning of overhangs and steep topographies possible in a robust and reliable manner. Efforts in applying the SICM on scanning of whole cells, that are adherent to glass substrates did not succeed. The cells chosen for these experiments have been insect cells (Sf9, Novagen, Germany), and *Escherichia coli* which show a semi–adherent character. Only a small part of the cell membrane is attached to the substrate, resulting in the formation of a large part of overhanging surface. It is assumed that due to this circumstance the SICM probe does not succeed in 'climbing' the cell wall when starting the scan from the glass substrate. Applying a backstep mode rejecting the surface by a predefined height before each single image pixel is scanned should circumvent this error.

With the SICM developed in this work, a tool is made available that offers many perspectives concerning applications in biology, chemistry, and physics. Localization of particles like individual biological macromolecules can be performed by the surface measurement potential of the microscope. Regarding the resolution demonstrated, even the in–vivo detection of such molecules should be possible reliably. However, the potential of the SICM is not only due to its capability of performing surface analysis. Combined with the powerful technique of fluorescence microscopy, an additional channel of information is available that can be used for analysis of single functional molecules. By using the hollow SICM probe and an appropriately shaped electrical field it is possible to deliver suitable dyes directly confined to the region of the fluorescence excitation focus. Temporal and spatial analysis of the fluorescent dye interacting with the scanned sample obtains information about the operation and conformation of single molecules. In addition, the SICM offers the ability of measuring local currents in the picoampere range, making direct observation of complex protein operation like that of ion–channels possible. Furthermore, contactless stimulation of functional areas of living biological

systems like cell membranes with simultaneous using the SICM potential mentioned above can yield much useful information for elucidating complex processes running inside a living cell.

Bibliography

Each reference is followed by numbers referring to the pages of citation.

E. Abbe. Beiträge zur Theorie des Mikroskops und der Mikroskopischen Wahrnehmung. *Arch. Mikrosk. Anat.*, 9:413–468, 1873. 1

A. J. Bard and J. Y. Kwak. Scanning Electrochemical Microscopy. *Abstracts of Papers of the American Chemical Society*, 196:18–Anyl, 1988. 118

Allen J. Bard, Guy Denuault, Chongmok Lee, Daniel Mandler, and David o. Wipf. Scanning Electrochemical Microscopy: A New Technique for the Characterization and Modification of Surfaces. *Acc. Chem. Res.*, 23:6, 1990. 6, 22, 118

A. J. Bard, G. Denuault, R. A. Friesner, B. C. Dornblaser, and L. S. Tuckerman. Scanning electrochemical microscopy: theory and application of the transient (chronoamperometric) SECM response. *Analytical Chemistry*, 63(13):1282–8, 1991. 118

R. M. Baum. Scanning Tunneling Microscope Achieves Atomic-Scale Resolution. *Chemical & Engineering News*, 64(16):22–25, 1986. 1

M. Bezanilla, S. Manne, D. E. Laney, Y. L. Lyubchenko, and H. G. Hansma. Adsorption of DNA to Mica, Silylated Mice, and Minerals - Characterization by Atomic-Force Microscopy. *Langmuir*, 11(2):655–659, 1995. 96

G. Binnig and H. Rohrer. Vacuum Tunnel Microscope. *Helvetica Physica Acta*, 55(2):128–128, 1982. 1

G. Binnig and H. Rohrer. Scanning Tunneling Microscopy, an Atomic Probe. *Scanning Electron Microscopy*, pages 1079–1082, 1983. 1

G. Binnig, H. Rohrer, C. Gerber, and E. Weibel. Surface Studies by Scanning Tunneling Microscopy. *Physical Review Letters*, 49(1):57–61, 1982. 1

G. Binnig, K. H. Frank, H. Fuchs, N. Garcia, B. Reihl, H. Rohrer, F. Salvan, and A. R.

Williams. Tunneling spectroscopy and inverse photoemission: Image and field states. *Physical Review Letters*, 55(9):991–994, 1985. 1

G. Binnig, C. F. Quate, and C. Gerber. Atomic force microscope. *Physical Review Letters*, 56(9):930–933, 1986. 3

G. Binnig, C. Gerber, E. Stoll, T. R. Albrecht, and C. F. Quate. Atomic Resolution with Atomic Force Microscope. *Surface Science*, 189:1–6, 1987. 3

F. Braet, C. Seynaeve, R. De Zanger, and E. Wisse. Imaging surface and submembranous structures with the atomic force microscope: a study on living cancer cells, fibroblasts and macrophages. *Journal of Microscopy-Oxford*, 190:328–338, 1998. 4

A. Bruckbauer, L. Ying, A. M. Rothery, Y. E. Korchev, and D. Klenerman. Characterization of a novel light source for simultaneous optical and scanning ion conductance microscopy. *Analytical Chemistry*, 74(11):2612–6, 2002. 7

A. Bruckbauer, D. Zhou, L. Ying, Y. E. Korchev, C. Abell, and D. Klenerman. Multicomponent submicron features of biomolecules created by voltage controlled deposition from a nanopipet. *Journal of the American Chemical Society*, 125(32):9834–9, 2003. 8

A. Bruckbauer, D. Zhou, D. J. Kang, Y. E. Korchev, C. Abell, and D. Klenerman. An addressable antibody nanoarray produced on a nanostructured surface. *Journal of the American Chemical Society*, 126(21):6508–9, 2004. 8

N. Crampton, W. A. Bonass, J. Kirkham, and N. H. Thomson. Formation of aminosilane-functionalized mica for atomic force microscopy imaging of DNA. *Langmuir*, 21(17):7884–91, 2005. 96

S. Doose, J. M. Tsay, F. Pinaud, and S. Weiss. Comparison of photophysical and colloidal properties of biocompatible semiconductor nanocrystals using fluorescence correlation spectroscopy. *Analytical Chemistry*, 77(7):2235–2242, 2005. 100, 108

R. J. Driscoll, M. G. Youngquist, and J. D. Baldeschwieler. Atomic-Scale Imaging of DNA Using Scanning Tunneling Microscopy. *Nature*, 346(6281):294–296, 1990. 4

Y. Ebenstein, T. Mokari, and U. Banin. Fluorescence quantum yield of CdSe/ZnS nanocrystals investigated by correlated atomic-force and single-particle fluorescence microscopy. *Applied Physics Letters*, 80(21):4033–4035, 2002. 100

J.L. Van Etten. *Phycodnaviridae Virus Taxonomy, Classification and Nomenclature of Viruses.* Academic Press, London, 2000. 116

G.F. Franklin, J. D. Powell, and A. Emami-Naeini. *Feedback Control of Dynamic Systems*. Addison-Wesley Publishing Company, Inc., 3 edition, 1994. 23

M. Fritz, M. Radmacher, and H. E. Gaub. Invitro Activation of Human Platelets Triggered and Probed by Atomic Force Microscopy. *Experimental Cell Research*, 205(1):187–190, 1993. 4

A. Ghazi, C. Berrier, B. Ajouz, and M. Besnard. Mechanosensitive ion channels and their mode of activation. *Biochimie*, 80(5-6):357–362, 1998. 6

J. Gorelik, A. Shevchuk, M. Ramalho, M. Elliott, C. Lei, C. F. Higgins, M. J. Lab, D. Klenerman, N. Krauzewicz, and Y. Korchev. Scanning surface confocal microscopy for simultaneous topographical and fluorescence imaging: application to single virus-like particle entry into a cell. *Proc Natl Acad Sci U S A*, 99(25):16018–23, 2002. 6

J. Gorelik, A. I. Shevchuk, G. I. Frolenkov, I. A. Diakonov, M. J. Lab, C. J. Kros, G. P. Richardson, I. Vodyanoy, C. R. Edwards, D. Klenerman, and Y. E. Korchev. Dynamic assembly of surface structures in living cells. *Proceedings of the National Academy of Sciences of the United States of America*, 100(10):5819–22, 2003. 6

J. Gorelik, Y. Zhang, A. I. Shevchuk, G. I. Frolenkov, D. Sanchez, M. J. Lab, I. Vodyanoy, C. R. Edwards, D. Klenerman, and Y. E. Korchev. The use of scanning ion conductance microscopy to image A6 cells. *Molecular & Cellular Endocrinology*, 217(1-2):101–8, 2004. 6

Y. Gu, J. Gorelik, H. A. Spohr, A. Shevchuk, M. J. Lab, S. E. Harding, I. Vodyanoy, D. Klenerman, and Y. E. Korchev. High-resolution scanning patch-clamp: new insights into cell function. *Faseb J*, 16(7):748–50, 2002. 5, 6

O. P. Hamill, A. Marty, E. Neher, B. Sakmann, and F. J. Sigworth. Improved Patch-Clamp Techniques for High-Resolution Current Recording from Cells and Cell-Free Membrane Patches. *Pflugers Archiv-European Journal of Physiology*, 391(2):85–100, 1981. 6

H. G. Hansma and J. H. Hoh. Biomolecular imaging with the atomic force microscope. *Annual Review of Biophysics & Biomolecular Structure*, 23:115–39, 1994. 4

P. K. Hansma, B. Drake, O. Marti, S. A. Gould, and C. B. Prater. The scanning ion-conductance microscope. *Science*, 243(4891):641–3, 1989. 4, 6, 11, 12

P. Happel, G. Hoffmann, S. A. Mann, and I. D. Dietzel. Monitoring cell movements and volume changes with pulse-mode scanning ion conductance microscopy. *Journal*

of Microscopy, 212(Pt 2):144–51, 2003. 5

E. Henderson, P. G. Haydon, and D. S. Sakaguchi. Actin Filament Dynamics in Living Glial-Cells Imaged by Atomic Force Microscopy. *Science*, 257(5078):1944–1946, 1992. 4

R. F. Heuff, J. L. Swift, and D. T. Cramb. Fluorescence correlation spectroscopy using quantum dots: advances, challenges and opportunities. *Physical Chemistry Chemical Physics*, 9(16):1870–1880, 2007. 105

P. Horowitz and W. Hill. *The Art of Electronics*. Cambridge University Press, Cambridge, 1988. 18

J. A. Howarter and J. P. Youngblood. Optimization of silica silanization by 3-aminopropyltriethoxysilane. *Langmuir*, 22(26):11142–11147, 2006. 100

D. H. Hu and H. P. Lu. Placing single-molecule T4 lysozyme enzymes on a bacterial cell surface: Toward probing single-molecule enzymatic reaction in living cells. *Biophysical Journal*, 87(1):656–661, 2004. 8

Y. E. Korchev, C. L. Bashford, M. Milovanovic, I. Vodyanoy, and M. J. Lab. Scanning ion conductance microscopy of living cells. *Biophysical Journal*, 73(2):653–8, 1997. 4, 6, 11, 12

Y. E. Korchev, M. Milovanovic, C. L. Bashford, D. C. Bennett, E. V. Sviderskaya, I. Vodyanoy, and M. J. Lab. Specialized scanning ion-conductance microscope for imaging of living cells. *Journal of Microscopy*, 188(Pt 1):17–23, 1997. 6

Y. E. Korchev, J. Gorelik, M. J. Lab, E. V. Sviderskaya, C. L. Johnston, C. R. Coombes, I. Vodyanoy, and C. R. Edwards. Cell volume measurement using scanning ion conductance microscopy. *Biophysical Journal*, 78(1):451–7, 2000. 7

Y. E. Korchev, Y. A. Negulyaev, C. R. Edwards, I. Vodyanoy, and M. J. Lab. Functional localization of single active ion channels on the surface of a living cell. *Nature Cell Biology*, 2(9):616–9, 2000. 6

Y. E. Korchev, M. Raval, M. J. Lab, J. Gorelik, C. R. Edwards, T. Rayment, and D. Klenerman. Hybrid scanning ion conductance and scanning near-field optical microscopy for the study of living cells. *Biophysical Journal*, 78(5):2675–9, 2000. 6, 7

C. Kung. A possible unifying principle for mechanosensation. *Nature*, 436(7051):647–654, 2005. 6

Y. G. Kuznetsov, J. R. Gurnon, J. L. Van Etten, and A. McPherson. Atomic force microscopy investigation of a chlorella virus, PBCV-1. *Journal of Structural Biology*, 149(3):256–63, 2005. 116, 118

J.R. Lakowicz. *Principles of Fluorescence Spectroscopy*. Kluwer Academic/Plenum, New York, USA, 2nd edition, 1999. 29

R. Lal and S. A. John. Biological applications of atomic force microscopy. *American Journal of Physiology*, 266(1 Pt 1):C1–21, 1994. 4

D. R. Larson, W. R. Zipfel, R. M. Williams, S. W. Clark, M. P. Bruchez, F. W. Wise, and W. W. Webb. Water-soluble quantum dots for multiphoton fluorescence imaging in vivo. *Science*, 300(5624):1434–6, 2003. 100, 108

C. Le Grimellec, E. Lesniewska, M. C. Giocondi, E. Finot, V. Vie, and J. P. Goudonnet. Imaging of the surface of living cells by low-force contact-mode atomic force microscopy. *Biophysical Journal*, 75(2):695–703, 1998. 4

C. Lee, J. Kwak, and A. J. Bard. Application of scanning electrochemical microscopy to biological samples. *Proceedings of the National Academy of Sciences of the United States of America*, 87(5):1740–3, 1990. 118

E. Lesniewska, M. C. Giocondi, V. Vie, E. Finot, J. P. Goudonnet, and C. Le Grimellec. Atomic force microscopy of renal cells: Limits and prospects. *Kidney International*, pages S42–S48, 1998. 4

A. Lewis and K. Lieberman. Near-Field Optical Imaging with a Non-Evanescently Excited High-Brightness Light-Source of Subwavelength Dimensions. *Nature*, 354(6350):214–216, 1991. 7

A. Lewis, M. Isaacson, A. Harootunian, and A. Muray. Development of a 500-a Spatial-Resolution Light-Microscope .1. Light Is Efficiently Transmitted through Gamma-16 Diameter Apertures. *Ultramicroscopy*, 13(3):227–231, 1984. 7

S. A. Mann, G. Hoffmann, A. Hengstenberg, W. Schuhmann, and I. D. Dietzel. Pulse-mode scanning ion conductance microscopy–a method to investigate cultured hippocampal cells. *Journal of Neuroscience Methods*, 116(2):113–7, 2002. 5

S. A. Mann, J. W. Meyer, and I. D. Dietzel. Integration of a scanning ion conductance microscope into phase contrast optics and its application to the quantification of morphological parameters of selected cells. *Journal of Microscopy*, 224(Pt 2):152–7, 2006. 5

Y. Martin and H. K. Wickramasinghe. Magnetic Imaging by Force Microscopy with

1000-a Resolution. *Applied Physics Letters*, 50(20):1455–1457, 1987. 4

Molecular Devices Corp.. *Manual of the Axopatch 200B Patch Clamp, Theory and Operation*. Molecular Devices Corporation, Union City, CA, USA, e edition, 1999. 30, 39, 40, 41, 73

National Instruments Corporation. *Manual of the BNC–2090 Rack Mount DAQ Accessory*. National Instruments Corporation, Austin, TX, USA, 1996. 46

Piezo System Jena GmbH. *Manual of the PA series stack type piezo actuators*. Piezosystem Jena, Jena, Germany, 2004. 37, 38, 78

Schott Rohrglas GmbH. *Schott Duran®: Physical and Chemical Properties Note*. Schott AG, Germany, 2007. 30

Stanford Research Systems Inc.. *Manual of the Model SR830 DSP Lock–In Amplifier*. SRS, Inc., Sunnyvale, California 94089, USA, 2002. 18

Sutter Instrument Company. *Operation Manual of the P-2000 Micropipette Puller*. Sutter Instrument Company, Novato, CA 94949, USA, 2.0/08110 edition, 1999. 31

Victrex plc. *VICTREX® PEEK™ Property Note*. Victrex plc, Lancashire, UK, 2007. 71

M. McElfresh, E. Baesu, R. Balhorn, J. Belak, M. J. Allen, and R. E. Rudd. Combining constitutive materials modeling with atomic force microscopy to understand the mechanical properties of living cells. *Proceedings of the National Academy of Sciences of the United States of America*, 99:6493–6497, 2002. 4

R. Morrison. *Grounding and Shielding Techniques in Instrumentation*. Wiley Interscience Publication, New York, second edition, 1977. 18

H. Nitz, J. Kamp, and H. Fuchs. A Combined Scanning Ion–Conductance and Shear–Force Microscope. *Probe Microscopy*, 1(2):14, 1998. 4, 6, 11

J.A. O'Keefe. Resolving power of visible light. *J. Opt. Soc. Am.*, 46:359, 1956. 1

D. Pastre, H. Iwamoto, J. Liu, G. Szabo, and Z. Shao. Characterization of AC mode scanning ion-conductance microscopy. *Ultramicroscopy*, 90(1):13–9, 2001. 5, 11, 21, 22

M. A. Poggi, E. D. Gadsby, L. A. Bottomley, W. P. King, E. Oroudjev, and H. Hansma. Scanning probe microscopy. *Anal Chem*, 76(12):3429–43, 2004. 4

D. W. Pohl, W. Denk, and M. Lanz. Optical Stethoscopy - Image Recording with Resolution Lambda/20. *Applied Physics Letters*, 44(7):651–653, 1984. 7

C. B. Prater, P. K. Hansma, M. Tortonese, and C. F. Quate. Improved Scanning Ion-Conductance Microscope Using Microfabricated Probes. *Review of Scientific Instruments*, 62(11):2634–2638, 1991. 4

R. Proksch, R. Lal, P. K. Hansma, D. Morse, and G. Stucky. Imaging the internal and external pore structure of membranes in fluid: TappingMode scanning ion conductance microscopy. *Biophys J*, 71(4):2155–7, 1996. 5

C. A. J. Putman, K. O. Vanderwerf, B. G. Degrooth, N. F. Vanhulst, and J. Greve. Viscoelasticity of Living Cells Allows High-Resolution Imaging by Tapping Mode Atomic-Force Microscopy. *Biophysical Journal*, 67(4):1749–1753, 1994. 4

M. Radmacher, R. W. Tillamnn, M. Fritz, and H. E. Gaub. From molecules to cells: imaging soft samples with the atomic force microscope. *Science*, 257(5078):1900–5, 1992. 4

K. T. Rodolfa, A. Bruckbauer, D. Zhou, Y. E. Korchev, and D. Klenerman. Two-component graded deposition of biomolecules with a double-barreled nanopipette. *Angewandte Chemie-International Edition*, 44(42):6854–9, 2005. 8

A. M. Rothery, J. Gorelik, A. Bruckbauer, W. Yu, Y. E. Korchev, and D. Klenerman. A novel light source for SICM-SNOM of living cells. *Journal of Microscopy*, 209(Pt 2):94–101, 2003. 7

D. Sanchez, U. Anand, J. Gorelik, C. D. Benham, C. Bountra, M. Lab, D. Klenerman, R. Birch, P. Anand, and Y. Korchev. Localized and non-contact mechanical stimulation of dorsal root ganglion sensory neurons using scanning ion conductance microscopy. *J Neurosci Methods*, 159(1):26–34, 2007. 6, 7

C. A. Schoenenberger and J. H. Hoh. Slow Cellular-Dynamics in Mdck and R5 Cells Monitored by Time-Lapse Atomic-Force Microscopy. *Biophysical Journal*, 67(2):929–936, 1994. 4

A. Sharma, K. I. Anderson, and D. J. Muller. Actin microridges characterized by laser scanning confocal and atomic force microscopy. *Febs Letters*, 579(9):2001–2008, 2005. 4

A. I. Shevchuk, J. Gorelik, S. E. Harding, M. J. Lab, D. Klenerman, and Y. E. Korchev. Simultaneous measurement of Ca2+ and cellular dynamics: combined scanning ion conductance and optical microscopy to study contracting cardiac myocytes. *Biophys J*, 81(3):1759–64, 2001. 5

A. I. Shevchuk, G. I. Frolenkov, D. Sanchez, P. S. James, N. Freedman, M. J. Lab,

R. Jones, D. Klenerman, and Y. E. Korchev. Imaging proteins in membranes of living cells by high-resolution scanning ion conductance microscopy. *Angew Chem Int Ed Engl*, 45(14):2212–6, 2006. 6, 11, 31

S. G. Shroff, D. R. Saner, and R. Lal. Dynamic Micromechanical Properties of Cultured Rat Atrial Myocytes Measured by Atomic-Force Microscopy. *American Journal of Physiology-Cell Physiology*, 38(1):C286–C292, 1995. 4

N. B. Standen, P. T. A. Gray, and M. J. Whitaker, editors. *Microelectrode Techniques: The Plymouth Workshop Handbook*. The Company of Biologists Limited, Cambridge, England, 1987. 17

E. H. Synge. A suggested method for extending microscopic resolution into the ultra–microscopic region. *Phil. Mag.*, 6:356–362, 1928. 1

M. K. Tsilimbaris, E. Lesniewska, S. Lydataki, C. Le Grimellec, J. P. Goudonnet, and I. G. Pallikaris. The use of atomic force microscopy for the observation of corneal epithelium surface. *Investigative Ophthalmology & Visual Science*, 41(3):680–686, 2000. 4

K. Umemura, H. Arakawa, and A. Ikai. High-Resolution Images of Cell-Surface Using a Tapping-Mode Atomic-Force Microscope. *Japanese Journal of Applied Physics Part 2-Letters*, 32(11B):L1711–L1714, 1993. 4

D. O. Wipf and A. J. Bard. Scanning Electrochemical Microscopy .15. Improvements in Imaging Via Tip-Position Modulation and Lock-in Detection. *Analytical Chemistry*, 64(13):1362–1367, 1992. 118

X. Yan, N. H. Olson, J. L. Van Etten, M. Bergoin, M. G. Rossmann, and T. S. Baker. Structure and assembly of large lipid-containing dsDNA viruses. *Nature Structural Biology*, 7(2):101–3, 2000. 116

J. Yao, D. R. Larson, H. D. Vishwasrao, W. R. Zipfel, and W. W. Webb. Blinking and nonradiant dark fraction of water-soluble quantum dots in aqueous solution. *Proceedings of the National Academy of Sciences of the United States of America*, 102(40):14284–14289, 2005. 100, 108

L. Ying, S. S. White, A. Bruckbauer, L. Meadows, Y. E. Korchev, and D. Klenerman. Frequency and voltage dependence of the dielectrophoretic trapping of short lengths of DNA and dCTP in a nanopipette. *Biophysical Journal*, 86(2):1018–27, 2004. 8, 20, 21, 32

R. Young, J. Ward, and F. Scire. Topografiner - Instrument for Measuring Surface

Microtopography. *Review of Scientific Instruments*, 43(7):999–1011, 1972. 1

Y. G. Yu, R. X. Xu, X. D. Jiang, and Y. Q. Ke. The study of 3-dimensional structures of IgG with atomic force microscopy. *Chinese Journal of Traumatology*, 8(5):277–82, 2005. 110

List of Figures

Abbreviations

AFM	Atomic Force Microscopy
APD	Avalanche Photodiode
BSA	Bovine Serum Albumine
CCD	Charge–Coupled Device
CEL	Counter–Electrode
CLSM	Confocal–Laser–Scanning–Microscopy
CW	Continuous Wave Laser Emission
DAC	Analog–to–Digital Converter
DAQ	Data Acquisition
EMCCD	Electron–Multiplying Charge–Coupled Device
EOF	Electro–Osmotic Flow
EP	Excitation Profile
FCS	Feedback Control System
FRET	Fluorescence Resonance Energy Transfer
FWHM	Full Width at Half Maximum
HF	High Frequency
HPC	Host PC
LIA	Lock–In Amplifier
MEA	Micro Electrode Amplifier
MOD	Reference Modulation Signal
NA	Numerical Aperture
NC	Nanocrystal
NI	National Instruments
PBCV	*Paramecium Bursaria* Chlorella Virus
PBS	Phosphate Buffered Saline

PCTRL	Piezo Controller
PIP	Nanopipette
PRA	Headstage Preamplifier
PSA	Piezo Stack Actuator
PSD	Phase Sensitive Detection
PSF	Point Spread Function
RMS	Root Mean Square
RTC	Real Time Controller
SBR	Signal to Background Ratio
SEM	Scanning Electron Microscopy
SFM	Scanning Force Microscopy
SICM	Scanning Ion–Conductance Microscopy
SNOM	Scanning Near–Field Optical Microscopy
SNR	Signal to Noise Ratio
STD	Standard Deviation
STM	Scanning Tunneling Microscopy
TCP/IP	Transmission Control Protocol/Internet Protocol
TEM	Transmission Electron Microscopy
UHV	Ultra High Vacuum

Acknowledgements

I would like to express my gratitude to everyone who helped and supported me during the research which eventually lead to the present thesis.

First of all I want to thank Prof. Markus Sauer for entrusting the very attractive subject of this work to me and for giving me enduring support and confidence during the last three years.

Without the extensive collaboration and many many discussions with all members of the group 'Applied Laser Physics and Laser Spectroscopy' in Bielefeld, this work would not have been possible. Dr. Sören Doose spent an endless number of his hours, not only for experimental work on the development of the microscope but also in helping me keeping track of the work and for proofreading the manuscript of this thesis. Thank you very much. In addition I am very thankful to Dr. Gerd Wiebusch for all his technical help, to Stephan Wörmer for support in all problems concerning IT, and to Reinhild Pätzmann and Dr. Rudolf Böttner for many helpful advices. I thank Dr. Andreas Biebricher for his useful tips, hints and fruitful discussions. Furthmore I appreciate very much the help that I got from the competence of the people working in the shops at the faculty of physics. A lot of custom designed essential components working in the microscope have been manufactured there.

I want to thank Prof. Dr. G. Thiel from the Institute of Botany of the University of Darmstadt, who provided the chlorella viruses to us. Prof. Dr. J. Heberle and A. Zuber from the Biophysical Chemistry group helped us with material and a lot of support concerned with the glutamate transporting proteins. Thank you very much. I am also grateful to Prof. D. Klenerman from the Department of Chemistry, University of Cambridge.

This work has only been possible because I had access to excellent equipment, thanks to

financial support by the Deutsche Forschungsgemeinschaft / Sonderforschungsbereich 613.

Der größte Dank geht an meine Familie und an meine Eltern, die mich immer in jeder erdenklichen Weise unterstützt haben. Schließlich gilt mein ganz besonderer Dank Claudia Schülke für ihre Geduld, Unterstützung und Motivation.

Erklärung

Hiermit erkläre ich, dass ich die vorliegende Arbeit selbständig verfasst und dabei keine weiteren als die ausdrücklich bezeichneten Hilfsmittel verwendet habe.

Bielefeld, den 27. August 2007

Achim Donnermeyer